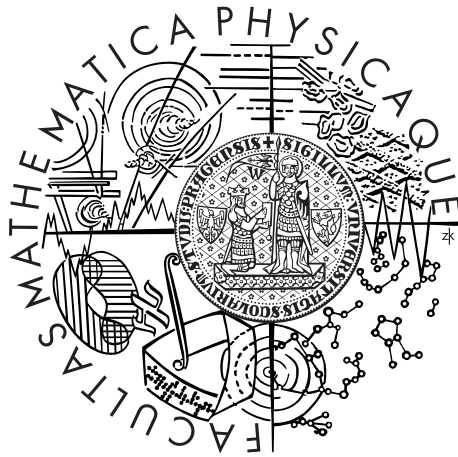


Charles University in Prague
Faculty of Mathematics and Physics

DOCTORAL THESIS



Kamil Daněk

Triple Gravitational Microlens

Institute of Theoretical Physics

Supervisor of the doctoral thesis: Mgr. David Heyrovský, PhD.

Study programme: Physics

Specialization: Theoretical Physics,
Astronomy and Astrophysics

Prague 2015

Acknowledgements

I would like to thank my supervisor Mgr. David Heyrovský, PhD. for organizing my otherwise disorganized thought processes and for guiding me through interesting topic that was definitely worth dedicating five years of work to.

To my wife

I declare that I carried out this doctoral thesis independently, and only with the cited sources, literature and other professional sources.

I understand that my work relates to the rights and obligations under the Act No. 121/2000 Coll., the Copyright Act, as amended, in particular the fact that the Charles University in Prague has the right to conclude a license agreement on the use of this work as a school work pursuant to Section 60 paragraph 1 of the Copyright Act.

In date

Kamil Daněk

Název práce: Trojitá gravitační mikročočka

Autor: Kamil Daněk

Katedra: Ústav teoretické fyziky

Vedoucí disertační práce: Mgr. David Heyrovský, Phd.

Abstrakt: Gravitační mikročočkou bývá objekt stelární nebo planetární hmotnosti, který způsobuje změnu zjasnění vzdálenějšího zdroje. V této práci zkoumáme mikročočky tvořené třemi hmotnými body, které mohou reprezentovat např. trojhvězdu, dvojhvězdu s planetou, hvězdu s dvěma planetami či systém hvězda + planeta + měsíc. Rozšiřujeme teorii trojitých čoček, abychom usnadnili interpretaci pozorování a umožnili správnou analýzu i ve složitějších případech. Soustředíme se hlavně na klasifikaci modelů trojčočky podle příslušných kaustik. Pro danou trajektorii zdroje určuje kaustika polohu píků na světelné křivce a proto je znalost kaustiky nutná pro správnou analýzu mikročočkování. Mapujeme závislost topologií kritické křivky (hlavních obrazů kaustiky) a počtu cuspů kaustiky v prostoru parametrů. Zavádíme nástroje této klasifikace pro obecnou n -bodovou mikročočku. Tyto modely pak demonstrujeme na čtyřech dvou-parametrických a třech tří-parametrických modelech gravitační mikročočky. Dále diskutujeme mapy zjasnění jak pro bodový tak pro nebodový zdroj s důrazem na chování objevující se u trojité čočky a obecné n -bodové čočky.

Klíčová slova: gravitační mikročočka, planetární systémy, kritické křivky a kaustiky

Title: Triple Gravitational Microlens

Author: Kamil Daněk

Department: Institute of Theoretical Physics

Supervisor: Mgr. David Heyrovský, Phd.

Abstract: Gravitational microlenses are stellar- or planetary-mass objects which cause a transient amplification when passing in the foreground of a distant source. We study microlenses that consist of three point masses. Such a model can represent a triple star, a binary star with a planet, a star with two planets, or a star + planet + moon system. Up to date, four planetary systems have been discovered in triple-lens microlensing events. We aim to expand the theory of triple lenses in order to simplify the interpretation of observed data and enable correct analysis in more complex cases. We focus mainly on the classification of triple-lens models with respect to their caustics. For a given source trajectory, the caustic determines prominent features on the light curve and thus its knowledge is essential for the analysis of microlensing events. We map the topology of the critical curve (the main caustic image) and the number of cusps of the caustic in the lens-model parameter space. We introduce methods for the classification of general n -point-mass microlenses. The methods are then demonstrated on four two-parameter and three three-parameter models. Furthermore, we study amplification maps for both point sources and extended sources, with an emphasis on new features appearing in triple and general n -point-mass microlenses.

Keywords: gravitational microlens, planetary systems, critical curves and caustics

Contents

1	Introduction	3
1.1	Historical context	3
1.2	Lens equation	4
1.3	Single-lens microlensing	5
1.4	Two-point-mass lens microlensing	6
1.5	Content overview	9
2	Analysis of n-point-mass Lens critical curves and caustics	10
2.1	Introduction	11
2.2	Lensing by an n -point-mass lens	12
2.3	The Jacobian and its properties	15
2.3.1	Definition and global character	15
2.3.2	Stationary points: maxima and saddles	15
2.3.3	Jacobian contours and critical curves	16
2.4	The n -point-mass lens critical curve	19
2.4.1	Critical-curve topology	19
2.4.2	Identifying topology changes in parameter space	20
2.5	The n -point-mass lens caustic	21
2.5.1	Caustic structure and cusp number	21
2.5.2	Cusp condition	22
2.5.3	The cusp curve and its properties	23
2.5.4	Caustic metamorphoses and the morph curve	25
2.5.5	Distinguishing butterflies from swallow tails	27
2.6	Lens analysis using cusp and morph curves	28
2.7	Summary	32
3	Critical curves and caustics of triple-lens models	34
3.1	Introduction	35
3.2	The n -point-mass lens and its Jacobian	37
3.3	Critical-curve topology regions in parameter space	38
3.3.1	Critical-curve topology and its changes	38
3.3.2	Analytical boundaries computed by resultant method	40
3.3.3	Numerical boundaries via first resultant	42
3.3.4	Numerical boundaries via Jacobian-contour correspondence	44
3.4	Mapping the number of cusps of the caustic in parameter space	44
3.5	Triple-lens models	46
3.5.1	General properties	46
3.5.2	LS Model: Linear Symmetric Configuration	48
3.5.3	LA Model: Linear Asymmetric Configuration	56
3.5.4	TE Model: Equilateral Triangle Configuration	60
3.5.5	TI Model: Isosceles Triangle Configuration	66
3.5.6	Overview of critical-curve topologies and caustic structures	72
3.6	Summary	77

4	Critical-curve topologies of triple lens with fixed fractional masses	79
4.1	Parameters-space visualization	79
4.2	Probability of topology occurrence	80
4.3	Equal-mass model	81
4.4	Planet-in-binary model	85
4.5	Hierarchical-mass model	89
5	Light curves and amplification maps	93
5.1	Summary of methods	94
5.2	Description of the code	95
5.3	Precision of the algorithm	97
5.4	Amplification maps	100
5.5	Sensitivity to an extended source	102
5.6	Amplification in vicinity of caustic metamorphoses	104
6	Conclusions	109
	Bibliography	111
A	Computing the resultant of two polynomials	117
B	Spurious results of the resultant method	119
C	Cusp and morph curve polynomials of the LS model	120

1. Introduction

During the gravitational lensing event, a light from a distant source is deflected by the influence of a closer object that acts as a gravitational lens. There are strong, weak and micro regimes of gravitational lensing differentiated both by measuring methods and typical scales of mass of the lens.

Strong lensing manifests several images of the source. Sources of strong lensing can be a quasar or a galaxy while the lens can be other galaxy or galaxy cluster. In the case of weak lensing, it is impossible to characterize the lens by its effect on a single source. Rather, a statistical method of evaluating small deformations of a large number of the source galaxies is employed to obtain mass distribution of the lens which is, mostly, a cluster of galaxies. In the microlensing regime, an object of stellar mass acts as a lens while the source is bright star or quasar. Although the multiple images produced in microlensing are too close to be resolved, the time dependence of source amplification can be recorded.

1.1 Historical context

Pioneering works of Refsdal on gravitational microlensing date back to sixties of last century, e.g. (68). In 1986, Paczyński proposed microlensing as a method of dark-matter detection in galactic halo by means of observing a large number of stars in Large Magellanic Cloud (55). This article motivated several surveys of which EROS (Expérience pour la Recherche d'Objets Sombres), MACHO (MAssive Compact Halo Object), OGLE (Optical Gravitational Lensing Experiment) and MOA (Microlensing Observation in Astrophysics) were the most prominent. While EROS and MACHO resulted in disfavoring galactic dark-matter model predominantly consisting of compact objects (2), OGLE and MOA became major microlensing surveys contributing to planetary detections.

Most of the microlensing events can be modeled by single point-mass lens which results into single symmetric peak in a light curve. Two-point-mass lens was analyzed for the first time in 1986 by Schneider and Weiß (71) who demonstrated utility of critical curve and caustic for the model. Applicability of the two-point-mass lens model was discussed by Mao and Paczynski (53). They estimated that approximately 10% of all microlensing events in the Galactic Bulge is due to lensing by a two-point-mass lens and demonstrated that even a star with a planet can act as a two-point-mass lens.

The articles expanding the work on two-point-mass systems took several directions. Witt and Peters (79) added shear to the two-point lens model. Gaudi, Naber and Sackett (27) investigated central caustics of multiple planet systems. Bozza published series of articles focused on perturbative analysis of caustic in multiple lens systems of too high or too small separations (12), (13), (14). More interest in triple lenses was brought about by the first triple lens event observed OGLE-2006-BLG-109 (28). The successful analysis of the first three-point mass systems inspired several articles involving studies of detectability of the third low-mass object in a stellar system, e.g., detectability of moons around an extra-solar planets (38) and (48) and detectability of planets in a binary star systems (47), (17) and (69). Up to date there were three other triple-lens events pub-

lished: star plus two planets system OGLE-2012-BLG-0026 (39) and two events including planet in binary lens system OGLE-2008-BLG-0092 (60), OGLE-2013-BLG-0341 (31). However, up to this point, gravitational microlensing by a triple lens has not yet been satisfactorily analyzed theoretically. The substantial part of this thesis deals with classification of triple-lens caustics, starting with critical curves in various parameter-space sections then building a method of caustic cusp counting on top of critical-curve topology analysis.

1.2 Lens equation

In the gravitational microlensing, the light geodesic is assumed to be a straight line except for the point of deflection where its direction is changed by deflection angle α . The lens is assumed to be thin, i.e., the deflection occurs on a single plane perpendicular to the line of sight. Furthermore, the deflection angles are assumed to be small so that trigonometric function are approximated by their expansions up to linear terms. The thin lens is then described by a surface density in the lens plane. In the case of n -point-mass lens, the surface density has the form of a weighted sum of Dirac delta-functions in lens-point positions. With the introduction of the Cartesian coordinates on the lens plane (r_I, r_{II}) we obtain deflection vector $\boldsymbol{\alpha} = (\alpha_I, \alpha_{II})$

$$\boldsymbol{\alpha} = \frac{4G}{c^2} \sum_{j=1}^n M_j \frac{\mathbf{r} - \mathbf{r}_j}{|\mathbf{r} - \mathbf{r}_j|^2}, \quad (1.1)$$

where $\mathbf{r} = (r_I, r_{II})$ is position vector, $\mathbf{r}_j = (r_{jI}, r_{jII})$ are lens positions, M_j are lens masses, G is the gravitational constant, c is the speed of light.

There are several paths along which light can reach the observer. Each path is registered by the observer as a different image of the source. Given observer-lens distance D_l , we have angular position of the image $\boldsymbol{\theta} = (r_I/D_l, r_{II}/D_l)$. Combining basic trigonometry with equation (1.1), we can then infer the source position $\boldsymbol{\beta} = (\beta_I, \beta_{II})$ that has, under assumption of small angles, the form

$$\boldsymbol{\beta} = \boldsymbol{\theta} - \frac{4GM_{tot}}{c^2} \frac{D_{ls}}{D_l D_s} \sum_{j=1}^n \mu_j \frac{\boldsymbol{\theta} - \boldsymbol{\theta}_j}{|\boldsymbol{\theta} - \boldsymbol{\theta}_j|^2}, \quad (1.2)$$

where $D_{ls} = D_s - D_l$ is a lens-source distance, $M_{tot} = \sum_{j=1}^n M_j$ is total mass, $\mu_j = M_j/M_{tot}$ are lens mass ratios and $\boldsymbol{\theta}_j$ are lens angular positions.

The factor preceding the summation in equation (1.2) is the square of characteristic lens scale called Einstein radius

$$\theta_E = \sqrt{\frac{4GM_{tot}}{c^2} \frac{D_{ls}}{D_l D_s}}. \quad (1.3)$$

As was shown by Witt (78), the lens equation (1.1) can be expressed in an elegant form using complex notation. Normalized by Einstein radius θ_E we have $\zeta \equiv (\beta_I + i\beta_{II})/\theta_E$ for source position, $z \equiv (\theta_I + i\theta_{II})$ for image positions, $z_j \equiv (\theta_{jI} + i\theta_{jII})$ for lens positions. In these coordinates the lens equation is dimensionless and without additional constants

$$\zeta = z - \sum_{j=1}^n \frac{\mu_j}{\bar{z} - \bar{z}_j}, \quad (1.4)$$

where bars stand for complex conjugates.

The amplification of an image of a uniform source is given by the ratio of image areas to the source area. For a point source, the amplification of an image is given by the reciprocal absolute value of the Jacobian determinant of $z \rightarrow \zeta$ mapping by equation (1.4) at the image position. Total amplification is then obtained by a summation of the amplification over all image positions.

In the case of a source with non-constant brightness profile $I(\zeta)$ the extended-source amplification $A_*(\zeta_c)$ can be expressed using point-source amplification via

$$A_*(\zeta_c) = \frac{\int_S A_0(\zeta_c + \zeta) I(\zeta) d^2\zeta}{\int_S I(\zeta) d^2\zeta}, \quad (1.5)$$

where the integration domain is source area S in the complex plane and ζ_c stands for the center of the source. For simplicity, we describe the brightness profile by radially symmetric by linear limb-darkening law

$$I(r) = I_0 \left[1 - v \left(1 - \sqrt{1 - r^2} \right) \right], \quad (1.6)$$

where $v \in (0.0, 1.0)$ is the limb-darkening parameter and $r \in (0.0, 1.0)$ is radial coordinate, i.e., $r = 0$ for source center, $r = 1$ for the limb.

1.3 Single-lens microlensing

For the case of a single lens the lens equation 1.4 is reduced to

$$\zeta = z - \frac{1}{\bar{z}}, \quad (1.7)$$

where the lens is in the origin of coordinate system. If we substitute image position in polar form $z = r e^{i\theta}$ into equation 1.7 we can obtain image positions in the form $z_{\pm} = \pm r_{\pm} \zeta / |\zeta|$ where $r_{\pm} = \pm |\zeta| / 2 + \sqrt{1 + |\zeta|^2 / 4}$. The determinant of Jacobian is given by $\det J(z) = 1 - 1/|z|^2$. The total point-source amplification of a single lens is then given by

$$A_0 = \frac{|\zeta|^2 + 2}{|\zeta| \sqrt{|\zeta|^2 + 2}}. \quad (1.8)$$

When the source, the single-point lens and the observer are aligned, an image forms a circle with radius of one Einstein radius. Such a scenario corresponds to the infinite point-source amplification. In a non-aligned configuration, the two solutions of the lens equation (1.7) correspond to two images, one inside and one outside Einstein ring. The one outside is always amplified, the one inside the ring can have amplification $A < 1$, the amplification of each images diverge in aligned source-lens configuration.

The light curve of single a lens event with the linear source trajectory, firstly described by Paczynski (55), is a symmetric curve that is smooth except for a point source passing through the lens position.

For an extended source, the amplification is also finite. For instance, a disc source of radius ρ and uniform brightness whose center is aligned with lens and observer, the images merge into annulus of width given by the difference between image-lens distances of the two images of a point on the limb of the source. For that reason, the amplification of the extended source of uniform brightness is capped by $A_0 = \sqrt{1 + 4/\rho^2}$.

1.4 Two-point-mass lens microlensing

The first theoretical study of a two-point-mass lens has been done by Schneider & Weiß (71). It was shown that a set of source positions with infinite point-source amplification is no longer one isolated point as in the case of a single lens but forms a closed curves called caustics. The corresponding set of infinitely amplified images forms a critical curve.

The Caustic is concave curve composed of folds and cusps. While folds are smooth parts of the caustic, cusps are points where tangent vector changes its direction by π . Critical curve has smooth tangential derivatives. Both critical curve and caustic of two-point-mass lens consist of one to three non-intersecting loops.

As the source enters the caustic, the amplification diverges when the point source lies exactly on the caustic. At that point, two degenerate infinitely amplified images appear on the critical curve. When inside the caustic, the pair of images becomes non-degenerate and finite in the amplification.

The extended-source amplification changes continuously both inside and outside the caustic but the point-source amplification has discontinuities while crossing the caustic. While the point source is entering caustic along cusp axis, the amplification diverges and then decreases both as $1/r$ with r being distance from caustic. A fold transit of a point-source causes a jump to an infinite amplification at first then $1/\sqrt{r}$ amplification decrease.

Again, the amplification is finite for the extended sources lying on caustic. But still, entering the caustic via fold causes discontinuities in the first derivative on the light curve. Usually, fold caustic crossing even for the big sources causes characteristic asymmetric peaks on the light curve.

In the Figure 1.1 we plotted light curve of sample two-point-mass lens with the sequence of images for different extended source positions. Parameters of the lens are $s = 1.0$, i.e. separation of the lens points, and $\mu = 0.1$, i.e. fractional mass of one lens point. For the first source position, there are three images of the source, one outside the critical curve and two inside. For the second source position, the source overlaps the caustic which have two additional images merged into one on the critical curve. In the last position the source is already inside the caustic, the additional images split and shrink causing decrease in total amplification. The light curve is again smooth while more peaks are present. Discontinuities in the first derivative of the light curve are clearly visible for positions where source enters and exits the caustic completely.

Schneider and Weiß (71) has shown that a two-point-mass lens with equal masses produces caustics and critical curves of three different topologies with two extra merging topologies at separations $d = 1/\sqrt{2}$ and $d = 2$.

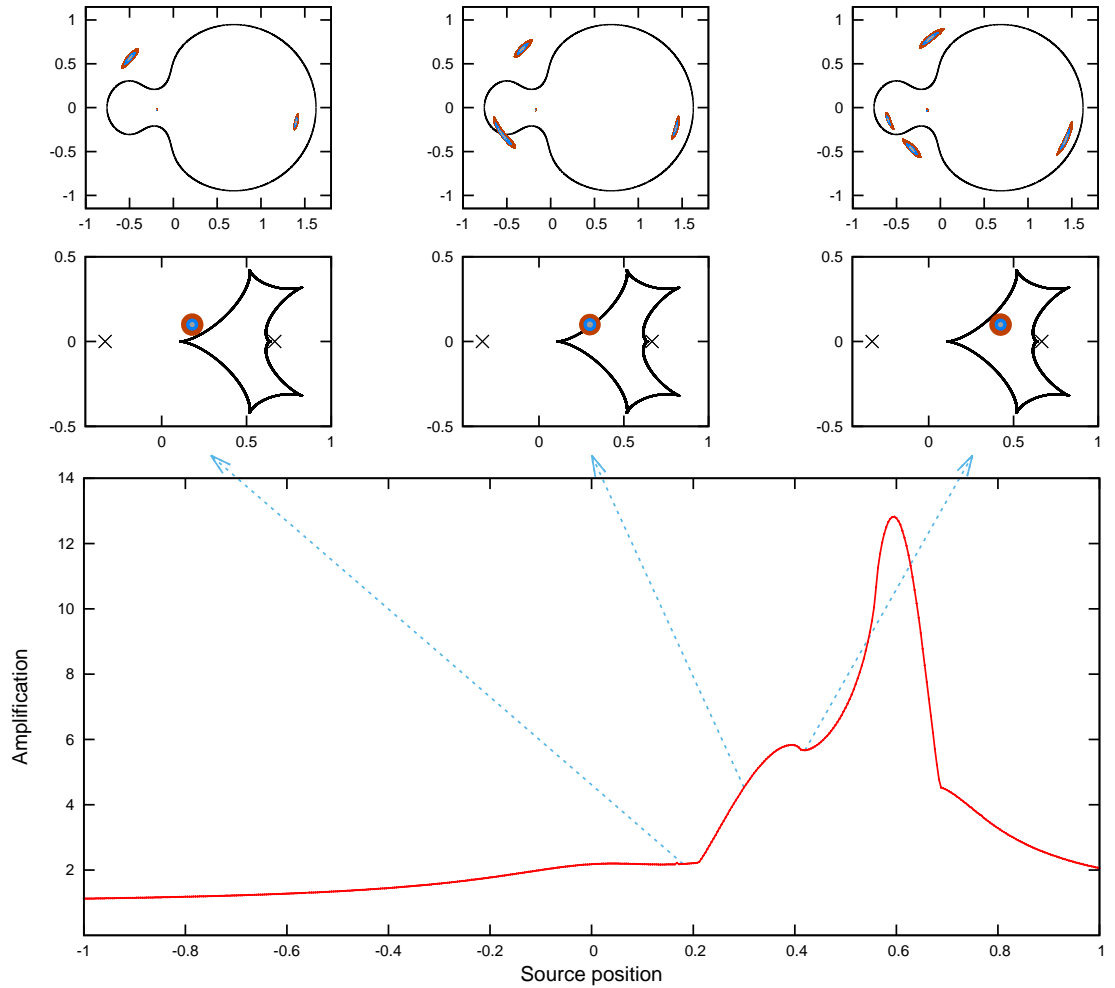


Figure 1.1 Two-point-mass lens: light curve and images. Bottom panel for light curve parametrized by x-position of the source. Source radius $\rho = 0.06$, impact parameter 0.1. Each separate column for different source position. Middle panels: colorful concentric rings for the source position; black curve for the caustic; black cross for the lens position. Top panels: black circle for critical curve, colored areas for images. Each image area correspond by color to a source ring.

More general results on the topological classification of caustics of a two-point-mass lens was obtained by Erdl & Schneider (25), using Sylvester matrix method described in the next chapter. It was shown that topologies found by (71) are the only topologies possible for a generic binary lens.

The condition for a topology of critical curve and caustic to change forms two curves in the two-dimensional parameter space $[\mu, d]$ which separates three regions with three different topologies of critical curve and caustic. These are usually labeled according to the separation d as “close” (critical curve formed by three loops), “intermediate” (one loop), and “wide” (two loops), with boundaries between the regimes depending on the binary fractional mass. In addition to those non-merging topologies, the two merging topologies are present on the borders between regions.

Parameter space of binary lens is shown in Figure 1.2 with the examples of critical curves and caustic with top panel for “wide”, panel in the middle for “intermediate”, and bottom panel for “close” topology.

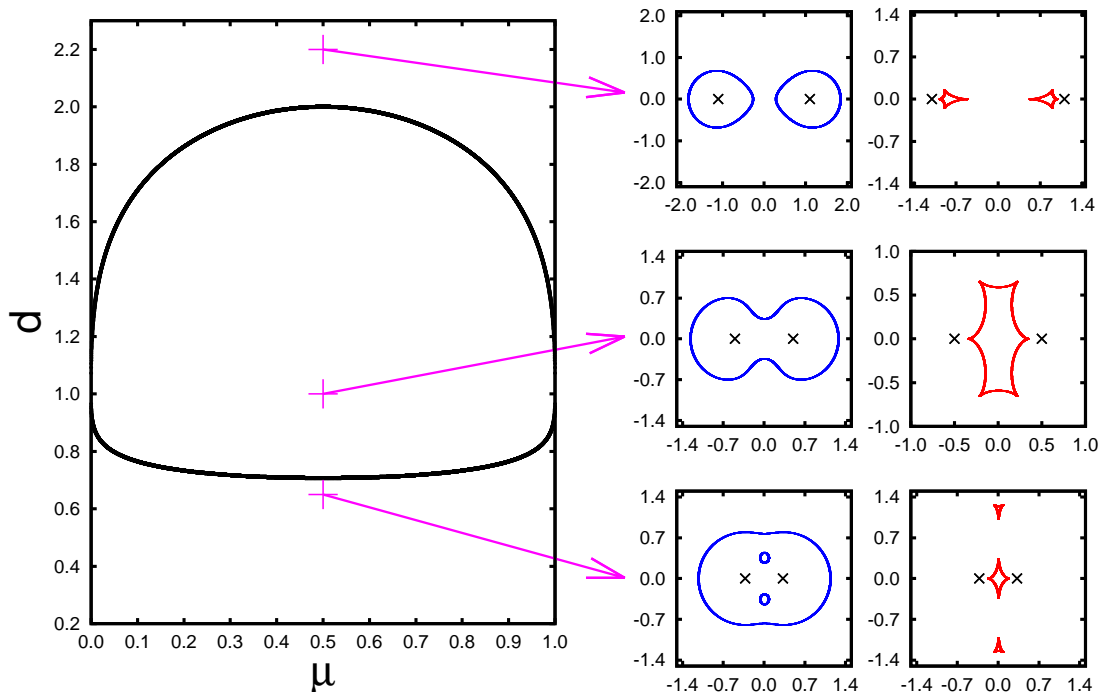


Figure 1.2 Topological division of parameter space of two-point-mass lens with examples of critical curves and caustics. Left panel: Parameter space with curves representing topology transitions of critical curves and caustics. Right panels: Examples of critical curves and caustics of different topology; red for critical curves, blue for caustics. Examples are of mass ratio $\mu = 0.5$ different topologies separations d : top for wide topology $d = 2$, middle for intermediate and $d = 1$, bottom for close topology $d = 0.65$.

This chapter shows connection between Figure 1.2 and Figure 1.1. The inverted lens equation (1.4) maps the source to its images. A caustic determines position of caustic-crossing features on a light curve given a source trajectory, a source size and a brightness profile, e.g., the light curve of Figure 1.1. Finally, a topology analysis like the one in Figure 1.2 maps the caustic topology in the

parameter space of the lens.

1.5 Content overview

The second chapter consists of the article “Image-plane Analysis of n-point-mass Lens Critical Curves and Caustics” accepted by The Astrophysical Journal. Its introduction serves here as a more profound discussion of microlensing theory that we aim to expand. In the chapter new methods of critical-curve topology analysis and caustic cusp counting are introduced along with Jacobian-contour correspondence, cusp curve and morph curve that are useful utilities even beyond the scope of our topology analysis.

In the third chapter the methods of image-plane analysis of critical curves and caustics are demonstrated on four two-parametric models of triple lens. The chapter is a modified preprint version of the article “Critical curves and Caustics of Triple-lens Models” also accepted by The Astrophysical Journal.

The fourth chapter uses the topology-analysis method for three three-parameter models of triple lens. The chosen models are triple lenses with fixed mass ratios and arbitrary positions, namely mass ratios representing equal-mass triple star, planet in binary system and star, planet and moon system. More degrees of freedom bring our model closer to the observed events but poses serious difficulty in both visualizing 3D parameter space and in handling the topology regions. We visualize the parameter space as a sequence of ternary plots. Also, portions of parameter space that each topology occupies are evaluated.

The fifth chapter discusses methods of source amplification calculation. Here we present our algorithm using effective inverse ray shooting method to compute light curves and amplification maps under extended-source effect. Also, amplification pattern in the vicinity of swallowtail catastrophe and butterfly catastrophe is looked into.

2. Image-plane analysis of n -point-mass lens critical curves and caustics¹

ABSTRACT

The interpretation of gravitational microlensing events caused by planetary systems or multiple stars is based on the n -point-mass lens model. The first planets detected by microlensing were well described by the two-point-mass model of a star with one planet. By the end of 2014, four events involving three-point-mass lenses had been announced. Two of the lenses were stars with two planetary companions each; two were binary stars with a planet orbiting one component. While the two-point-mass model is well understood, the same cannot be said for lenses with three or more components. Even the range of possible critical-curve topologies and caustic geometries of the three-point-mass lens remains unknown. In this paper we provide new tools for mapping the critical-curve topology and caustic cusp number in the parameter space of n -point-mass lenses. We perform our analysis in the image plane of the lens. We show that all contours of the Jacobian are critical curves of re-scaled versions of the lens configuration. Utilizing this property further, we introduce the cusp curve to identify cusp-image positions on all contours simultaneously. In order to track cusp-number changes in caustic metamorphoses, we define the morph curve, which pinpoints the positions of metamorphosis-point images along the cusp curve. We demonstrate the usage of both curves on simple two- and three-point-mass lens examples. For the three simplest caustic metamorphoses we illustrate the local structure of the image and source planes.

Key words: gravitational lensing: micro — planetary systems — methods: analytical

¹Accepted by The Astrophysical Journal (21).

2.1 Introduction

The effect of the gravitational field of an astrophysical object on the passage of light from a background source was first computed for a point-mass-like object (24; 49; 50), which provided the simplest model of a gravitational lens. The model can be used in some cases as a first approximation for describing the strong lensing of a quasar by a galaxy. Its main application, however, has been in Galactic gravitational microlensing, where it accurately describes the lensing of a background star by another star passing in the foreground (e.g., 56).

The more than ten thousand observed microlensing events include several hundred cases of lensing by binary stars (lists can be found in 1; 40; 41; 42; 43; 73). In addition, there are more than 30 cases of microlensing by a star with a planet (e.g., 11; 9). Planets are currently the primary goal of microlensing surveys, which are sensitive to Solar-system analogues including Earth-mass planets in AU-scale orbits. Binary stars and stars with a planet can be both described by two-point-mass microlensing, which has been well understood theoretically for the past twenty years.

(16) first described an extension of the single point-mass lens obtained by adding a constant external shear. Such a system has extended caustics with different geometries in the weak and strong shear regimes. (71) performed a detailed analysis of a two-point-mass lens with equal masses. They demonstrated there were three distinct regimes for the critical curve and caustic: close, intermediate, and wide (in order of increasing separation of binary components). Transitions between neighboring regimes involved beak-to-beak metamorphoses of the caustic. (25) studied the lensing by two independent objects generally in different lens planes. As a special case they included the analysis of the single-plane (thin) two-point-mass lens with arbitrary mass ratio, showing that the regimes and metamorphoses were the same as in the equal-mass case. This result was corroborated by (79). From the range of subsequent papers we mention here the analysis by (23) of special cases of the binary lens.

However, already at $n = 3$ observations overtook theory. Three-component lensing was detected first by (28), second by (39). Both cases involved microlensing by a star with two planets. Most recently, (31) and (60) documented two events with microlensing by a binary star with a planet orbiting one of the components. Despite these observational advances, we still have no general insight into the possible regimes, types of critical curves and caustics permitted by the three-point-mass lens model. Nevertheless, a number of theoretical papers have been published on different aspects of triple-lens microlensing.

The first step beyond two-point-mass lensing was taken by (32), who studied the effect of an additional constant shear and demonstrated the appearance of the swallow-tail and butterfly caustic metamorphoses. This particular model was studied later also by (79). The general triple-lens equation was discussed by (65). Other works concentrated on specific types of triple lenses. Most frequent among them are papers studying lensing by a star with two planets (e.g., 27; 33; 69; 74; 81). Several papers explored lensing by a binary star with a single planet (e.g., 47; 37). Finally, the possibility of detecting exo-moons in microlensing events involving a star with a planet with a moon was discussed by (34), (38), and (48).

Much of the literature on general n -point-mass lenses revolved around the

question of the maximum possible number of images generated by such a lens. Individual contributions include (63), (54), (64; 66), (45), (5), (51), and (72). Pivotal among these are (66), who conjectured the maximum number of images was $5(n - 1)$, and (45), who proved the conjecture.

Other papers used perturbative methods to study the n -point-mass lens formed by a star with $n - 1$ planets. (12) explored the caustics of such a system, and (4) presented perturbative solutions of the lens equation. Finally, for the general n -point-mass lens (13; 14) studied the geometry of caustics in the close and wide limits.

The initial goal of the research behind the present paper was to explore systematically the properties of three-point-mass lenses. Following the methods used by (25) and (79) for the general two-point-mass lens, we set out to map critical-curve topologies and caustic geometries in the parameter space of the three-point-mass lens. Some early results appeared in (18), (19), and (20). In the course of our work we devised an efficient method for tracking the changes in critical-curve topology and caustic cusp number in the image plane of an arbitrary n -point-mass lens. We present these results here, while their application to the analysis of simple three-point-mass lens models appears separately in a companion paper (22).

We start in § 2.2 by describing the studied lens model, a thin n -point-mass gravitational lens with no external shear and no convergence due to continuous matter. We transform the lens equation to complex formalism following (78), which translates the analysis of lens properties to the study of polynomials, curves, real and complex functions in the complex plane.

Our approach is based on investigating the properties of the Jacobian of the lens, viewed in § 2.3 as a surface (real function) over the complex image plane. The main new insight is the correspondence of Jacobian contours with critical curves of zoomed-in or zoomed-out lens configurations, as described in § 2.3.3. The nature of the critical curve, and the changes of its topology in the parameter space of the lens are discussed in § 2.4.

In the following § 3.4 we study the caustic of the lens, paying particular attention to the changes in cusp number during caustic metamorphoses. We introduce two further tools for finding important points along Jacobian contours in the image plane: the cusp curve in § 2.5.3 for tracking the positions of cusp images, and the morph curve in § 2.5.4 for pinpointing the images of caustic-metamorphosis points. In § 2.5.5 we give specific conditions for distinguishing butterfly and swallow-tail metamorphoses.

We demonstrate the introduced method in § 2.6 on the example of a binary lens, and two triple lenses with swallow-tail and butterfly metamorphoses, respectively. Finally, we illustrate the local structures in the image and source planes in the vicinity of the three simplest caustic metamorphoses of the n -point-mass lens. The main results are summarized in § 3.6.

2.2 Lensing by an n -point-mass lens

In this work we study a composite gravitational lens formed by an association of n objects, which we approximate by point masses with masses M_j , $j = 1 \dots n$. We retain the usual thin-lens approximation, in which variations in the line-of-sight

distance of individual objects from the observer are neglected. The entire lens is thus assumed to lie at a single distance D_l from the observer and D_{ls} from the background source, so that $D_s = D_l + D_{ls}$ is the distance from the observer to the source. The angular positions $\boldsymbol{\theta}_j$ of the individual objects (lens components) in the plane of the sky, the position $\boldsymbol{\theta}$ of an image formed by the lens, and the position $\boldsymbol{\beta}$ of the source are all defined relative to a specific point of the lens. The usual choices for this point are: the position of a lens component, the center of mass of the lens, or its geometric center. While the equations in this work are independent of the choice, in the presented examples we use the geometric center as the origin. All object positions must be distinct, $\boldsymbol{\theta}_j \neq \boldsymbol{\theta}_k$ for all $j \neq k$, in order to qualify as an n -point-mass lens. In the thin-lens approximation any pair of objects exactly aligned with the observer acts as a single object with the total mass of the pair, reducing the number of lens components by 1.

The lens defines a characteristic scale in the plane of the sky: the angular Einstein radius corresponding to the total mass of the lens. It is given by

$$\theta_E = \sqrt{\frac{4G M_{tot}}{c^2} \frac{D_{ls}}{D_l D_s}}, \quad (2.1)$$

where G is the gravitational constant, c is the speed of light, and $M_{tot} = \sum_{j=1}^n M_j$ the total mass of the lens. In the absence of external shear and convergence due to continuous matter, the relation between the source and image positions is expressed by the lens equation

$$\boldsymbol{\beta} = \boldsymbol{\theta} - \theta_E^2 \sum_{j=1}^n \mu_j \frac{\boldsymbol{\theta} - \boldsymbol{\theta}_j}{|\boldsymbol{\theta} - \boldsymbol{\theta}_j|^2}. \quad (2.2)$$

Here $\mu_j \equiv M_j/M_{tot}$ are the fractional masses in units of total mass (hence $\sum_{j=1}^n \mu_j = 1$).

In order to study the properties of the lens it is advantageous to switch from vectorial to complex notation (78), in which all angular positions in the plane of the sky are expressed in terms of complex variables. If we additionally measure all angular positions in units of θ_E , the positions of the individual objects are $z_j \equiv (\theta_{jI} + i\theta_{jII})/\theta_E$, the image position $z \equiv (\theta_I + i\theta_{II})/\theta_E$, and the source position $\zeta \equiv (\beta_I + i\beta_{II})/\theta_E$, where we used Roman indices to mark vector components, and i is the imaginary unit. The inverse transformation from complex to vectorial notation is obtained by combining a position with its complex conjugate. For example, the image position $\boldsymbol{\theta} = (z + \bar{z}, -iz + i\bar{z}) \theta_E/2$, where \bar{z} denotes the complex conjugate of z . In matrix notation the transformation $\boldsymbol{\theta} \rightarrow z$ can be described by $(z, \bar{z}) = C(\theta_I, \theta_{II})$ with

$$C = \frac{1}{\theta_E} \begin{pmatrix} 1 & i \\ 1 & -i \end{pmatrix}. \quad (2.3)$$

The same matrix transforms similarly $\boldsymbol{\theta}_j \rightarrow z_j$ and $\boldsymbol{\beta} \rightarrow \zeta$. The opposite transformation $z \rightarrow \boldsymbol{\theta}$ can be described using the inverse matrix $(\theta_I, \theta_{II}) = C^{-1}(z, \bar{z})$, given explicitly by

$$C^{-1} = \frac{\theta_E}{2} \begin{pmatrix} 1 & 1 \\ -i & i \end{pmatrix}. \quad (2.4)$$

Matrix C^{-1} transforms also $z_j \rightarrow \theta_j$ and $\zeta \rightarrow \beta$ in an analogous way². This description will be useful for studying the Jacobian of the lens mapping and its properties in § 2.3.

The lens equation (2.2) attains a simpler form in complex formalism,

$$\zeta = z - \sum_{j=1}^n \frac{\mu_j}{\bar{z} - \bar{z}_j}. \quad (2.5)$$

The positions of images for a given source position are usually found by transforming equation (3.1) to polynomial form purely in terms of z . This can be achieved by taking the complex conjugate of equation (3.1), expressing \bar{z} in terms of z and ζ from it, and substituting back into equation (3.1), obtaining

$$\zeta = z - \sum_{j=1}^n \frac{\mu_j}{\bar{\zeta} - \bar{z}_j + \sum_{k=1}^n \frac{\mu_k}{z - z_k}}. \quad (2.6)$$

The expression on the right-hand side can be converted to a rational function of z by gradual transformation to a common denominator. Multiplying by the final denominator leads to a polynomial equation of degree $n^2 + 1$ for the image position z (e.g., 78).

Such an equation always yields a set of $n^2 + 1$ solutions. However, not all of these are true images. Additional solutions were introduced by the substitution for \bar{z} when deriving equation (2.6), which is not an equivalent step. Only those solutions that satisfy the original lens equation (3.1) correspond to images of the lensed source. The actual number of images for $n > 1$ ranges from $n + 1$ to $5n - 5$ in increments of two (66; 45).

The number of images depends on the position of the source with respect to the caustic, which is a characteristic curve of the lens in the source plane (e.g., 71). When a point source enters the caustic, a pair of images appears and branches off from a point on the critical curve of the lens in the image plane. Conversely, when a point source exits the caustic, a pair of images meets and vanishes at the critical curve. In special cases, when the point source enters or exits the caustic at an intersection point of two or more sections of the caustic, two or more pairs of images may appear or vanish simultaneously at different points along the critical curve.

From the description above, it follows that the critical curve z_{cc} is a degenerate image of the caustic ζ_c . This property is usually used in reverse to find the caustic of the lens by setting $z = z_{cc}$ in equation (3.1). In mathematical terms, the critical curve is defined as the zero set of the Jacobian determinant corresponding to the lens equation (3.1).

For a given image of a point source its flux amplification is given by the reciprocal absolute value of the Jacobian determinant, and its parity is given by the sign of the determinant. Since the Jacobian determinant plays a pivotal role in the analysis of gravitational lensing, we explore its properties in more detail in the following section.

²In case the positions are already in units of θ_E , set $\theta_E = 1$ in equations (2.3) and (2.4).

2.3 The Jacobian and its properties

2.3.1 Definition and global character

The Jacobi matrix in real vectorial lensing notation is defined as

$$J_0 \equiv \frac{\partial (\beta_I, \beta_{II})}{\partial (\theta_I, \theta_{II})}. \quad (2.7)$$

The usual definition of the Jacobi matrix in complex notation is

$$J \equiv \frac{\partial (\zeta, \bar{\zeta})}{\partial (z, \bar{z})}, \quad (2.8)$$

where z and \bar{z} are taken as independent variables (78). The two matrices are connected by the simple transformation

$$J = C J_0 C^{-1}, \quad (2.9)$$

with the matrices C and C^{-1} defined in equations (2.3) and (2.4), respectively. Since equation (2.9) conserves the determinant, $\det J = \det J_0$, all properties of $\det J_0(\boldsymbol{\theta})$ as a real function over the real plane are identical to those of $\det J(z)$ as a real function over the complex plane. The determinant (hereafter the ‘‘Jacobian’’) can thus be viewed and explored as a simple two-dimensional surface.

In the case of our studied lens equation (3.1), the Jacobian simplifies to

$$\det J(z) = \partial_z \zeta \partial_{\bar{z}} \bar{\zeta} - \partial_{\bar{z}} \zeta \partial_z \bar{\zeta} = 1 - |\partial_z \bar{\zeta}|^2 = 1 - \left| \sum_{j=1}^n \frac{\mu_j}{(z - z_j)^2} \right|^2, \quad (2.10)$$

where we used abbreviated notation for partial derivatives, e.g., $\partial_z \zeta \equiv \partial \zeta / \partial z$ (78; 79). From the final expression we immediately see that $\det J(z) \leq 1$ over the entire complex plane. The Jacobian is a continuous smooth function everywhere except at n poles at the positions of the lens components, where $\det J(z_j) = -\infty$. Far from all the lenses, for $|z - z_j| \gg 1$, it approaches unity, $\det J(z) \rightarrow 1$. The set of points with zero Jacobian forms the critical curve of the lens, $\det J(z_{cc}) = 0$.

2.3.2 Stationary points: maxima and saddles

The stationary points of the Jacobian fulfill the condition $\partial_z \det J = 0$. Since the Jacobian is a real function, $\partial_{\bar{z}} \det J = 0$ is then implied automatically. Using equations (3.4) and (3.1) we obtain the expression

$$\partial_z \det J = -\partial_{\bar{z}} \zeta \partial_z^2 \bar{\zeta} = 0, \quad (2.11)$$

where we used abbreviated notation for the second derivative, $\partial_z^2 \bar{\zeta} \equiv \partial^2 \bar{\zeta} / \partial z^2$. Equation (2.11) yields two types of solutions, $\partial_{\bar{z}} \zeta = 0$ and $\partial_z^2 \bar{\zeta} = 0$. The nature of these solutions can be found from the Hessian matrix of the second derivatives along the real and imaginary axes, with components $h_{ij} = \partial^2 \det J_0 / \partial \theta_i \partial \theta_j$ where $i, j = I, II$. Expressed in terms of complex derivatives, the Hessian matrix

$$H = C^T \begin{pmatrix} \partial_z^2 \det J & \partial_{z, \bar{z}}^2 \det J \\ \partial_{\bar{z}, z}^2 \det J & \partial_{\bar{z}}^2 \det J \end{pmatrix} C, \quad (2.12)$$

where C^T is the transpose of matrix C . Substituting for the Jacobian from equation (3.4), we obtain the Hessian determinant

$$\det H = \frac{4}{\theta_E^4} (|\partial_{\bar{z}}^2 \zeta|^4 - |\partial_{\bar{z}} \zeta|^2 |\partial_{\bar{z}}^3 \zeta|^2). \quad (2.13)$$

Note that the Hessian has the opposite sign when compared with the determinant of the central matrix on the right-hand side of equation (2.12).

The stationary points with $\partial_z^2 \bar{\zeta} = 0$ have $\det H = -4\theta_E^{-4} |\partial_{\bar{z}} \zeta|^2 |\partial_{\bar{z}}^3 \zeta|^2 \leq 0$, hence they are saddle points (71; 25) unless $\partial_{\bar{z}} \zeta = 0$ or $\partial_{\bar{z}}^3 \zeta = 0$. In the former case they are higher-order maxima, as shown above. In the latter case they are higher-order saddle points, such as the monkey saddle if $\partial_{\bar{z}}^4 \zeta \neq 0$. In terms of the lens parameters the condition for Jacobian saddle points can be written as

$$\partial_z \bar{\zeta} = \sum_{j=1}^n \frac{\mu_j}{(z - z_j)^2} = 0, \quad (2.14)$$

where we used equation (3.1) and complex conjugation. Multiplication by all denominators converts equation (3.6) to a polynomial of degree $3n - 3$ with highest-degree-term coefficient equal to 1. The n -point-mass lens Jacobian thus has at most $3n - 3$ different saddle points. Some solutions of equation (3.6) may correspond to higher-order maxima, or several solutions may correspond to a higher-order saddle. The saddle points play a key role in determining changes in the topology of the critical curve, as discussed further in § 2.4.

The stationary points with $\partial_z^2 \bar{\zeta} = 0$ have $\det H = -4\theta_E^{-4} |\partial_{\bar{z}} \zeta|^2 |\partial_{\bar{z}}^3 \zeta|^2 \leq 0$, hence they are saddle points (71; 25) unless $\partial_{\bar{z}} \zeta = 0$ or $\partial_{\bar{z}}^3 \zeta = 0$. In the former case they are multiple maxima, as shown above. In the latter case they are higher-order saddle points, such as the monkey saddle if $\partial_{\bar{z}}^4 \zeta \neq 0$. In terms of the lens parameters the condition for Jacobian saddle points can be written as

$$-\frac{1}{2} \partial_z^2 \bar{\zeta} = \sum_{j=1}^n \frac{\mu_j}{(z - z_j)^3} = 0, \quad (2.15)$$

where we used equation (3.1) and complex conjugation. Multiplication by all denominators converts equation (3.6) to a polynomial of degree $3n - 3$ with highest-degree-term coefficient equal to 1. The n -point-mass lens Jacobian thus has at most $3n - 3$ different saddle points. Some solutions of equation (3.6) may correspond to multiple maxima, or several solutions may correspond to a higher-order saddle. The saddle points play a key role in determining changes in the topology of the critical curve, as discussed further in § 2.4.

2.3.3 Jacobian contours and critical curves

The n -point-mass-lens Jacobian has a remarkable property we have not found mentioned in the literature on gravitational lensing. We demonstrate here that all level curves of the Jacobian, seen as contours in the image plane, correspond to critical curves of re-scaled lens configurations. We can show this by taking any level curve of the Jacobian surface, e.g., $\det J(z) = \lambda$, where the Jacobian range restricts the parameter λ to real values $\lambda \leq 1$. Using the last expression for the

Jacobian from equation (3.4), the equation for the corresponding contour in the image plane is

$$1 - \left| \sum_{i=1}^n \frac{\mu_j}{(z - z_j)^2} \right|^2 = \lambda. \quad (2.16)$$

If we subtract λ and divide by $1 - \lambda$, we get

$$1 - \frac{1}{1 - \lambda} \left| \sum_{j=1}^n \frac{\mu_j}{(z - z_j)^2} \right|^2 = 0. \quad (2.17)$$

This step can be taken anywhere except exactly at maxima. There $\lambda = 1$ and the corresponding contours are point-like. Now if we re-scale the image plane including the lens positions by a real positive factor,

$$z' = z \sqrt[4]{1 - \lambda}, \quad z'_j = z_j \sqrt[4]{1 - \lambda}, \quad (2.18)$$

equation (2.17) simplifies to

$$1 - \left| \sum_{j=1}^n \frac{\mu_j}{(z' - z'_j)^2} \right|^2 = 0, \quad (2.19)$$

which is the critical-curve equation for a lens with components at z'_j .

One can proceed similarly the other way round: if we change the scale of a lens configuration by shifting all lens components from z_j to αz_j , where α is a real positive factor, we find that the critical curve is equal to the Jacobian contour $\det J = 1 - \alpha^4$ of the original configuration re-scaled by α .

This property is especially useful for studies of the lensing behavior, and it further enhances the significance of the Jacobian surface. For any particular n -point-mass lens the surface includes as its contours not only the critical curve of the given configuration, but also the critical curves of all directly similar configurations, arbitrarily shrunk or expanded. For values $\lambda \rightarrow -\infty$ in equation (2.16) we get the critical curve of a set of n individual widely separated lenses (the “wide” limit), while for $\lambda \rightarrow 1^-$ we get the critical curve of a combined lens with all components approaching a single point (the “close” limit), as can be seen from equation (2.18).

In Figure 2.1 we demonstrate the Jacobian contour \leftrightarrow critical curve correspondence on the example of a two-point-mass lens (hereafter for simplicity “binary” lens) with masses $\mu_1 = 4/5$ and $\mu_2 = 1/5$ separated by $s_0 = 1$ Einstein radius. In the left panel we plotted the Jacobian surface $\det J(z)$, with its “trunks” around the lens positions truncated at $\det J = -15$. On the surface we marked a sequence of Jacobian contours specified in the caption. The highest contours outside the upper self-intersecting $\det J = 0.711$ contour each have two additional small loops around the positions of the two Jacobian maxima. The three saddle points of the Jacobian surface lie at the self-intersection points of this contour and of the lowermost $\det J = -11.0$ contour.

In the right panel we plotted the same contours as seen from above in the image plane, adding the innermost $\det J = -100$ curve that would lie below the plot in the left panel. For illustration, selected curves corresponding to Jacobian values marked in the caption in boldface are labeled by the re-scaled binary

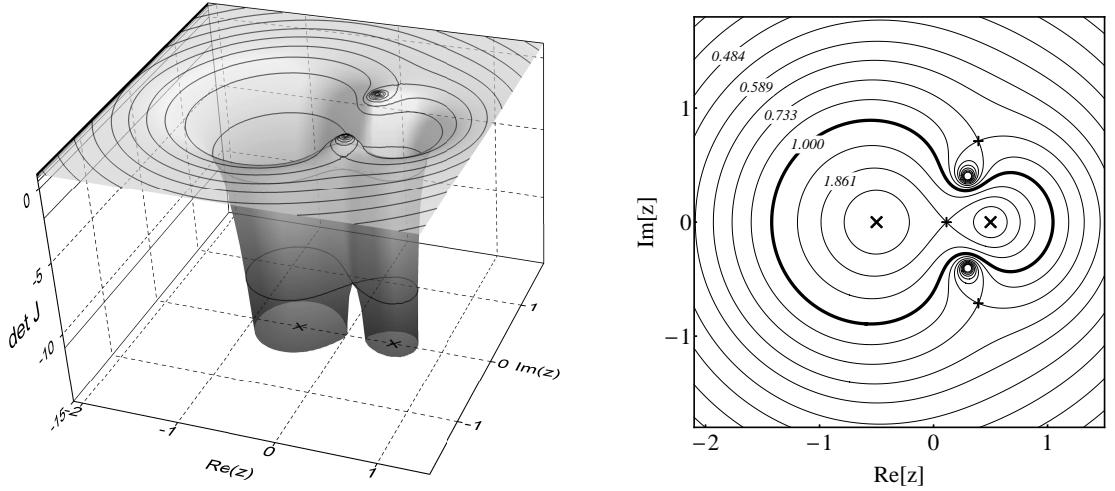


Figure 2.1 Correspondence of Jacobian contours and critical curves of re-scaled lens configurations, illustrated on a binary lens with fractional masses $\{\mu_1, \mu_2\} = \{4/5, 1/5\}$ and positions $\{z_1, z_2\} = \{-1/2, 1/2\}$, i.e., separation $s_0 = 1$. Left panel: Jacobian surface of lens plotted over the image plane z , truncated below at $\det J = -15$, with contours plotted for $\det J \in \{-11.0, -2, 0, 0.5, \mathbf{0.711}, 0.82, \mathbf{0.88}, 0.92, \mathbf{0.945}, 0.962, 0.973\}$. Right panel: same contours with additional innermost $\det J = -100$ plotted in image plane, with the critical curve plotted in bold. Each contour is identically equal to the critical curve of a binary lens with separation and units on axes multiplied by $\sqrt[4]{1 - \det J}$. Several separation values are included as labels for Jacobian contours listed in bold. Crosses: lens components; pluses: Jacobian saddle points. The two Jacobian maxima lie within the off-axis critical-curve loop sequences.

separation $s_0 \sqrt[4]{1 - \det J}$. The given contour is identically equal to the critical curve in a similarly re-scaled image plane.

The right panel may also be viewed as a sequence of critical-curve plots for lenses with the same mass ratio and different separations s , with the position in the image plane measured in units of s instead of θ_E . Finally, the sequence of curves also corresponds to holding the absolute angular separation $s\theta_E$ fixed and changing the angular Einstein radius θ_E (e.g., by varying the total mass of the lens M_{tot} , or any of the distances D_s, D_l, D_{ls}).

Note that the positions of Jacobian maxima and saddle points scale together with the lens positions, i.e., their relative configuration stays fixed with the lens components. This can be seen from equations (2.14) and (3.6), in which any scaling factor in the denominator drops out due to the zero right-hand side, so that both equations retain their form. The correspondence with contours of the Jacobian surface in the left panel of Figure 2.1 provides the best illustration: the maxima and saddle points are defined globally just like the lens positions, irrespective of which of the contours is the critical curve.

2.4 The n -point-mass lens critical curve

2.4.1 Critical-curve topology

The critical curve z_{cc} is the set of all points in the image plane with zero Jacobian. Using the second expression for the Jacobian from equation (3.4), we can write the general critical-curve condition in the compact form

$$\partial_z \zeta \partial_z \bar{\zeta} = 1. \quad (2.20)$$

If we multiply the last expression in equation (3.4) by all the denominators, we see that for $n \geq 2$ the critical curve is a real algebraic curve of order $4n$. The same expression also indicates that the zero-Jacobian condition is satisfied if the derivative $\partial_z \bar{\zeta}$ lies anywhere along the unit circle. Hence, the points of the critical curve are the solutions of

$$\sum_{j=1}^n \frac{\mu_j}{(z - z_j)^2} = e^{-2i\phi}, \quad (2.21)$$

where $\phi \in [0, \pi)$ is a phase parameter (78). The normalization of the phase is arbitrary; in our choice one gets the single-lens critical curve in the form $z_{cc} = z_1 \pm \sqrt{\mu_1} e^{i\phi}$.

The critical-curve equation (3.2) can be multiplied by all the denominators to yield a polynomial equation of degree $2n$. It follows that for any value of ϕ there are up to $2n$ different solutions of equation (3.2). By varying the phase from 0 to π the solutions trace out $2n$ continuous critical-curve segments in the image plane. The choice of sign of the phase in equation (3.2) ensures that while tracing any segment in the sense of increasing ϕ , the Jacobian is positive on its right side, negative on its left side. This can be shown by differentiating equations (3.4) and (3.2) to obtain

$$\det J(z_0 \mp idz) = \pm 4 d\phi, \quad (2.22)$$

where z_0 is a point on the critical curve, and dz is a tangential shift along the critical curve corresponding to phase shift $d\phi$. With this notation $z_0 \mp idz$ are points offset perpendicularly to the right or left, respectively, from the tangential shift dz .

The segments connect together in groups of 1 to $2n$ to form closed loops, the full set of which constitutes the critical curve. This follows from the continuous and periodic dependence of equation (3.2) on ϕ , together with the fact that the critical curve avoids poles and complex infinity, $z \neq z_j, \infty$.

From the limitations on the number of segments per loop it follows that the number of loops of the critical curve may be as low as one (as in the case of the single lens or the intermediate binary lens), but not higher than $2n$ (78). Individual loops may lie outside one another (as in the wide binary lens), or some may lie nested in another (as in the close binary lens). The number of loops and their mutual position together define the topology of the critical curve.

The topology of the critical curve determines the structure of the caustic, which in turn determines the number of images as well as the structure of observable light curves in microlensing events. The topology depends on the parameters of the n -point-mass lens, i.e., on the masses and positions of the individual components. The actual number of relevant parameters for $n > 1$ is reduced from $3n$ to $3n - 4$, after accounting for the freedom of choice of the coordinate system (i.e., its origin, orientation, and position-measurement unit). Mapping the critical-curve topology in this parameter space is a crucial step towards understanding the nature of lensing by an n -point-mass lens.

2.4.2 Identifying topology changes in parameter space

In order to map the critical-curve topology in the parameter space of the lens, we follow the approach of (25) and (79), and identify parameter combinations that correspond to changes in the topology. These combinations define boundaries of regions with specific topologies in the parameter space. In order to find them we first note that individual loops of the critical curve are typically disconnected and have no self-intersections. Intersections occur only at the boundaries, where the topology changes by the splitting or merging of loops.

The critical curve, viewed as the $\det J = 0$ Jacobian contour, separates regions of positive and negative Jacobian in the image plane. Therefore, at a simple intersection point on a critical curve where two loops meet, there is a facing pair of positive regions and a facing pair of negative regions. At the intersection the Jacobian peaks at zero when crossing from one negative region to the other. At the same time it drops there to zero when crossing from one positive region to the other. Hence, such an intersection must be a saddle point of $\det J$ (e.g., 71). In case three loops meet at an intersection point, the Jacobian does change sign but undergoes an inflexion when crossing it. The three-fold symmetry forms a monkey saddle on the surface, as mentioned in § 2.3.2. Similarly, higher-order intersections of the critical curve correspond to higher-order saddles on the Jacobian surface. Generally, intersections of any order must simultaneously satisfy the saddle-point equation (3.6) as well as the critical-curve equation (3.2).

The transitions in parameter space can be illustrated on the example of the binary lens in Figure 2.1. For lens separations $s > 1.861$ the critical curve consists

of two separate loops around the lenses. At $s \approx 1.861$ the critical curve passes through a saddle point, at which the two loops come into contact. For lens separations $1.861 > s > 0.733$ the critical curve consists of a single merged loop surrounding both lenses. At $s \approx 0.733$ the critical curve self-intersects at a symmetric pair of saddle points, splitting off two small loops. For lens separations $s < 0.733$ the critical curve consists of an outer loop plus two small loops surrounding the maxima of the Jacobian. Overall, for the given mass ratio the different topologies are separated by boundaries at $s \approx 1.861$ and $s \approx 0.733$, at which the critical curve passes through saddle points of the Jacobian.

As discussed in § 2.3.2, the n -point-mass lens may have up to $3n - 3$ different saddle points z_{sadd} . Each of them lies on a Jacobian contour $\det J(z) = \det J(z_{sadd})$. While in the binary lens two of the three saddles lie on the same contour, for higher n there may be in principle up to $3n - 3$ different contours dividing the image plane into regions with different critical-curve topology. Taking into account the scaling properties discussed in § 2.3.3, this means that any lens configuration may undergo up to $3n - 3$ topology changes when changing its scale from the “wide” to the “close” limit. By configuration we mean here fixed relative masses and positions of the components except an absolute scale. This property can greatly simplify the mapping of critical-curve topologies for different n -point-mass lens models, as demonstrated in the companion paper (22).

2.5 The n -point-mass lens caustic

2.5.1 Caustic structure and cusp number

The caustic ζ_c is a characteristic curve of the lens, defined as the set of all points in the source plane with infinite point-source amplification. Since the amplification of an image is the inverse absolute value of its Jacobian, the caustic must have an image with zero Jacobian. Indeed, in addition to regular images the caustic has a degenerate image, the critical curve z_{cc} .

If we know the critical curve, the caustic can be obtained simply from the lens equation

$$\zeta_c = z_{cc} - \sum_{j=1}^n \frac{\mu_j}{\bar{z}_{cc} - \bar{z}_j}. \quad (2.23)$$

Since the critical curve passes neither through lens positions, nor through complex infinity, the simple continuous transformation in equation (3.3) preserves various properties of the critical curve. For example, each loop of the critical curve corresponds to a loop of the caustic, so that the number of loops is identical. The boundaries in parameter space corresponding to changes in critical-curve topology thus also correspond to changes in the number of caustic loops.

Unlike for single or binary lenses, the mapping between the critical curve and the caustic given by equation (3.3) for lenses with $n \geq 3$ components is not always one-to-one. Different points of the critical curve may be mapped onto the same point of the caustic. As a result, loops of the caustic may intersect each other, and individual loops may self-intersect. While following a path in parameter space, a caustic loop may move from the inside of another loop and cross it to the outside without a change in the number of loops. Hence, the mutual position of

loops does not play the same role as in the critical curve, where the only contact between loops occurs at points where the loop number changes. The mutual position of caustic loops does play a role in identifying the number of images of the background source, which changes when crossing the caustic, as described in § 2.2. The caustic thus plays the role of a boundary between regions of the source plane with different numbers of images.

Another distinction of the caustic from the critical curve is its lack of smoothness. Within our n -point-mass lens model given by equation (2.2), all loops of the caustic have cusps, sharp points at which the tangent-vector orientation changes by π . The smooth parts of the caustic between cusps are called folds. The number of cusps of a given caustic loop changes only under special local caustic metamorphoses.

The range of possible metamorphoses expands when increasing the number of lens components. The binary lens with $n = 2$ permits only the simplest beak-to-beak metamorphosis, in which two tangent folds reconnect and form two facing cusps. This metamorphosis corresponds to a change in critical-curve topology; the boundaries are thus identical.

All higher-order metamorphoses occur without any accompanying change in the critical-curve topology. For lenses with $n = 3$ components, two additional metamorphoses may occur. In the swallow-tail metamorphosis two cusps and a self-intersection arise from a point along a fold. In the butterfly metamorphosis two additional cusps and three self-intersections arise from a cusp.

In the rest of this section we concentrate on identifying the conditions under which caustic metamorphoses occur. In the parameter space they define boundaries that form a finer subdivision of the critical-curve topology regions discussed in § 2.4.2 according to the number of cusps of the caustic.

2.5.2 Cusp condition

Cusps of the caustic are points at which the caustic tangent changes phase by π . Since the caustic is computed from the critical curve following equation (3.3), we derive the tangent to the caustic from the tangent to the critical curve.

We start with the gradient of the Jacobian in complex notation,

$$G_z = \frac{\partial \det J}{\partial \operatorname{Re}[z]} + i \frac{\partial \det J}{\partial \operatorname{Im}[z]} = 2 \partial_z \det J. \quad (2.24)$$

The critical curve is a contour of the Jacobian, hence its tangent is perpendicular to the gradient. We define the tangent to the critical curve as

$$T_z = i G_z = 2 i \partial_z \det J, \quad (2.25)$$

evaluated along the critical curve (78). In this definition the absolute value of T_z is equal to the absolute value of the gradient at the given point. This implies that the only points that may occur along the critical curve with $T_z = 0$ are Jacobian saddle points. Critical-curve loops meet there for lens parameters at the boundaries studied in § 2.4.2.

The orientation of T_z is such that the Jacobian increases (i.e., is positive) to its right and decreases (i.e., is negative) to its left. For our lens equation (3.1)

we may use the complex conjugate of the left equality from equation (2.11) to obtain

$$T_z = -2i \partial_z \bar{\zeta} \partial_{\bar{z}}^2 \zeta. \quad (2.26)$$

Using the Jacobi matrix J from equation (2.8) we compute the tangent to the caustic T_ζ from the transformation

$$\begin{pmatrix} T_\zeta \\ \bar{T}_\zeta \end{pmatrix} = J \begin{pmatrix} T_z \\ \bar{T}_z \end{pmatrix}, \quad (2.27)$$

which gives us (78)

$$T_\zeta = T_z \partial_z \zeta + \bar{T}_z \partial_{\bar{z}} \zeta. \quad (2.28)$$

Using the lens equation (3.1) and equation (2.26), we obtain

$$T_\zeta = 2i [(\partial_z \zeta)^2 \partial_z^2 \bar{\zeta} - \partial_z \bar{\zeta} \partial_{\bar{z}}^2 \zeta]. \quad (2.29)$$

As we trace the critical curve, the right-hand side of equation (2.29) changes continuously, since the critical curve avoids the singularities at the lens positions. The only way in which the argument of T_ζ may change abruptly by π is when $|T_\zeta|$ shrinks to zero. Therefore, cusps occur at points along the caustic where $T_\zeta = 0$.

Using equation (2.29) we conclude that in the image plane, cusps correspond to points along the critical curve which fulfill the cusp condition

$$(\partial_z \zeta)^2 \partial_z^2 \bar{\zeta} = \partial_z \bar{\zeta} \partial_{\bar{z}}^2 \zeta. \quad (2.30)$$

2.5.3 The cusp curve and its properties

If we multiply equation (2.30) by $\partial_z^2 \bar{\zeta} (\partial_z \bar{\zeta})^2$ and utilize the critical-curve equation (2.20), we get

$$(\partial_z^2 \bar{\zeta})^2 = |\partial_z^2 \bar{\zeta}|^2 (\partial_z \bar{\zeta})^3. \quad (2.31)$$

We note that for Jacobian saddle points $\partial_z^2 \bar{\zeta} = 0$, so that both sides of equations (2.30) and (2.31) are equal to zero. If a saddle lies on the critical curve, it corresponds to cusp images. At such points in the image plane loops of the critical curve meet, while in the source plane cusps meet in a beak-to-beak metamorphosis, as discussed in § 2.5.1.

For all other solutions we divide equation (2.31) by the first term on the right-hand side. From equation (3.2) we know that the last term on the right-hand side lies on the unit circle for critical-curve points. We may thus write the result as

$$\arg [(\partial_z^2 \bar{\zeta})^2] = \arg [\partial_z \bar{\zeta}]^3, \quad (2.32)$$

an equation involving only the arguments (phases) of the powers of lens-equation derivatives. An equivalent formulation of equation (2.32) is

$$(\partial_z^2 \bar{\zeta})^2 = 4 \Lambda (\partial_z \bar{\zeta})^3, \quad (2.33)$$

where Λ is a real non-negative parameter, as seen from equation (2.31). In view of the one degree of freedom, equation (2.32) or (2.33) describes a curve in the image plane which intersects the critical curve at the positions of cusp images. For brevity we call it the cusp curve.

If we compute the derivatives of $\bar{\zeta}$ using lens equation (3.1), equations (2.32) and (2.33) can be converted to

$$\arg \left[\sum_{j=1}^n \frac{\mu_j}{(z - z_j)^3} \right]^2 = \arg \left[\sum_{j=1}^n \frac{\mu_j}{(z - z_j)^2} \right]^3, \quad (2.34)$$

and

$$\left[\sum_{j=1}^n \frac{\mu_j}{(z - z_j)^3} \right]^2 = \Lambda \left[\sum_{j=1}^n \frac{\mu_j}{(z - z_j)^2} \right]^3. \quad (2.35)$$

The latter equation can be converted to a polynomial of degree $6n - 6$, so that varying Λ from 0 to ∞ yields up to $6n - 6$ branches of the cusp curve. The cusp curve connects all important points of the image plane: the lens positions, Jacobian maxima, Jacobian saddle points, and complex infinity. The value $\Lambda = 0$ corresponds uniquely to the saddle points (up to $3n - 3$ different ones), and $\Lambda = \infty$ uniquely to the maxima (up to $2n - 2$ different ones). Complex infinity corresponds to several roots at $\Lambda = 1$. Similarly, each lens position z_j corresponds to several roots at $\Lambda = 1/\mu_j$.

Changing the scale in the image plane $(z, z_j) \rightarrow \alpha(z, z_j)$ leaves equations (2.34) and (3.27) unchanged, which means the cusp curve is scale-invariant. Therefore, when added to a Jacobian-contour plot such as the right panel of Figure 2.1, it will intersect all contours (i.e., re-scaled critical curves) at the positions of cusp images. A single plot can thus illustrate the number and distribution of cusps not only for the given lens configuration, but simultaneously also for all arbitrarily shrunk or expanded configurations. We point out here that the initial forms of the cusp condition in equations (2.30) and (2.31) are not scale-invariant, hence they cannot be used in the same way.

For illustration we present in the left panel of Figure 2.2 the cusp curve of the binary lens from Figure 2.1 with $\mu_1 = 4/5$ and $s_0 = 1$. The curve can be constructed from 6 branches starting at the saddle points and ending at the maxima, with some branches turning en route at the lens positions (two branches through each) or at complex infinity (two branches proceeding to either lens). The intersections of the cusp curve with the critical curve show the positions of cusp images, hence the corresponding caustic has six cusps.

Intersections with the other contours show us the positions of cusp images for re-scaled lens configurations (in this case for different binary separations s). The number of cusps changes in this case only through beak-to-beak metamorphoses that occur here for separations $s \approx 1.861$ and $s \approx 0.733$ (see also discussion in § 2.4.2). If we increase the separation to $s > 1.861$, two additional cusps appear between the lenses, as shown by the contour closest to the lenses. The two loops of the critical curve each have four intersections, hence the two caustic loops have four cusps each. On the other hand, if we reduce the separation to $s < 0.733$, two additional pairs of cusps appear outwards from the off-axis saddle points. The outer loop of the critical curve has four intersections (its caustic loop has four cusps); the two small loops around the maxima have three intersections each (their caustic loops have three cusps each).

The geometry of the cusp curve and the sequence of caustic transitions remains the same for any two-point-mass lens. Adding a third component to the lens

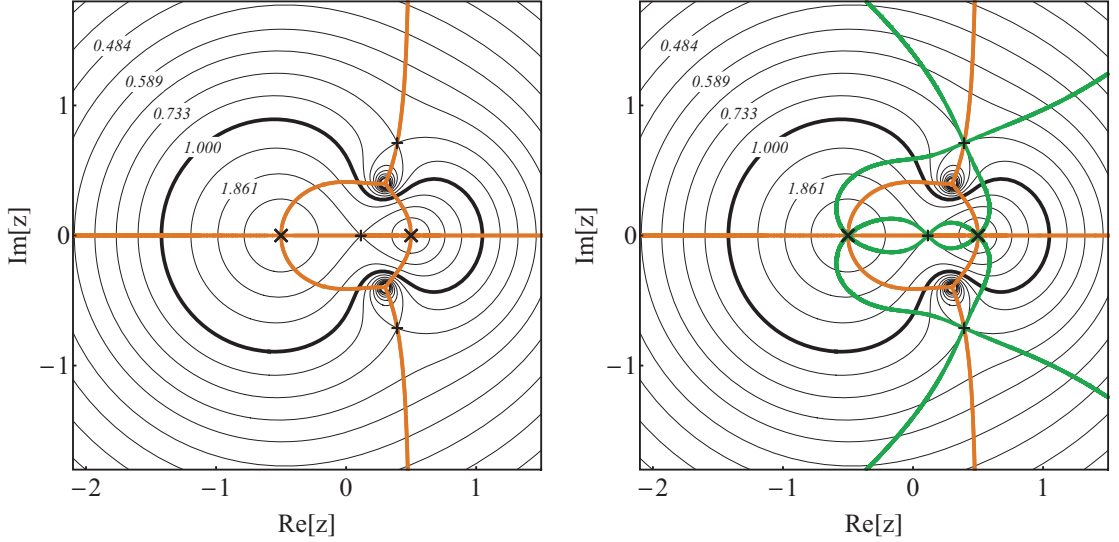


Figure 2.2 Cusp curve (orange) and morph curve (green) of the binary lens from Figure 2.1. The cusp curve intersects Jacobian contours at the positions of cusp images along the critical curves of the corresponding re-scaled lens configurations. The morph curve intersects the cusp curve at the lens positions and at the images of caustic-metamorphosis points for the corresponding re-scaled lens configurations. For a sequence of contours progressing through any such point the number of cusps on the corresponding caustics changes (see also Figure 2.5). Here the intersections at Jacobian saddle points correspond to beak-to-beak metamorphoses. Notation as in Figure 2.1.

opens up a range of different geometries, as illustrated by the examples in § 2.6 and in (22). The cusp curve then becomes a useful guide for understanding the occurrence of different caustic metamorphoses, and for keeping track of the cusp number on individual caustic loops.

2.5.4 Caustic metamorphoses and the morph curve

When changing the scale of a given lens configuration, the local appearance of two additional cusps other than at beak-to-beak metamorphoses may be detected in the image plane by finding points where the cusp curve is tangent to the local Jacobian contour. For a simple tangent point, contours adjacent from one side have no intersection with the cusp curve while contours adjacent from the opposite side each have two intersections. Such a configuration corresponds to the swallow-tail metamorphosis.

If the tangent point occurs at a simple self-intersection point of the cusp curve away from saddle points, contours adjacent from one side have one intersection with the cusp curve while contours adjacent from the opposite side each have three intersections. Such a configuration corresponds to the butterfly metamorphosis.

The appearance of additional cusps at a point on the caustic requires stationarity of the caustic tangent T_ζ at the corresponding point in the image plane when moving along the critical curve (e.g., 59). This requirement implies the condition

$$(T_z \partial_z + \bar{T}_z \partial_{\bar{z}}) T_\zeta = 0, \quad (2.36)$$

which must be fulfilled in addition to the critical-curve equation (2.20) and the cusp condition given by equation (2.30).

In the case of our lens equation (3.1) we can substitute from equations (2.25) and (2.28) for the tangents T_z and $T_{\bar{\zeta}}$, respectively. Equation (2.36) can then be written in the somewhat ungainly form

$$\partial_z \bar{\zeta} \partial_{\bar{z}}^2 \zeta \left[\partial_{\bar{z}}^2 \zeta \partial_z^2 \bar{\zeta} - (\partial_{\bar{z}} \zeta)^2 \partial_z^3 \bar{\zeta} \right] = \partial_z \zeta \partial_z^2 \bar{\zeta} \left[\partial_z \bar{\zeta} \partial_{\bar{z}}^3 \zeta - 2 \partial_z \zeta \partial_{\bar{z}}^2 \zeta \partial_z^2 \bar{\zeta} \right]. \quad (2.37)$$

The terms before the brackets indicate that all stationary points of the Jacobian are among the solutions of equation (2.36). Here we seek other solutions, such as the swallow-tail and butterfly metamorphosis points. In order to find them we simplify equation (2.37) utilizing the critical-curve and cusp conditions.

We first multiply equation (2.37) by $\partial_z^2 \bar{\zeta}$ and substitute for $(\partial_{\bar{z}} \zeta)^2 \partial_z^2 \bar{\zeta}$ in the second terms on both sides of the equation using the cusp equation (2.30). Next we multiply the obtained equation by $\partial_z \zeta$, which cancels out $\partial_z \bar{\zeta}$ on the left-hand side as well as in both terms on the right-hand side, due to the critical-curve equation (2.20). Now we have

$$(\partial_z^2 \zeta)^2 (\partial_z^2 \bar{\zeta})^2 - \partial_z \bar{\zeta} (\partial_z^2 \zeta)^2 \partial_z^3 \bar{\zeta} = \partial_z \zeta (\partial_z^2 \bar{\zeta})^2 \partial_z^3 \zeta - 2 (\partial_z^2 \zeta)^2 (\partial_z^2 \bar{\zeta})^2. \quad (2.38)$$

The second term on the right-hand side can be added to the first on the left-hand side. If we divide the equation by $|\partial_z^2 \bar{\zeta}|^4$ and transfer the second term on the left-hand side to the right-hand side, we are left with the real equation

$$3 = \text{Re} \left[2 \partial_z \bar{\zeta} (\partial_z^2 \bar{\zeta})^{-2} \partial_z^3 \bar{\zeta} \right]. \quad (2.39)$$

Since the imaginary part of the expression in the square brackets is not constrained by the equation and thus may be arbitrary, we parameterize it as $3i\Gamma$, where Γ is a real parameter. We may now write

$$2 \partial_z \bar{\zeta} \partial_z^3 \bar{\zeta} = 3 (\partial_z^2 \bar{\zeta})^2 (1 + i\Gamma). \quad (2.40)$$

We first note that in case the Jacobian has higher-order maxima or higher-order saddles (see § 2.3.2), they will solve equation (2.40) for any Γ . Maxima never lie on the critical curve, while saddles always correspond to topology-changing beak-to-beak metamorphoses (with more beaks involved in the case of higher-order saddles).

Setting these isolated points aside, equation (2.39) is a real equation in the complex plane depending both on z and \bar{z} , while equation (2.40) is a complex parametric equation for z . Both describe the same curve, which we call the morph curve. It passes through the critical-curve points corresponding to all caustic-metamorphosis points, such as beak-to-beak, swallow-tail, and butterfly. In addition, it passes through the lens positions and complex infinity.

If we compute the derivatives of $\bar{\zeta}$ and ζ using lens equation (3.1), equations (2.39) and (2.40) can be converted to

$$1 = \text{Re} \left\{ \left[\sum_{j=1}^n \frac{\mu_j}{(z - z_j)^2} \right] \left[\sum_{j=1}^n \frac{\mu_j}{(z - z_j)^3} \right]^{-2} \left[\sum_{j=1}^n \frac{\mu_j}{(z - z_j)^4} \right] \right\}, \quad (2.41)$$

and

$$\left[\sum_{j=1}^n \frac{\mu_j}{(z - z_j)^2} \right] \left[\sum_{j=1}^n \frac{\mu_j}{(z - z_j)^4} \right] = (1 + i\Gamma) \left[\sum_{j=1}^n \frac{\mu_j}{(z - z_j)^3} \right]^2, \quad (2.42)$$

respectively. Multiplying the latter equation by all denominators converts it to a polynomial of degree $6n - 6$, so that varying Γ from $-\infty$ to ∞ yields up to $6n - 6$ branches of the morph curve. The values $\Gamma = -\infty$ and $\Gamma = \infty$ correspond uniquely to the saddle points (up to $3n - 3$ different ones). Each simple saddle point is crossed twice in perpendicular directions by the morph curve, monkey saddles are crossed symmetrically three times, higher-order saddles a corresponding higher number times. Turning around any saddle point, the arriving morph-curve parameters alternate between $\Gamma = -\infty$ and $\Gamma = \infty$. Complex infinity and the lens positions each correspond to a pair of roots at $\Gamma = 0$.

From both versions of the morph-curve equation it is clear that changing the scale in the image plane $(z, z_j) \rightarrow \alpha(z, z_j)$ leaves equations (2.41) and (3.28) unchanged, which means that even the morph curve is scale-invariant. We can therefore add it to Jacobian-contour plots and identify its intersections with the cusp curve away from the lens positions. Intersections at the saddle points identify the topology-changing beak-to-beak metamorphoses studied earlier. Simple intersections away from saddle points identify swallow-tail metamorphoses. Tangent intersections of a single morph-curve branch at a simple cusp-curve self-intersection point identify butterfly metamorphoses. For any of these points, the Jacobian contour passing through it identifies the scale of the lens configuration at which the metamorphosis occurs.

2.5.5 Distinguishing butterflies from swallow tails

In order to distinguish between swallow-tail and butterfly metamorphoses, we first check the condition for self-intersection points on the cusp curve. An arbitrarily small circle around such a point must have more than two intersections with the cusp curve defined by equation (2.34). By expanding the equation we obtain the condition

$$3 = 2 \partial_z \bar{\zeta} (\partial_z^2 \bar{\zeta})^{-2} \partial_z^3 \bar{\zeta}. \quad (2.43)$$

Comparing this self-intersection condition with the morph curve equation (2.40), we find that all butterfly points must be morph-curve points with $\Gamma = 0$. From the discussion above we know that for $\Gamma = 0$ the morph curve has $2n$ roots at the lens positions plus 2 roots at complex infinity. It follows that a given lens configuration may have at most $4n - 8$ butterfly points.

Butterfly metamorphoses additionally require the critical curve to be tangent to one of the branches of the cusp curve. Expanding the critical-curve equation (2.20) to first order around its point z_0 away from saddles, we get its tangent

$$z_{cc} \simeq z_0 + i (\partial_z \zeta \partial_z^2 \bar{\zeta})^{-1} \varepsilon_1, \quad (2.44)$$

where all derivatives are computed at z_0 , and the real parameter ε_1 varies along the tangent. Similarly, we expand the cusp-curve equation (2.32) to first order around a self-intersection point away from maxima and lens positions. The

tangents of its two branches are

$$z_{cusp\pm} \simeq z_0 + e^{i(-2\psi\pm\pi)/4} \varepsilon_2, \quad (2.45)$$

where the phase

$$\psi = \arg \left\{ i \left[3(\partial_z^2 \bar{\zeta})^3 - \partial_z^4 \bar{\zeta} (\partial_z \bar{\zeta})^2 \right] \left[(\partial_z \bar{\zeta})^2 \partial_z^2 \bar{\zeta} \right]^{-1} \right\}, \quad (2.46)$$

all derivatives are computed at z_0 , and the real parameter ε_2 varies along the tangent. For one of the two perpendicular tangents to be equal to the critical-curve tangent, the first-order terms of the expansions in equations (2.44) and (2.45) must have the same argument in the complex plane (up to an integer multiple of π). Setting the arguments equal and using equations (2.20) and (2.31) we derive the condition

$$\text{Im} \left[\partial_z^4 \bar{\zeta} (\partial_z \bar{\zeta} \partial_z^2 \bar{\zeta})^{-1} \right] = 0. \quad (2.47)$$

Any $\Gamma = 0$ morph-curve intersection with the cusp curve has to be checked using this tangency condition, to make sure the metamorphosis is a butterfly rather than a pair of swallow tails.

In the rare case when the critical and cusp curves additionally have the same curvature at their tangent intersection point, the condition in equation (2.47) is not sufficient. The described technique then has to be extended by comparing higher-order expansions of the curves. Generally, a butterfly-like transition from one to three intersections occurs if the first difference between the expansions appears at an even order. Note that the equality of each order of the expansions introduces an additional constraint on the lens parameters. Such situations would therefore occur in lenses with a sufficiently high dimension of their parameter space (i.e., with a higher number of components).

Finally, we have to check whether we are at a simple self-intersection of the cusp curve, since equation (2.43) describes even higher order self-intersections with three or more intersecting branches. This final condition for the butterfly metamorphosis is

$$\partial_z^4 \bar{\zeta} \neq 3 (\partial_z \bar{\zeta})^{-2} (\partial_z^2 \bar{\zeta})^3. \quad (2.48)$$

Violation of this condition would lead to higher-order metamorphoses, which can be analyzed in a similar manner. Nevertheless, they do not occur in the triple lens and their exploration goes beyond the scope of this paper.

To summarize, the butterfly metamorphosis occurs when the critical curve intersects the cusp curve so that it passes as a tangent through a self-intersection point involving exactly two branches of the cusp curve. The conditions on the first through fourth derivatives of the lens equation are given by equations (2.20), (2.32), (2.43), (2.47), and (2.48). Mapping the self-intersection back to the source plane using lens equation (3.1) yields the position of the butterfly metamorphosis point on the caustic.

2.6 Lens analysis using cusp and morph curves

In the right panel of Figure 2.2 we present the morph curve of the binary lens from Figure 2.1 plotted together with the cusp curve. Their five mutual intersection

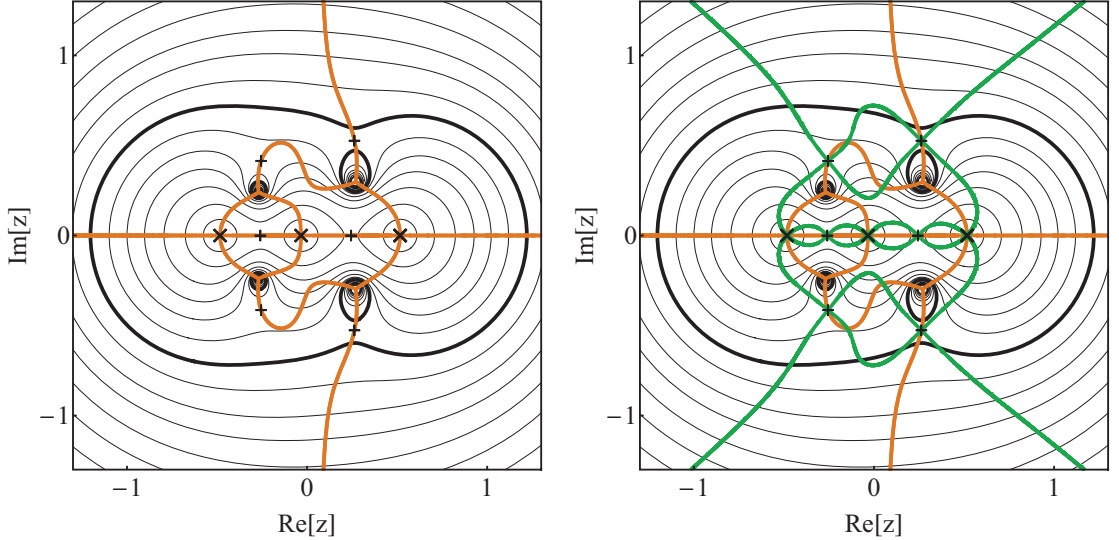


Figure 2.3 Swallow-tail metamorphosis in the image plane: cusp curve (orange) and morph curve (green) of an equal-mass triple lens with positions $\{z_1, z_2, z_3\} = \{-29, -2, 31\} s/30$, where $s = 0.5$. Jacobian contours are plotted outward from the lenses for $\det J \in \{-1599, -99, -16.6, -5.25, -2.06, -0.69, 0, 0.36, 0.578, 0.698, 0.788, 0.848, 0.891\}$. The cusp-curve branch connecting the two Jacobian maxima above the real axis and its mirror counterpart below the real axis each pass through two points where they are tangent to the contours. These points, pinpointed in the right panel as simple intersections with the morph curve, correspond to swallow-tail metamorphoses. There are six additional saddle-point intersections corresponding to beak-to-beak metamorphoses. Notation as in Figure 2.1.

points include the two lens positions and the three Jacobian saddles. At the lens positions the incoming cusp-curve branches alternate with the morph-curve branches. At the (simple) saddle points the cusp curve crosses the intersecting morph-curve branches, identifying the occurrence of beak-to-beak metamorphoses for correspondingly re-scaled lens configurations. The morph curve has the same geometry for all two-point-mass lenses, marking the positions of the three beak-to-beak metamorphosis-point images along the respective Jacobian contours (re-scaled critical curves).

As mentioned above in § 2.5.1, swallow-tail and butterfly metamorphoses occur in n -point-mass lenses starting from $n = 3$. We note here that they occur already for a two-point-mass lens with non-zero external shear, as shown by (32). Such a model is relevant to the present work as a limiting case of a two-point-mass lens weakly perturbed by a third component. In Figure 2.3 we illustrate the swallow-tail case as seen in the image plane of a triple equal-mass lens in a linear configuration with lens positions $\{z_1, z_2, z_3\} = \{-29/30, -2/30, 31/30\} s$ for $s = 0.5$. Here the scale parameter s is one half of the separation of the two outer lenses.

The Jacobian surface has a generic triple-lens topology with 4 maxima and 6 saddle points, which correspond to beak-to-beak metamorphoses as indicated by the intersections of the cusp and morph curves in the right panel. In addition, there are 4 simple intersections of the cusp and morph curves in the right panel,

seen also in the left panel as points where the cusp curve is tangent to Jacobian contours (two pairs above and below the axis between the maxima). Since they occur away from cusp-curve self-intersections, they correspond to swallow-tail metamorphoses.

We can now directly read off the sequence of gradual caustic changes from Figure 2.3, as we vary the scale of the lens from the wide to the close limit. In the figure this corresponds to progressing from lowest to highest Jacobian contour, starting from the small loops around the lenses. In the wide limit the caustic has three loops with 4 cusps each. The loops corresponding to the two left bodies merge through a beak-to-beak metamorphosis forming a loop with 6 cusps. Another beak-to-beak metamorphosis merges it with the third-body loop, leaving a single 8-cusped loop.

The critical curve then reaches the symmetric pair of swallow-tail points closer to the lens axis. Two simultaneous swallow-tail metamorphoses add 4 cusps to form a single 12-cusped loop. Next comes the symmetric pair of saddle points near the two left maxima. Two simultaneous beak-to-beak metamorphoses split off two 3-cusped loops, leaving a third 10-cusped caustic loop. The symmetric pair of swallow-tail points further from the lens axis changes the third loop by two simultaneous swallow-tail metamorphoses removing 4 cusps, so that it is left with only 6 cusps. The symmetric pair of saddle points near the two right maxima leads to the final pair of simultaneous beak-to-beak metamorphoses, splitting off two more 3-cusped loops and thus removing two cusps from the 6-cusped loop. In the close limit the caustic has four 3-cusped loops and a single 4-cusped loop.

In Figure 2.4 we illustrate the butterfly metamorphosis in the image plane of a similar triple equal-mass lens, in a linear configuration but with symmetric lens positions $\{z_1, z_2, z_3\} = \{-1, 0, 1\}$ for $s = 0.5$. Even in this case the Jacobian has 4 maxima and 6 saddle points, which correspond to beak-to-beak metamorphoses indicated by the intersections of the cusp and morph curves in the right panel. In addition, there are 4 intersections along the imaginary axis in the right panel, each with a single branch of the morph curve passing through a self-intersection point of the cusp curve. In the left panel we see them as points where one branch of the cusp curve at a simple self-intersection point (away from lens positions and Jacobian maxima) is tangent to the local Jacobian contour. This confirms the intersections correspond to butterfly metamorphoses.

The sequence of gradual caustic changes is simpler here as we vary the scale of the lens from the wide to close limit, due to the higher degree of symmetry of the lens. In the wide limit the caustic has three loops around the lens components with 4 cusps each. All loops merge through two simultaneous beak-to-beak metamorphoses forming a loop with 8 cusps. Two simultaneous butterfly metamorphoses due to the butterfly points closer to the real axis add 4 cusps to form a single 12-cusped loop. Four simultaneous beak-to-beak metamorphoses due to the four off-axis saddles then split off four 3-cusped loops, leaving a fifth 8-cusped caustic loop. Finally the outer pair of butterfly points causes two simultaneous butterfly metamorphoses that remove 4 cusps from the fifth loop, leading to the close limit with four 3-cusped loops and a single 4-cusped loop.

In Figure 2.5 we summarize the local behavior of the first three elementary caustic metamorphoses occurring in n -point-mass lenses (see e.g., 70; 59). The left, central, and right pairs of columns illustrate the beak-to-beak (vicinity of

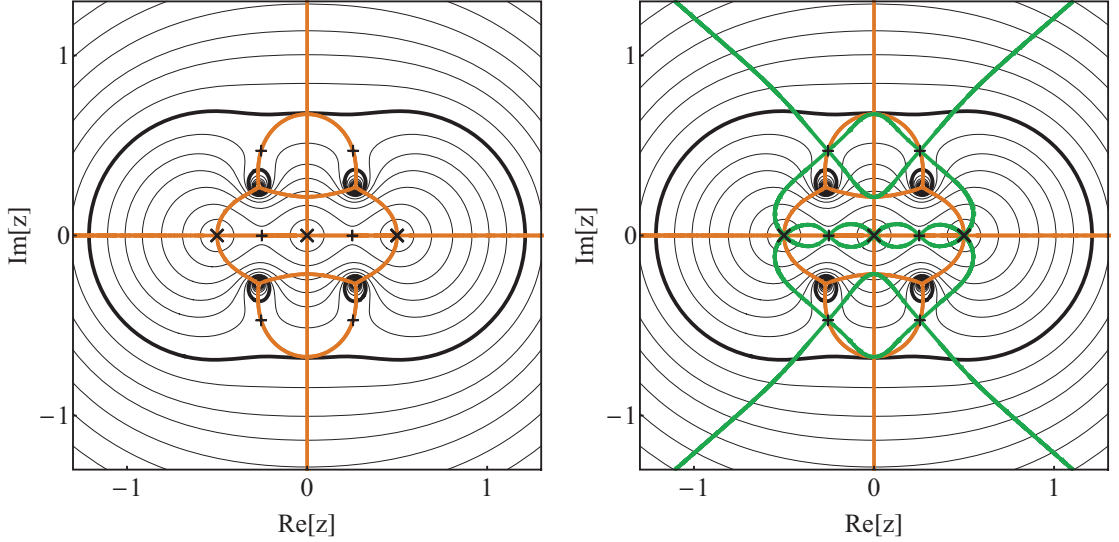


Figure 2.4 Butterfly metamorphosis in the image plane: cusp curve (orange) and morph curve (green) of an equal-mass triple lens with positions $\{z_1, z_2, z_3\} = \{-1, 0, 1\}s$, where $s = 0.5$. Jacobian contours are plotted outward from the lenses for $\det J \in \{-1599, -99, -16.6, -5.25, -2.06, -0.69, 0, 0.36, 0.578, 0.698, 0.788, 0.848, 0.891\}$. The two cusp-curve branches connecting the Jacobian maxima above the real axis and their mirror counterparts below the real axis each pass through a self-intersection point at which they are tangent to the contours. These points, found in the right panel as tangent intersections with the morph curve, correspond to butterfly metamorphoses. There are six additional beak-to-beak metamorphoses at saddle-point intersections. Notation as in Figure 2.1.

central saddle point from Figure 2.2), the swallow-tail (swallow-tail point close to top right maximum from Figure 2.3), and the butterfly (butterfly point just above central lens from Figure 2.4) metamorphoses, respectively. The left panel of each pair shows the detail in the image plane including Jacobian contours with constant $\det J$ spacing. The right panel shows the corresponding detail of the caustic in the source plane. Rows correspond to different lens scales parameterized by s , as marked in each pair (top: before metamorphosis, middle: at metamorphosis, bottom: after metamorphosis with two new cusps). The image-plane details are plotted in units of s , so that the three critical curves in each column correspond to three different contours from the same Jacobian contour plot.

In addition to the three types of local behavior shown in Figure 2.5, for a triple lens the only more complicated metamorphosis occurs at monkey saddles, where three loops of the critical curve meet. In the source plane they correspond to beak-to-beak metamorphoses with three “beaks” meeting at a single point. An example can be found in the companion paper (22).

In lenses with $n > 3$ components higher-order saddles may occur, corresponding to a meeting of a higher number of “beaks” in the source plane. In addition, higher-order metamorphoses may occur at cusp-curve self-intersections involving three or more cusp-curve branches. Their exploration, which may proceed in a similar manner as the butterfly analysis in § 2.5.5, is beyond the scope of this paper.

As a final caveat, note that all three scenarios illustrated in Figure 2.5 may

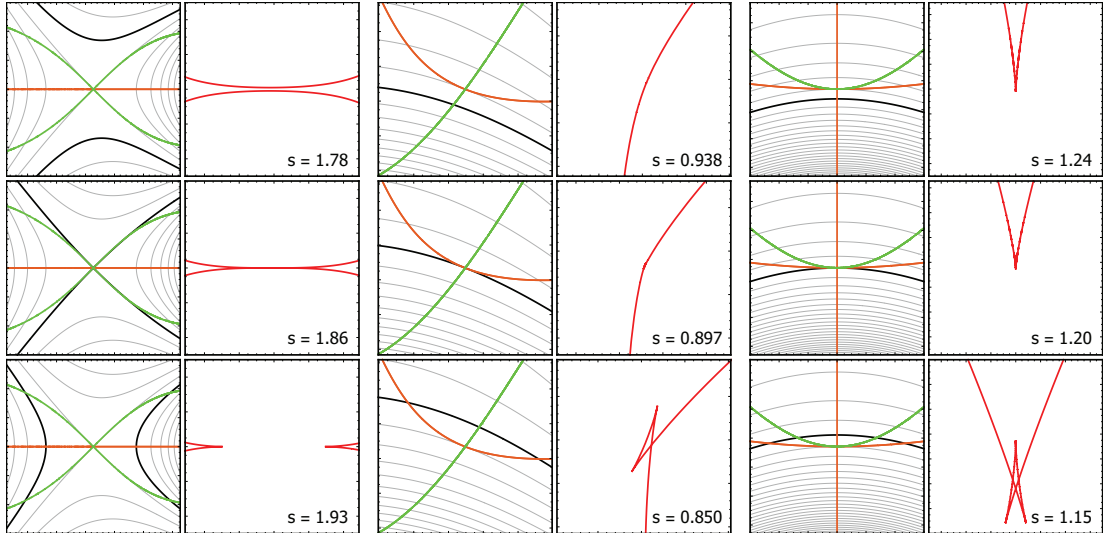


Figure 2.5 The first three elementary caustic metamorphoses of the n -point-mass lens. Left column: beak-to-beak (detail from Figure 2.2); central column: swallow-tail (detail from Figure 2.3); right column: butterfly metamorphosis (detail from Figure 2.4). Left panel in each pair: detail of image plane divided by scale parameter d (black: critical curve; gray: other Jacobian contours; orange: cusp curve; green: morph curve). Right panel in each pair: detail of source plane (red: caustic). Rows correspond to scale parameters d marked in the panels. Top: before metamorphosis with n cusps; middle: at metamorphosis; bottom: after metamorphosis with $n + 2$ cusps.

be complicated in special situations. The beak-to-beak scenario may be altered if the cusp curve crosses the saddle as a tangent to the critical curve. While this would have no effect on the change in critical-curve topology, the caustic may possibly undergo no change in cusp number. In the swallow-tail and butterfly scenarios there may be no change in cusp number if the critical and cusp curves have the same curvature at the tangent point. The outcome of these situations can be studied by expanding both curves around the metamorphosis point and checking whether the first order at which the curves differ is even or odd.

All caustic metamorphoses studied here were demonstrated by changing the lens scale, which permits the usage of contour plots to visualize the full sequence. However, the metamorphoses occur even when changing arbitrary other parameters of the lens. Nevertheless, they happen exactly at the points identified by the presented analysis. All relevant equations and the sequence of caustic changes remain the same for any crossing of the respective parameter-space boundary.

2.7 Summary

In this work we studied n -point-mass lensing by exploring the geometry of the Jacobian, viewed as a two-dimensional surface defined over the image plane. If we plot the Jacobian contours in the image plane, the zero-Jacobian contour represents the critical curve of the lens. However, as we show in § 2.3.3, any contour of the Jacobian $\det J(z) = \lambda$ corresponds to the critical curve of a lens with component spacing re-scaled by the factor $\sqrt[4]{1 - \lambda}$.

For a lens consisting of a given combination of point masses in a given formation, this property permits the simultaneous study of critical curves for all re-scaled configurations, from the single-lens close limit to the n -independent-lenses wide limit. A single contour plot thus illustrates the lens properties for a full 1-D cut through the parameter space of the lens, instead of just for a single parameter combination.

We extend the approach further in § 3.4 by introducing two scale-invariant curves: the cusp curve given by equation (2.34), and the morph curve given by equation (2.41). The cusp curve identifies the positions of cusp images along all the Jacobian contours. The morph curve pinpoints positions along the cusp curve, at which the number of cusps changes due to caustic metamorphoses.

For illustration, we present several simple applications in § 2.6. The overall structure of the curves for the binary lens shown in Figure 2.2 is generic, valid for any mass ratio. However, adding a third component already opens up a broader range of possible structures and associated lens properties. We use triple-lens examples to illustrate two additional caustic metamorphoses, the swallow tail in Figure 2.3 and the butterfly in Figure 2.4. Details of the image and source planes in Figure 2.5 demonstrate the characteristic features associated with these metamorphoses as well as the simple beak-to-beak metamorphosis.

In the companion paper (22) we use the presented approach for a systematic exploration of several simple triple-lens models. However, the concepts introduced here can be used also for more general studies. For example, a detailed analysis of the structure of critical, cusp, and morph curves would enable a full classification of local lensing behavior of triple, quadruple, etc. lenses. We conclude that image-plane analysis of Jacobian contour plots may prove to be a useful tool for studying and visualizing the nature of lensing by n -point-mass lenses.

We thank the anonymous referee for helpful suggestions. Work on this project was supported by Czech Science Foundation grant GACR P209-10-1318 and Charles University grant SVV-260089.

3. critical curves and caustics of triple-lens models¹

ABSTRACT

Among the 25 planetary systems detected up to now by gravitational microlensing, there are two cases of a star with two planets, and two cases of a binary star with a planet. Other, yet undetected types of triple lenses include triple stars or stars with a planet with a moon. The analysis and interpretation of such events is hindered by the lack of understanding of essential characteristics of triple lenses, such as their critical curves and caustics. We present here analytical and numerical methods for mapping the critical-curve topology and caustic cusp number in the parameter space of n -point-mass lenses. We apply the methods to the analysis of four symmetric triple-lens models, and obtain altogether 9 different critical-curve topologies and 32 caustic structures. While these results include various generic types, they represent just a subset of all possible triple-lens critical curves and caustics. Using the analyzed models, we demonstrate interesting features of triple lenses that do not occur in two-point-mass lenses. We show an example of a lens that cannot be described by the Chang-Refsdal model in the wide limit. In the close limit we demonstrate unusual structures of primary and secondary caustic loops, and explain the conditions for their occurrence. In the planetary limit we find that the presence of a planet may lead to a whole sequence of additional caustic metamorphoses. We show that a pair of planets may change the structure of the primary caustic even when placed far from their resonant position at the Einstein radius.

¹Accepted by The Astrophysical Journal (21).

3.1 Introduction

In the past two decades gravitational microlensing surveys have been very successful, in particular as a tool for studying the stellar population towards the Galactic bulge. A star passing close to the line of sight to a background “source” star is detected by its gravitational lens effect, which temporarily amplifies the flux from the source (e.g., 56). The main advantage of the method is its sensitivity to low-mass objects, ranging from stellar down to planetary masses, with most of them too faint to be routinely detected by other means.

In addition to single-star microlensing events, right from their start of operations the surveys have detected events with binary-star lenses (77; 3). The frequency of binary events is lower than the frequency of binary stars, since binaries with too close or too far components often mimic single-lens events. The microlensing sensitivity to low mass ratios finally led in 2003 to the first detection of microlensing by a star with a planet (11). By the time of writing, altogether 25 planetary systems had been detected by microlensing². A majority involved a star with a single planet; nevertheless, four of them involved three-body systems. In two cases the lens was a star with two planets (28; 39), while the other two involved a binary with a planet (31; 60). Other possible triple-lens systems that had not been detected yet include triple stars, or even lenses formed by a star with a planet with a moon.

Turning to the underlying physics, in the case of a single lens the light from the source star is split into two images, which remain generally unresolved due to their small angular separation $\lesssim 1$ mas. The accompanying temporary amplification of the flux from the source typically produces a simple symmetrically peaked light curve (e.g., 56). Lenses with multiple components produce a higher number of images and lead to a greater diversity of light curves, which peak anytime the source crosses or approaches the caustic of the lens. Any simple caustic crossing leads to the appearance or disappearance of a pair of unresolved images at positions defining the critical curve of the lens. The caustic and the critical curve thus are key characteristics of the lens. They depend sensitively on the lens parameters: the masses and positions of the components. Understanding the range of possible critical-curve and caustic geometries is a prerequisite for successful analysis and interpretation of observed microlensing light curves.

Microlensing by a two-component lens, such as a binary star or a star with a planet, is well described by the two-point-mass lens model. Such a lens has only two relevant parameters: the mass ratio, and the projected component separation. The model has been analyzed in detail by (71), (25), and (79); its limiting cases were studied by (23). For any mass ratio the critical curve was shown to have three different topologies. In order of decreasing component separation these are: “wide” with two separate loops, “intermediate” (or resonant) with a single loop, and “close” with an outer plus two inner loops. Each regime has a corresponding caustic geometry with the same number of separate non-overlapping loops: wide has two four-cusped loops, intermediate a single six-cusped loop, and close has one four-cusped plus two three-cusped loops. A source positioned outside the caustic has three images, while a source positioned inside the caustic has five images.

²<http://exoplanetarchive.ipac.caltech.edu>

Micro-lensing by triple lenses can be described analogously by the three-point-mass lens model. There are five lens parameters: two relative masses, and three relative positions defining the two-dimensional configuration of the components in the plane of the sky. In comparison with the two-point-mass lens, the model has a number of qualitative differences. For example, varying the lens parameters may lead to a change in the cusp number of the caustic without any accompanying change in the topology of the critical curve. Such changes in the caustic structure occur via swallow-tail or butterfly metamorphoses (70). In addition, loops of the caustic may overlap, and individual loops may self-intersect. As a result, the caustic may have inner multiply nested regions. All caustics separate the outer 4-image region from an inner 6-image region. Only caustics with overlapping loops or self-intersections have additional 8-image regions, in case of double nesting even 10-image regions.

However, unlike in the two-point-mass lens case, the full range of critical-curve topologies and caustic structures of the three-point-mass lens has not been explored yet. Such a study would require a systematic mapping of the five-dimensional parameter space, detecting changes in the critical curve and caustic of the corresponding lens. Nevertheless, a range of published works have explored different specific regimes of triple lenses. The first studies explored binary lenses with an additional external shear (32; 79), with caustics already displaying swallow tails and butterflies. Most numerous are the studies involving a stellar lens with two (or more) planets. Some of them demonstrate effects on the light curve, others for example place constraints on the presence of a second planet in observed single-planet events. Without claiming completeness, we refer here to the works of (27), (12), (33), (35), (62), (36), (46), (4), (69), (74), and (81).

Lensing by a binary star with a planet has been explored less frequently (6; 47; 37; 17). In view of the two recently detected systems, this is bound to change. The close and far limits of triple-star lensing were investigated by (13; 14). Finally, lensing by a star with a planet with a moon was studied by (34), (29), (38), and (48), with prospects for detecting such systems remaining open.

Here we set out to systematically study the critical curves and caustics of triple lenses. Based on the work of (25) and (79), we develop methods for efficient mapping of critical-curve topologies and caustic geometries in the parameter space of n -point-mass lenses. We then apply the methods to the analysis of simple triple-lens models. Initial steps of this research appeared in (18), (19), and (20).

We start in § 3.2 by introducing the basic concepts of n -point-mass lensing. In particular, we concentrate on the Jacobian and its properties, such as the equivalence of its contours with critical curves of re-scaled lens configurations (21). Analytical and numerical methods for mapping critical-curve topologies in the lens parameter space are introduced in § 3.3. In the next § 3.4 we discuss the caustic and its metamorphoses, and show how to track changes in cusp number using the cusp and morph curves (21). We apply the methods to triple lenses in § 3.5, starting with a brief overview of their properties in § 3.5.1. The following § 3.5.2 – § 3.5.5 include a full analysis of four symmetric two-parameter triple-lens models, with an overview of the found critical curves and caustics in § 3.5.6. We end by summarizing the main results and highlights in § 3.6.

3.2 The n -point-mass lens and its Jacobian

Galactic gravitational microlensing events can be described using a simple n -point-mass lens model, consisting of n components (stars, planets) in a single lens plane with no external shear and no convergence due to continuous matter. Following (78) we describe positions in the plane of the sky as points in the complex plane, with separations measured in units of the Einstein radius corresponding to the total mass of the lens.

The relation between the position of a background source ζ and the position z of its image formed by the lens is expressed by the lens equation

$$\zeta = z - \sum_{j=1}^n \frac{\mu_j}{\bar{z} - \bar{z}_j}, \quad (3.1)$$

where z_j and μ_j are the positions and fractional masses, respectively, of the individual components of the lens, and bars over variables denote their complex conjugation. The complex plane of the image positions z is called the image plane, and the complex plane of the source positions ζ is called the source plane. The fractional masses are normalized to the total mass of the lens, so that $\sum_{j=1}^n \mu_j = 1$.

The positions of individual components z_j generally change with time as they orbit around the center of mass of the lens. In this work we study the lensing properties of a “snapshot” n -body configuration at a given instant. A time-dependent microlensing event then corresponds to lensing by sequence of such snapshot configurations.

The n -point-mass lens with $n > 1$ components produces between $n + 1$ and $5(n - 1)$ images (in steps of two) of any point in the source plane (66; 45). In the image plane images appear and disappear in pairs along the critical curve of the lens. The critical curve can be expressed as the set of all points z_{cc} for which the sum

$$\sum_{j=1}^n \frac{\mu_j}{(z_{cc} - z_j)^2} = e^{-2i\phi}, \quad (3.2)$$

lies on the unit circle (78). Here ϕ is a phase parameter spanning the interval $\phi \in [0, \pi)$. In the source plane the image number changes when the source crosses the caustic ζ_c of the lens. The caustic is obtained by tracing critical-curve points back to the source plane using equation (3.1), i.e.,

$$\zeta_c = z_{cc} - \sum_{j=1}^n \frac{\mu_j}{\bar{z}_{cc} - \bar{z}_j}. \quad (3.3)$$

In mathematical terms, the critical curve is the set of points in the image plane with zero Jacobian of the lens equation. The Jacobian

$$\det J(z) = 1 - \left| \sum_{j=1}^n \frac{\mu_j}{(z - z_j)^2} \right|^2 \quad (3.4)$$

is discussed in detail in (21). Here we only summarize its properties important for the following analyses. As seen from equation (3.4), the Jacobian is a real function defined over the complex plane, running from $-\infty$ at the positions of all

components $z = z_j$ to 1 at complex infinity and at the positions of all Jacobian maxima. These can be found as the roots of the polynomial obtained from

$$\sum_{j=1}^n \frac{\mu_j}{(z - z_j)^2} = 0. \quad (3.5)$$

The degree of the corresponding polynomial indicates the Jacobian has up to $2n - 2$ different maxima. The number may be lower if there are any degenerate roots; these correspond to higher-order maxima. A doubly degenerate root corresponds to a double maximum, a root with degeneracy 3 corresponds to a triple maximum, etc.

The saddle points of the Jacobian can be found similarly among the roots of the polynomial obtained from

$$\sum_{j=1}^n \frac{\mu_j}{(z - z_j)^3} = 0. \quad (3.6)$$

The corresponding polynomial has up to $3n - 3$ different roots. First we need to sort out any common roots of equations (3.5) and (3.6), those correspond to higher-order maxima instead of saddles. All remaining roots are Jacobian saddle points. The number of different saddles may be reduced further if there are any degenerate roots; these identify higher-order saddles. A non-degenerate root corresponds to a simple saddle, a doubly degenerate root corresponds to a monkey saddle, etc.

Studying the contours of the Jacobian, (21) pointed out a remarkable correspondence. While the zero-Jacobian contour is the critical curve z_{cc} of the lens, any other Jacobian contour z_λ with $\det J(z_\lambda) = \lambda$ is a re-scaled critical curve of a lens with the same components in re-scaled positions. Denoting by $z_{cc}(\mu_j, z_j)$ and $z_\lambda(\mu_j, z_j)$ the critical curve and $\det J = \lambda$ contour, respectively, of a lens with masses μ_j and positions z_j , we can express this correspondence by

$$z_\lambda(\mu_j, z_j) = z_{cc}(\mu_j, z_j \sqrt[4]{1 - \lambda}) / \sqrt[4]{1 - \lambda}. \quad (3.7)$$

For $\lambda = 0$ we get the critical curve of the original configuration. Close to the original positions, the $\lambda \rightarrow -\infty$ contours are shrunk versions of the wide-limit critical curves. At the other limit, the highest-Jacobian $\lambda \rightarrow 1$ contours are expanded versions of the close-limit critical curves. A single Jacobian contour plot thus yields the critical curves for all scalings of the given lens configuration, from the close to the wide limit.

3.3 Critical-curve topology regions in parameter space and their boundaries

3.3.1 Critical-curve topology and its changes

Here we summarize general properties of n -point-mass lens critical curves following (21). Varying the phase parameter ϕ in the critical curve equation (3.2), we obtain $2n$ continuous line segments, which may connect to form $1 \leq N_{loops} \leq 2n$

closed loops³ of the critical curve (78). Individual loops may lie in separate regions of the image plane, or they may lie nested inside other loops. The total number and mutual position of loops define the topology of the critical curve.

In the wide limit, all lenses have a critical curve with $N_{loops} = n$ separate loops, corresponding to n Einstein rings of the individual components. In the close limit, the critical curve has $N_{loops} = 1 + N_{max}$ loops, where N_{max} is the number of different Jacobian maxima. One loop corresponds to the Einstein ring of the total mass, plus there is a small loop around each maximum of the Jacobian. In view of the discussion following equation (3.5), $N_{max} \leq 2n - 2$, so that in the close limit $N_{loops} \leq 2n - 1$. The equality holds if the Jacobian has only non-degenerate (simple) maxima. Any degenerate (higher-order) maximum reduces the number of loops. For example, the two-point-mass lens always has two different maxima, thus its critical curve always has 3 loops in the close limit.

When varying the parameters of the lens such as its scale, the topology may undergo changes when individual loops merge or split. This occurs at Jacobian saddle points when the critical curve passes through them (e.g., 25). Two loops come into contact at a simple saddle, three at a monkey saddle, more loops at gradually higher-order saddles. As shown by equation (3.6), the Jacobian may have up to $3n - 3$ different saddle points, with the highest number occurring when there are no higher-order saddles and no higher-order maxima. The number of different Jacobian contours passing through the set of saddles identifies the total number of changes in critical-curve topology encountered when varying the scale of the lens from the wide to the close limit. This can be seen as a consequence of the Jacobian-contour / critical-curve correspondence expressed by equation (3.7). Therefore, the critical curve of an n -point-mass lens may undergo no more than $3n - 3$ changes in topology between the wide and close limits.

In the case of the two-point-mass lens, there are always three simple saddles. One lies on the axis between the components, while an off-axis pair of saddles lies on a different Jacobian contour. The two distinct saddle contours imply that the two-point-mass lens critical curve always undergoes two changes when varying the component separation s , and thus has exactly three topologies. The wide topology has two separate loops, the intermediate topology has a single merged loop, and the close topology has an outer loop plus two small inner loops around the Jacobian maxima. The topology sequence is independent of the second lens parameter, the mass ratio of the lens components.

Proceeding to lenses with more than two components, we note that the shape of the critical curve depends on $3n - 4$ lens parameters (e.g., 21). Following the preceding discussion, boundaries between regions in parameter space with different critical-curve topology can be found by identifying parameter combinations, for which the critical curve passes through a saddle point of the Jacobian (e.g., 25). The search for these boundaries is thus mathematically reduced to finding the conditions for the occurrence of a common solution of equations (3.2) and (3.6).

The usual analytical approach described in the following § 3.3.2 is based on rewriting both equations in polynomial form and computing their resultant. This step is then followed by a second resultant constructed from the first. However,

³We note that at least for $n < 3$ the sharp upper bound is $2n - 1$, and even for triple lenses we have found no more than 5 loops so far.

this approach often yields unwieldy expressions. In addition, one has to check the results for spurious solutions. These do not occur in the two-point-mass lens, but they do appear in all the triple-lens models studied further below.

As an alternative, we present in § 3.3.3 and § 3.3.4 two efficient numerical methods for mapping the boundaries. These can be used in models with at least one scale-defining parameter, such as the component separation s in the two-point-mass lens. In the first method we find the roots of the first resultant condition, while in the second we utilize the Jacobian scaling properties described by (21). Both methods are free of spurious solutions.

3.3.2 Analytical boundaries computed by resultant method

The method described here was pioneered in the context of critical-curve topology mapping by (25) and (79). Multiplying the saddle-point equation (3.6) by the product of its denominators yields

$$p_{sadd}(z) = \sum_{j=1}^n \mu_j \prod_{k=1, k \neq j}^n (z - z_k)^3 = 0, \quad (3.8)$$

a polynomial of degree $3n - 3$. In a similar manner we convert the critical-curve equation (3.2) to

$$p_{crit}(z) = \prod_{k=1}^n (z - z_k)^2 - e^{2i\phi} \sum_{j=1}^n \mu_j \prod_{k=1, k \neq j}^n (z - z_k)^2 = 0, \quad (3.9)$$

a polynomial of degree $2n$ for any value of the parameter ϕ . The analytical condition for the existence of a common root of $p_{sadd}(z)$ and $p_{crit}(z)$ is

$$\text{Res}_z(p_{sadd}, p_{crit}) = 0, \quad (3.10)$$

where the resultant $\text{Res}_z(f, g)$ of two polynomials f, g is a function of their coefficients. It may be computed by evaluating the determinant of the Sylvester or Bézout matrices, as described in Appendix A.

The expression obtained from equation (3.10) is a polynomial in terms of $e^{2i\phi}$. If we denote $w = e^{2i\phi}$, we can write the result as

$$p_{res}(w) = \sum_{j=0}^m a_j w^j = 0, \quad (3.11)$$

where the degree of the polynomial $m \leq 3n - 3$. The boundary condition is now equivalent to the condition for p_{res} to have a root on the unit circle.

In order to obtain the condition purely in terms of the lens parameters, (79) suggested the following approach for the two-point-mass lens. For a root along the unit circle $\bar{w}^j = w^{-j}$, so that if we take the complex conjugate of equation (3.11) and multiply it by w^m , we get another polynomial equation

$$p_{conj}(w) = \sum_{j=0}^m \bar{a}_{m-j} w^j = 0. \quad (3.12)$$

Along the boundary in parameter space, polynomials p_{res} and p_{conj} must have a common root, thus

$$\text{Res}_w(p_{res}, p_{conj}) = 0 \quad (3.13)$$

yields the sought condition in terms of lens parameters. We point out that equation (3.13) presents a single constraint in parameter space. Hence for two-parameter models (such as the two-point-mass lens or the triple-lens models described in § 3.5.2 – § 3.5.5) it generally describes a set of curves, for three-parameter models a set of surfaces, etc.

We illustrate the approach here on the case of the two-point-mass lens (25; 79), parameterized by the fractional mass of one component $\mu \in (0, 1)$ and the separation between the components $s > 0$. If we align the lens with the real axis and place the components symmetrically about the origin, their positions and masses are $\{z_1, z_2\} = \{-s/2, s/2\}$, and $\{\mu_1, \mu_2\} = \{\mu, 1 - \mu\}$. The polynomial equations for p_{sadd} and p_{crit} are

$$p_{sadd}(z) = z^3 + \frac{3}{2}s(1 - 2\mu)z^2 + \frac{3}{4}s^2z + \frac{1}{8}s^3(1 - 2\mu) = 0 \quad (3.14)$$

and

$$p_{crit}(z) = z^4 - \frac{1}{2}(s^2 + e^{2i\phi})z^2 - s(1 - 2\mu)e^{2i\phi}z + \frac{1}{16}s^2(s^2 - 4e^{2i\phi}) = 0. \quad (3.15)$$

Using them in equation (3.10) leads to

$$\begin{aligned} \text{Res}_z(p_{sadd}, p_{crit}) = & -s^6\mu^2(1 - \mu)^2[e^{6i\phi} - 3s^2(1 - 9\mu + 9\mu^2)e^{4i\phi} \\ & + 3s^4e^{2i\phi} - s^6] = 0. \end{aligned} \quad (3.16)$$

The factors in front of the square brackets are non-zero for any genuine two-point-mass lens. If we set $e^{2i\phi} = w$, the term in the brackets yields the polynomial equation

$$p_{res}(w) = w^3 - 3s^2(1 - 9\mu + 9\mu^2)w^2 + 3s^4w - s^6 = 0. \quad (3.17)$$

Following equation (3.12) we construct

$$p_{conj}(w) = -s^6w^3 + 3s^4w^2 - 3s^2(1 - 9\mu + 9\mu^2)w + 1 = 0. \quad (3.18)$$

The resultant obtained from equation (3.13) can be factorized as follows:

$$\begin{aligned} & [1 - 3s^2(1 - 9\mu + 9\mu^2) + 3s^4 - s^6][1 + 3s^2(1 - 9\mu + 9\mu^2) + 3s^4 + s^6] \\ & \times [1 - 3s^4 + 3s^8(1 - 9\mu + 9\mu^2) - s^{12}]^2 = 0. \end{aligned} \quad (3.19)$$

At least one of these three square brackets thus has to be equal to zero.

The first bracket in equation (3.19) is equal to $p_{res}(1)$, with $w = 1$ corresponding to $\phi = 0$. Therefore, it must include any transitions occurring on the critical curve along the real axis, in this case the passage of the critical curve through the central saddle point. Taken as a polynomial in s , the first bracket has a single real positive root (25)

$$s_w = \left[\sqrt[3]{\mu} + \sqrt[3]{1 - \mu} \right]^{3/2}, \quad (3.20)$$

which is the boundary between the wide and intermediate topologies.

The second bracket is equal to $-p_{res}(-1)$, with $w = -1$ corresponding to $\phi = \pi/2$. There is only a single zero point of this expression in parameter space, $[\mu, s] = [0.5, \sqrt{0.5}]$, which corresponds to the intermediate – close splitting along the imaginary axis of the critical curve of an equal-mass lens.

The third bracket corresponds to topology transitions that occur at any other values of ϕ on the critical curve. Here they describe the passage of the critical curve through the pair of saddle points off the real axis. Taken as a polynomial in s , the third bracket has a single real positive root (25; 67)

$$s_c = \left[\sqrt[3]{\mu} + \sqrt[3]{1 - \mu} \right]^{-3/4} = s_w^{-1/2}, \quad (3.21)$$

which is the boundary between the intermediate and close topologies. This boundary in fact passes through the single zero point of the second bracket in equation (3.19) at $\mu = 0.5$ as well. The two curves given by equations (3.20) and (3.21) thus fully describe the division of the two-point-mass lens parameter space according to critical-curve topology.

Applying the same procedure to two-parameter models of triple lenses leads to the following problem. The method yields not only all the sought boundaries, but also curves corresponding to no change in critical-curve topology. These spurious results are additional solutions of equation (3.13), which correspond to common roots of $p_{res}(w)$ and $p_{conj}(w)$ lying off the unit circle. In Appendix B we describe how this occurs and why it doesn't occur in the two-point-mass lens. All curves corresponding to specific values of w that can be factored out of the final equation (3.13), such as $p_{res}(1)$ and $p_{res}(-1)$ in the case of equation (3.19), are genuine boundaries. Parameters satisfying the remaining parts of equation (3.13) should be verified either by computing sample critical curves, or by confirming the existence of a root of $p_{res}(w)$ on the unit circle.

Alternatively, instead of computing the second resultant, one may solve the polynomial from equation (3.11) directly by re-substituting $w = \cos 2\phi + i \sin 2\phi$. By taking the real and imaginary parts of p_{res} separately, equation (3.11) may be treated as a set of two real equations. In case all the coefficients a_j are real, such as in the two-point-mass lens or all the triple-lens models described in § 3.5.2 – § 3.5.5, the imaginary part of equation (3.11) instantly yields the $\phi = 0$ and $\phi = \pi/2$ solutions. The corresponding real parts then yield the $p_{res}(1) = 0$ and $p_{res}(-1) = 0$ boundaries, respectively. The other boundaries can be found by substituting $\cos 2\phi = \xi$ and solving the two obtained real polynomial equations in ξ . Finding all roots $\xi_0 \in [-1, 1]$ of one of the polynomials and substituting them into the other polynomial yields the remaining boundary conditions.

3.3.3 Numerical boundaries computed using first resultant

For any particular n -point-mass lens model the lens masses μ_j and positions z_j depend on a given set of parameters. Mapping the boundaries in parameter space numerically can be a tedious task. If we can compute analytically at least the first resultant and the polynomial p_{res} given by equation (3.11), the task is reduced to keeping track of the roots of p_{res} as one scans through parameter space. Positions at which the absolute value of any of the roots crosses unity correspond to points on the boundary. However, even this can be a very time-consuming exercise.

In case at least one of the parameters of the lens model defines an angular scale in the plane of the sky (such as the separation s in the two-point-mass lens), it is possible to reduce the dimension of the space to be scanned by one. At the same time this approach directly yields all boundary points for each reduced parameter combination. In case there are several angular-scale parameters, we select one of them (further denoted by s) and instead of the others we use their ratio to s . We can now assume that all masses are independent of s and all lens positions are directly proportional to s . All the models discussed in this paper satisfy these requirements.

If we divide equation (3.8) by s^{3n-3} , we obtain a polynomial equation of exactly the same form with $z' = z/s$ and re-scaled lens positions $z'_k = z_k/s$,

$$p'_{sadd}(z') = s^{-3n+3} \sum_{j=1}^n \mu_j \prod_{k=1, k \neq j}^n (z's - z'_k s)^3 = \sum_{j=1}^n \mu_j \prod_{k=1, k \neq j}^n (z' - z'_k)^3 = 0. \quad (3.22)$$

The equation is thus explicitly independent of s . If we divide similarly equation (3.9) by s^{2n} we obtain

$$p'_{crit}(z') = \prod_{k=1}^n (z' - z'_k)^2 - e^{2i\phi} s^{-2} \sum_{j=1}^n \mu_j \prod_{k=1, k \neq j}^n (z' - z'_k)^2 = 0, \quad (3.23)$$

a polynomial of exactly the same form as $p_{crit}(z)$ but with $e^{2i\phi} s^{-2}$ instead of $e^{2i\phi}$. Setting the resultant of $p'_{sadd}(z')$ and $p'_{crit}(z')$ equal to zero, we obtain a polynomial in terms of $w' = e^{2i\phi} s^{-2}$,

$$p'_{res}(w') = \sum_{j=0}^m a'_j w'^j = 0, \quad (3.24)$$

in which all coefficients a'_j are independent of s , and the degree of the polynomial $m \leq 3n-3$. Finding the boundaries now requires a scan of the reduced parameter space (skipping s), with the boundaries directly given by all roots of $p'_{res}(w')$. Any such root w'_{root} yields the value of s at the boundary, $s = |w'_{root}|^{-1/2}$. At the same time it also yields the position along the critical curve, $\phi = \arg(w'_{root})/2$, at which the critical curve splits.

Furthermore, if all coefficients a'_j are real (such as in all the models discussed in this paper), all roots of $p'_{res}(w')$ either are real or they occur in complex-conjugate pairs. A complex-conjugate pair of roots yields the same boundary value of s , corresponding to a simultaneous split at complex-conjugate positions along the critical curve. It is thus useful to keep track of the discriminant of $p'_{res}(w')$ in the reduced parameter space. Its change of sign corresponds to a transition from a pair of real roots (two boundaries) to a pair of complex-conjugate roots (one boundary). Zero discriminant corresponds to a multiple root of $p'_{res}(w')$, describing a single boundary point and a single ϕ value along the critical curve.

For illustration, for the two-point-mass lens we obtain

$$p'_{res}(w') = w'^3 - 3(1 - 9\mu + 9\mu^2)w'^2 + 3w' - 1 = 0, \quad (3.25)$$

and its discriminant

$$\Delta(p'_{res}) = -3^9 \mu^2 (1 - \mu)^2 (1 - 2\mu)^2 \leq 0. \quad (3.26)$$

The only non-degenerate configuration with zero discriminant has $\mu = 1/2$, for which there is a double real root plus another real root: $w'_{root} = \{-2, -2, 1/4\}$. These correspond to boundary points $s = \{\sqrt{1/2}, \sqrt{1/2}, 2\}$. For all other $\mu \in (0, 1)$ the discriminant is negative. Thus, $p'_{res}(w')$ has one real root and a complex-conjugate pair of roots, resulting in two boundary values of s for any μ .

3.3.4 Numerical boundaries computed using Jacobian-contour correspondence

We return here to the method mentioned briefly in § 3.3.1. Instead of computing the resultant, we can map the boundaries in parameter space utilizing the correspondence between Jacobian contours and critical curves of re-scaled lens configurations (21), described here at the end of § 2.2. Just like in the previous case, even this method requires having a single angular-scale defining parameter s , with all lens positions directly proportional to it, and all masses independent of it.

For a given set of the remaining parameters plus an arbitrary non-zero scale parameter s_0 we compute the positions of the Jacobian saddle points z_{sadd} by finding all roots of $p_{sadd}(z)$ from equation (3.8). For each root we evaluate $\det J(z_{sadd})$ from equation (3.4), which identifies the contour passing through the saddle point. Now the Jacobian-contour / critical-curve correspondence tells us, that in order for the critical curve to pass through the saddle point, we need to re-scale the lens positions by $\sqrt[4]{1 - \det J(z_{sadd})}$, as shown in equation (3.7). Hence, the boundary value of the parameter s is $s_0 \sqrt[4]{1 - \det J(z_{sadd})}$. Recalling the polynomial degree of $p_{sadd}(z)$, this approach yields up to $3n - 3$ different boundaries for any given point of the reduced parameter space.

For illustration we refer to Figure 1 from (21), which shows a Jacobian contour plot of a binary lens with $\mu = 0.8$ and $s_0 = 1$. The real saddle point lies on the $\det J \approx -11.0$ contour, and the complex-conjugate saddle-point pair lies on the $\det J \approx 0.711$ contour. The corresponding boundary separations are thus $s = \sqrt[4]{1 + 11} \approx 1.861$ and $s = \sqrt[4]{1 - 0.711} \approx 0.733$, respectively.

3.4 Mapping the number of cusps of the caustic in parameter space

The caustic of the lens, defined here by equation (3.3), consists of the same number of closed loops as the critical curve. We refer to (21) for an overall discussion of the properties of the n -point-mass lens caustic and its cusps. Here we are interested in tracking changes in the number of cusps in the parameter space of the lens.

Since individual loops or parts of the caustic may overlap in lenses with three or more components, we specify that we count the number of cusps encountered as we trace along each loop of the caustic. This means that a cusp superimposed over a fold is still a cusp, or that two or more cusps along different parts of the caustic that happen to lie at the same position in the source plane are still counted as two or more cusps.

The cusp number changes in caustic metamorphoses. The simplest of them is the beak-to-beak metamorphosis, in which two tangent folds reconnect and form two facing cusps (see Figure 5 in 21). In the image plane this always corresponds to a change in critical-curve topology at a saddle point. The corresponding boundaries in parameter space are thus identical with those studied in § 3.3.

While the beak-to-beak metamorphosis occurs already in two-point-mass lenses, two additional types occur in triple lenses: the swallow-tail and butterfly metamorphoses. They are discussed in more detail and illustrated in (21). Both occur on the caustic without any change in topology or other significant effect on the critical curve. The lens-parameter conditions for the occurrence of these additional metamorphoses form new boundaries in parameter space, which subdivide the critical-curve topology regions discussed in § 3.3.

For the following analysis we will use the cusp curve and morph curve introduced by (21). The parametric form of the cusp curve is

$$\left[\sum_{j=1}^n \frac{\mu_j}{(z - z_j)^3} \right]^2 = \Lambda \left[\sum_{j=1}^n \frac{\mu_j}{(z - z_j)^2} \right]^3, \quad (3.27)$$

where $\Lambda \geq 0$ is a real parameter. The intersections of the cusp curve with the critical curve in the image plane identify the positions of cusp images along the critical curve. Since the curve is scale-invariant, its intersections with other Jacobian contours identify the positions of cusp images for all arbitrarily shrunk or expanded lens configurations.

Another scale-invariant curve in the image plane is the morph curve, defined in parametric form by

$$\left[\sum_{j=1}^n \frac{\mu_j}{(z - z_j)^2} \right] \left[\sum_{j=1}^n \frac{\mu_j}{(z - z_j)^4} \right] = (1 + i\Gamma) \left[\sum_{j=1}^n \frac{\mu_j}{(z - z_j)^3} \right]^2, \quad (3.28)$$

where Γ is a real parameter. Its intersections with the cusp curve away from the lens positions and higher-order maxima identify the positions of metamorphosis-point images. Intersections at saddles correspond to beak-to-beaks, simple intersections away from special points correspond to swallow tails, and intersections at two-branch self-intersection points of the cusp-curve correspond to butterflies if the critical curve is tangent to either of the branches (21).

In order to find conditions for the occurrence of swallow-tail and butterfly metamorphoses, we first locate all intersections of the cusp curve and morph curve, and leave out the lens positions, saddle points, and higher-order maxima. We use the parametric polynomial forms of the curves obtained by multiplying equations (3.27) and (3.28) by all their denominators. We then employ a method analogous to the one used in § 3.3.2 for finding the topology boundaries in parameter space. We compute the resultant of the two polynomials and express the result as a polynomial in the morph-curve parameter Γ . Since we seek solutions with Γ real, we compute a second resultant of the obtained polynomial with its complex conjugate.

The result can be factorized to obtain several conditions involving the non-scaling parameters of the lens, each as a polynomial in the cusp-curve parameter Λ . For any combination of the non-scaling parameters we look for real non-negative roots Λ . Equation (3.27) then yields a set of z 's on the cusp curve:

those that satisfy equation (3.28) and lie on the morph curve are the sought intersections. The final check is important, since the second resultant condition may introduce additional spurious solutions. In case the second resultant cannot be simply factorized or generally is too unwieldy, one can find the intersections numerically by gradually varying Λ and tracing the branches of the cusp curve, checking each point z with the morph-curve equation (3.28).

We then compute the Jacobian at the metamorphosis points to identify the critical curve passing through each of them. The corresponding scaling factor $\sqrt[4]{1 - \det J}$ determines the separation of the lens components, just like in the saddle-point case in § 3.3.4. The obtained parameter combinations form additional curves in parameter space, leading to its final division into subregions with different combinations of cusps on the loops of the caustic.

3.5 Triple-lens models

3.5.1 General properties

The general triple lens is described by five parameters: typically two relative masses and three spatial-configuration-defining parameters. Among these three it is advantageous to select a single scale parameter, such as the separation of two of the components, or the perimeter of the triangle connecting the components. The remaining two parameters can be for example angles or relative lengths. With such a choice one may utilize the methods from § 3.3 and § 3.4 for studying critical curves and caustics based on the scaling properties of the Jacobian.

The Jacobian surface has three poles at the lens positions, hence the critical curve has three loops in the wide limit. There are up to four different Jacobian maxima, therefore in the close limit the critical curve has up to five loops: an Einstein ring corresponding to the total mass, plus up to four small loops around the maxima. The surface has up to six different saddle points. As a consequence, the critical curve of any triple-lens configuration may undergo up to six topology changes when varying the scale parameter from the close to the wide limit.

The critical-curve polynomial $p_{crit}(z)$ from equation (3.9) is of sixth degree, implying that the critical curve and caustic may each have no more than six loops. We point out here in advance that the models discussed further in § 3.5.2 – § 3.5.5 have only up to five loops.

A compact expression for $p_{crit}(z)$ can be obtained in terms of symmetric moments of the lens configuration. In general, five such moments are sufficient:

$$c_j = \frac{1}{j} \sum_{k=1}^3 z_k^j \quad (3.29)$$

for $j = 1 \dots 3$, and the mass-weighted

$$d_j = \sum_{k=1}^3 \mu_k z_k^j \quad (3.30)$$

for $j = 1, 2$. With these definitions d_1 is the center of mass of the lens, and $c_1/3$ is its geometric center. In equal-mass models ($\mu_k = 1/3$) the two centers coincide, so that $d_1 = c_1/3$, and $d_2 = 2 c_2/3$.

If we set the origin of the complex plane at the geometric center ($c_1 = 0$), we arrive at a simpler form of equation (3.9) than if we used the center of mass. The critical-curve polynomial equation can then be written using the four other complex moments:

$$p_{crit}(z) = z^6 - (2c_2 + e^{2i\phi})z^4 - 2(c_3 + d_1e^{2i\phi})z^3 + [c_2^2 + (2c_2 - 3d_2)e^{2i\phi}]z^2 + 2c_3(c_2 - e^{2i\phi})z + c_3^2 - (c_2^2 + c_3d_1 - c_2d_2)e^{2i\phi} = 0. \quad (3.31)$$

In a similar manner we may re-write the Jacobian saddle-point polynomial equation (3.8) in terms of the same four moments:

$$p_{sadd}(z) = z^6 + 3d_1z^5 - 3(c_2 - 2d_2)z^4 + (7c_3 + c_2d_1)z^3 + 3(c_2^2 + 2c_3d_1 - c_2d_2)z^2 - 3c_3(c_2 - d_2)z - c_2^2(c_2 - d_2) + c_3(c_3 - c_2d_1) = 0. \quad (3.32)$$

For any specific triple-lens model it is sufficient to express the moments in terms of the model parameters and use them in equations (3.31) and (3.32). The transitions between different critical-curve topologies can then be mapped using the methods described in § 3.3.2 – § 3.3.4.

In the following § 3.5.2 – § 3.5.5 we illustrate the nature of triple lenses by performing the analysis described in § 3.3 and § 3.4 on four simple two-parameter models. We chose the most symmetric models with a single scale parameter, sketched in Figure 3.1. Two of the models are linear (symmetric with variable central mass, general asymmetric with equal masses), and two are triangular (equilateral with variable mass in one vertex, isosceles with variable vertex angle and equal masses). Each of the models, seen as 2D cuts through the full 5D triple-lens parameter space, intersects at least one other model. For example, the isosceles model includes equal-mass equilateral and equal-mass symmetric linear configurations. As a combination, these models form a reference set for further studies of the triple lens.

For all the models we present parameter-space maps of critical-curve topologies and cusp numbers, together with galleries of all different topologies. In the accompanying text we pay particular attention to interpreting the wealth of information contained in the figures. We point out any particularly interesting features of the critical curves and caustics. For better orientation, the text for each model is structured under the following headings: Model Description, Jacobian Surface Character, Topology Boundaries, Critical-curve Topologies, Caustic Structure, Jacobian Contour Plots, Planetary Limits, Close Limit, and Wide Limit. For the first model, the linear symmetric configuration in § 3.5.2, we additionally include the equations of the topology boundaries obtained from the resultant method, a gallery of all transition topologies with merging critical-curve loops, the polynomial expressions for the cusp and morph curves, and a gallery of caustics from all subregions of the parameter space subdivided by swallow-tail and butterfly boundaries.

In § 3.5.6 we give a combined overview of all critical-curve topologies and caustic structures occurring in the studied triple-lens models.

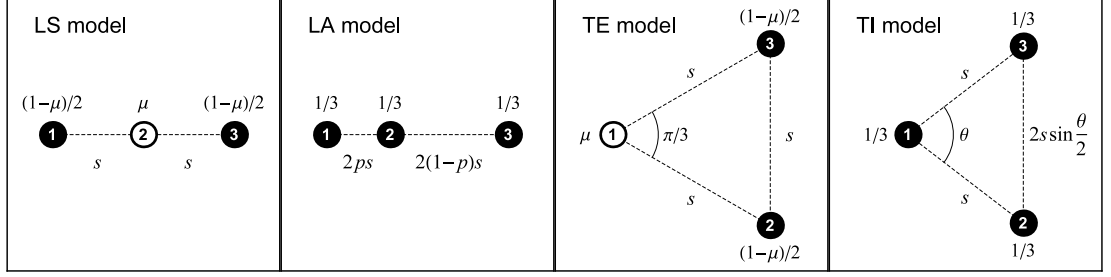


Figure 3.1 Configurations of the analyzed triple-lens models. Lens components are marked by numbered circles and labelled by their masses; black circles indicate equal mass. Model parameters: Linear Symmetric – central mass μ , separation s of neighbors; Linear Asymmetric – relative position p of central component, half-separation s of outer components; Triangular Equilateral – mass μ of component 1, side length s ; Triangular Isosceles – vertex angle θ , leg length s .

3.5.2 LS Model: Linear Symmetric Configuration

Model Description — In the LS model, sketched in the first panel of Figure 3.1, the three lens components lie equidistantly along a line, spaced by separation s . The second parameter is the fractional mass μ of the central component. Placing the origin at the geometric center and the lenses along the real axis, the positions and masses of the components are $\{z_1, z_2, z_3\} = \{-s, 0, s\}$ and $\{\mu_1, \mu_2, \mu_3\} = \{(1 - \mu)/2, \mu, (1 - \mu)/2\}$, with parameter ranges $\mu \in (0, 1)$ and $s \in (0, \infty)$.

The $\mu = 0$ limit describes an equal-mass binary with components 1 & 3 separated by $2s$. The $\mu = 1$ case corresponds to a single central lens represented by component 2. The three-equal-masses case with $\mu = 1/3$ is identical with special cases of two other models discussed further below: the $p = 1/2$ configurations of the LA model in § 3.5.3, and the $\theta = \pi$ configurations of the TI model in § 3.5.5. *Jacobian Surface Character* — For $\mu \neq 1/9, 1/5$: four simple maxima + six simple saddles; for $\mu = 1/9$: two double maxima + four simple saddles; for $\mu = 1/5$: four simple maxima + two simple saddles + two monkey saddles.

For $\mu \leq 1/9$ all maxima lie in complex-conjugate pairs along the imaginary axis; for $\mu > 1/9$ there are two complex-conjugate pairs of simple maxima symmetrically displaced from the imaginary axis.

Two simple saddles lie along the real axis between neighboring lens components. The remaining saddles for $\mu \leq 1/5$ lie in complex-conjugate pairs along the imaginary axis; for $\mu > 1/5$ they lie in complex-conjugate pairs symmetrically displaced from the imaginary axis.

Topology Boundaries — Due to the high degree of symmetry of the LS model, two of the moments defined by equations (3.29) and (3.30) are zero, $c_3 = d_1 = 0$. This leaves only two non-zero moments, $c_2 = s^2$ and $d_2 = (1 - \mu) s^2$. The critical-curve polynomial is reduced to

$$p_{crit}(z) = z^6 - (2s^2 + e^{2i\phi})z^4 + [s^2 + (3\mu - 1)e^{2i\phi}]s^2z^2 - \mu s^4 e^{2i\phi} = 0, \quad (3.33)$$

and the saddle-point polynomial to

$$p_{sadd}(z) = z^6 + 3(1 - 2\mu)s^2z^4 + 3\mu s^4z^2 - \mu s^6 = 0, \quad (3.34)$$

both in the form of cubic polynomials in z^2 . Hence they can be solved analytically, yielding bulky explicit formulae for the critical curve and Jacobian saddle points. We proceed to identify the boundaries of parameter-space regions with different critical-curve topologies using the resultant method described in § 3.3.2, applied here to the two cubic polynomials.

The first resultant yields the polynomial equation

$$p_{res}(w) = (1 - 9\mu) w^3 + 6(1 - 15\mu + 18\mu^2) s^2 w^2 - 3(5 + 3\mu) s^4 w + 8 s^6 = 0, \quad (3.35)$$

where $w = e^{2i\phi}$. The second resultant can be factorized to yield three independent conditions,

$$8 s^6 - 3(5 + 3\mu) s^4 + 6(1 - 15\mu + 18\mu^2) s^2 + 1 - 9\mu = 0 \quad (3.36)$$

$$8 s^6 + 3(5 + 3\mu) s^4 + 6(1 - 15\mu + 18\mu^2) s^2 - 1 + 9\mu = 0 \quad (3.37)$$

$$64 s^{12} - 48(1 - 15\mu + 18\mu^2) s^8 - 3(5 + 3\mu)(1 - 9\mu) s^4 - (1 - 9\mu)^2 = 0 \quad (3.38)$$

each defining a curve in parameter space. The left-hand side of equation (3.36) is equal to $p_{res}(1)$, hence it describes the splitting of the critical curve at $\phi = 0$. Similarly, the left-hand side of equation (3.37) is equal to $p_{res}(-1)$, hence it describes the splitting of the critical curve at $\phi = \pi/2$. These parameter-space curves thus are genuine boundaries between regions with different critical-curve topology. Due to the form of equation (3.33) any splitting points of the critical curve along the real or imaginary axes correspond to parameter combinations lying on one of these two boundaries.

The third equation (3.38) describes the splitting of the critical curve at off-axis points with any other value of ϕ . Checking the third curve following Appendix B, we find that for $\mu < 1/5$ it is a spurious solution of the resultant method. Only the $\mu \geq 1/5$ part of the curve defines a genuine parameter-space boundary between different topologies.

A closer inspection of equations (3.36) and (3.37) reveals that both are of third degree in s^2 , while equation (3.38) is of third degree in s^4 . Hence, the scale parameter s of all the boundaries can be expressed analytically as a function of μ . Instead, we present the results graphically in the parameter-space plot in the left panel of Figure 3.2. The boundaries described by equations (3.36), (3.37), and (3.38) are illustrated by the black, orange, and cyan curves, respectively. The boundaries reach the limits of the plot at $[\mu, s] = [0, 8^{-1/2}]$, $[0, 1]$, $[1/9, 0]$, and $[1, 1]$. At the $[1/5, 5^{-1/2}]$ triple point the critical curve passes through the monkey saddles.

Critical-curve Topologies — The plot of the parameter space in the left panel of Figure 3.2 identifies regions with different critical-curve topology. The right panel and its blown-up detail in Figure 3.5.2 include further subdivision by total cusp number, as discussed further below. For better orientation we mark the six topology regions in the left panel by letters A – F from top to bottom and left to right. Starting from the widest regime we proceed gradually to lower values of the separation s and mark regions in order of appearance. In case several regions appear at the same value of s , we mark them in order from lowest to highest central mass μ .

The critical-curve topologies corresponding to all regions are illustrated by the examples in Figure 3.4, where they are shown together with their caustics.

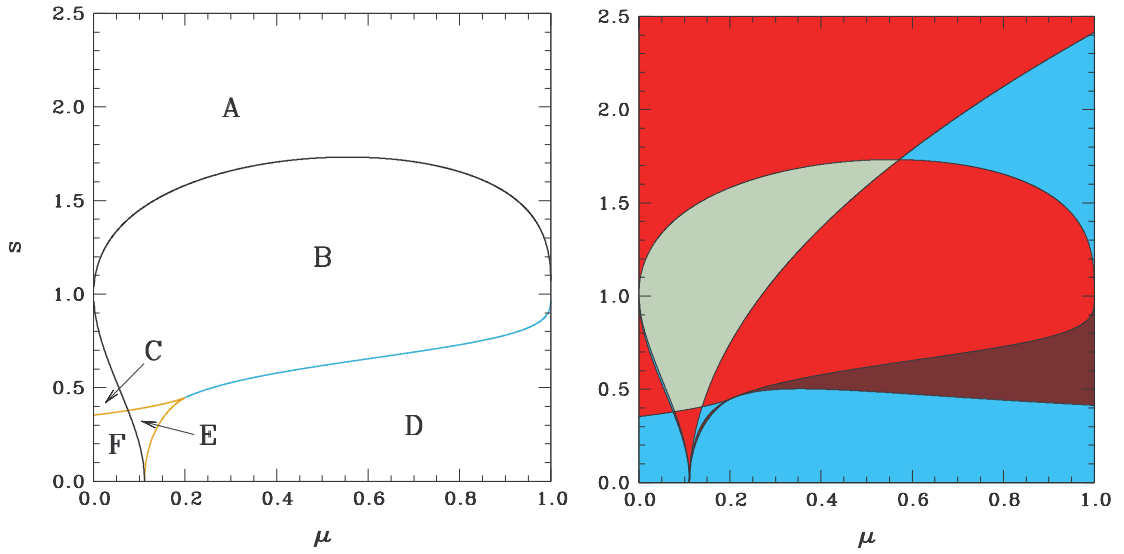


Figure 3.2 LS model – linear symmetric triple lens with variable central mass μ and separation s . Left panel: Parameter space divided into regions by critical-curve topology (marked by letters). Right panel: Parameter space divided into color-coded subregions by total number of cusps on caustic [8 cusps – gray; 12 – red; 16 – cyan; 20 – brown]. Region near lower left corner of right panel is blown up in Figure 3.5.2.

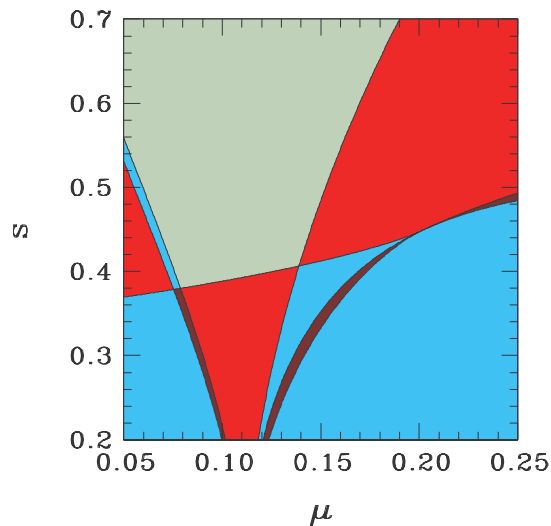


Figure 3.3 LS model: Detail of parameter-space division by total cusp number from Figure 3.2.

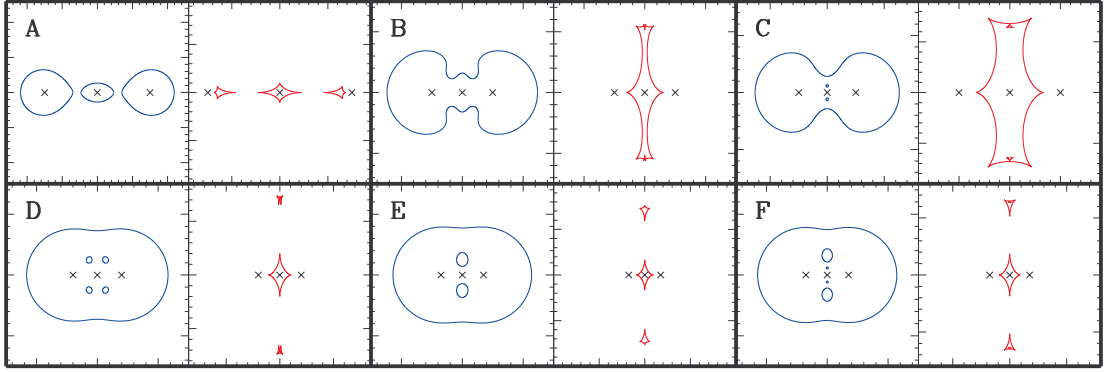


Figure 3.4 LS model: Gallery of topologies of critical curves (blue) and corresponding caustics (red) with lens positions marked by black crosses. Letters correspond to regions marked in Figure 3.2. Caustic subregions and lens parameters $[\mu, d]$ of examples: $A_1 [0.1, 1.5]$, $B_2 [0.2, 0.5]$, $C_1 [0.04, 0.5]$, $D_2 [0.2, 0.4]$, $E_3 [1/9, 0.35]$, $F_1 [0.07, 0.35]$.

Figure 3.5 includes examples of critical curves and caustics for transitions along the topology boundaries, marked by the letters of adjacent topology regions. The last two examples correspond to the boundary-intersection points seen in Figure 3.2.

As shown in Figure 3.4, the critical curve of the LS model consists of one (region B), three (regions A, C, E), or five loops (regions D, F). Not all the regions have a unique critical-curve topology: regions C+E, as well as D+F have the same topology. The linear symmetric triple lens thus has four distinct topologies: a single loop (B), three independent loops (A), an outer loop with two inner loops (C, E), or an outer loop with four inner loops (D, F). The topologies are summarized in the LS row of Table 3.1.

We inspect the curves in Figure 3.4 together with the parameter-space map in the left panel of Figure 3.2, in order to understand the occurrence of the different topologies and transitions between them. In the wide limit (region A) the three independent loops correspond to Einstein rings of the three components. Reducing the separation first leads to a simultaneous merger of all three loops at the real-axis saddles forming a single loop in region B, as shown by transition AB in Figure 3.5.

Further development with decreasing s depends on the value of μ . For $\mu < 0.0753$ the next transition BC leads to region C, splitting off inwards two loops around the inner pair of Jacobian maxima along the imaginary axis, followed by transition CF to region F, splitting from the outer loop another pair of loops around the outer pair of maxima along the imaginary axis. For $\mu \in (0.0753, 1/9)$ and $\mu \in (1/9, 1/5)$ the transition BE to region E splits off inwards two loops along the imaginary axis, each of which encloses two maxima. For $\mu \in (0.0753, 1/9)$ the next transition EF to region F splits each of the inner loops into a vertical pair along the imaginary axis, while for $\mu \in (1/9, 1/5)$ transition DE to region D splits the inner loops into horizontal pairs bracing the imaginary axis. Finally, for $\mu > 1/9$ transition BD to region D splits off simultaneously four loops from four different points along the outer loop.

The three remaining special cases, $\mu \approx 0.0753$, $\mu = 1/9$, and $\mu = 1/5$, are

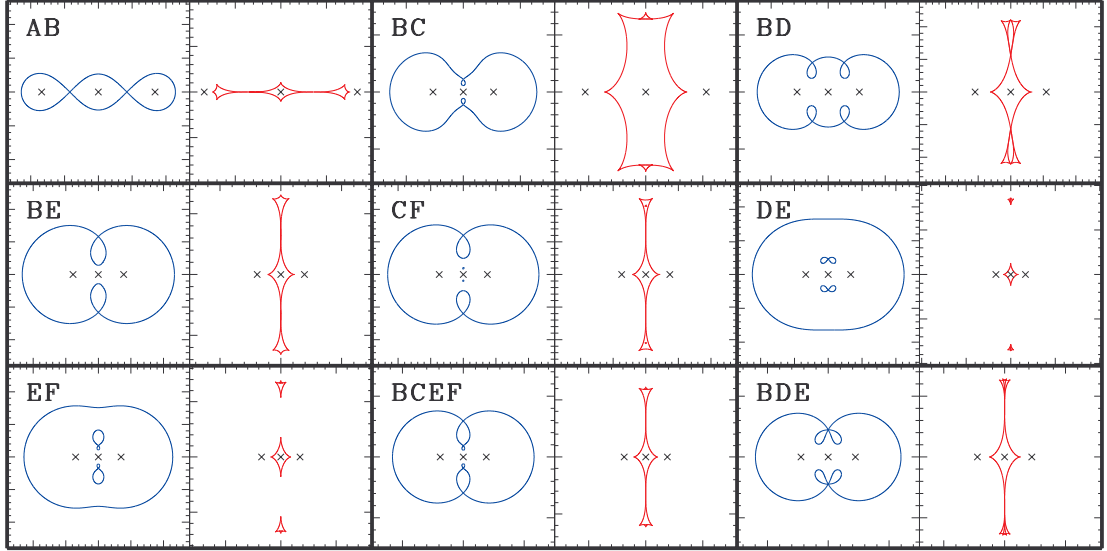


Figure 3.5 LS model: Gallery of critical curves (blue) and corresponding caustics (red) in transitions between the regions $[\mu, s]$ marked in Figure 3.2. Letters denote all adjacent regions. Lens parameters $[\mu, s]$ of examples: AB $[1/3, 1.6777]$, BC $[0.05, 0.53075]$, BD $[1/3, 0.54593]$, BE $[0.1, 0.38852]$, CF $[0.05, 0.36951]$, DE $[0.15, 0.33]$, EF $[0.08, 0.34866]$, BCEF $[0.07530, 0.37866]$, BDE $[1/5, 5^{-1/2}]$.

illustrated and discussed together with their caustic structure under the “Jacobian Contour Plots” heading further below.

Caustic Structure — The number of cusps on the caustic changes in beak-to-beak, butterfly, and swallow-tail metamorphoses. These can be found by studying the intersections of the cusp and morph curves, as discussed in § 3.4. The polynomial form of both curves for the LS model is provided in Appendix C.

The butterfly and swallow-tail metamorphoses introduce additional boundary curves that lead to a finer division of parameter space by total cusp number. The number is color-coded in the right panel of Figure 3.2 and in Figure 3.5.2. Topology regions A and D are divided into two, B into three, and E into four subregions, with regions C and F undivided. For better orientation we mark each subregion by the letter of the region and a subscript number assigned similarly within the region from top to bottom and left to right.

A gallery of caustics corresponding to all 13 subregions can be found in Figure 3.6 together with transition caustics BCEF and BDE. For each marked subregion there is a pair of panels showing the full caustic plus a blown-up detail. Already at first inspection we can identify a range of local features that do not occur in two-point-mass lens caustics, such as self-intersecting loops (e.g., A_2 , E_2), nested (C_1) or overlapping (D_2 , F_1) loops. The caustic structures generated in butterfly metamorphoses can be seen in A_2 , B_2 , D_1 , E_1 , E_2 ; swallow-tail-generated structures in B_3 , E_4 .

Inspecting the caustic changes along parameter-space boundaries, we find there are two types of beak-to-beak metamorphoses. The transition from two tangent folds to two facing cusps may lead to the formation of an additional loop. This is always the case in two-point-mass lenses, and it occurs here in transitions B-A (B_1 - A_1 , B_2 - A_2), B-D (B_2 - D_1), B-E (B_2 - E_1 , B_1 - E_3 , B_3 - E_4) and C-F

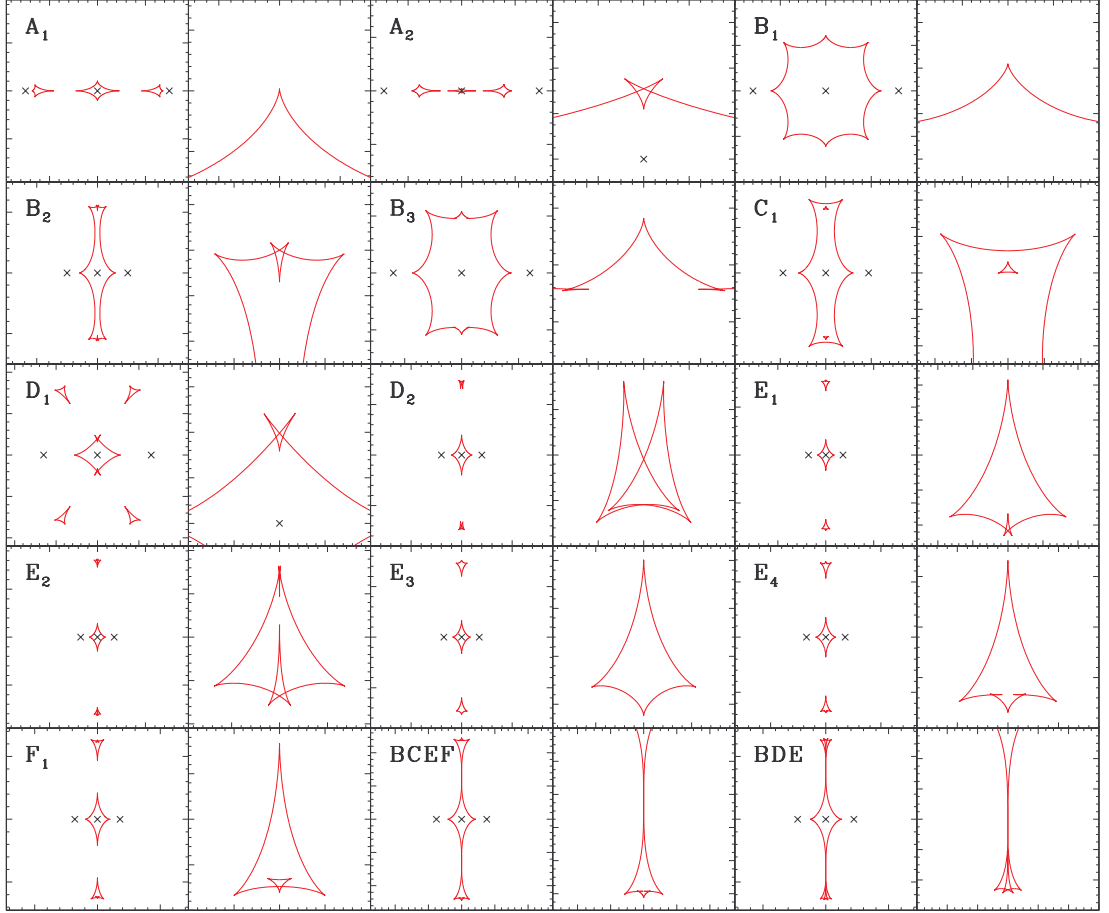


Figure 3.6 LS model: Gallery of caustics with blown-up details from 13 subregions of right panel of Figure 3.2, plus two transition caustics. Labels mark cusp-number subregions, with numbers assigned within given region from top to bottom and left to right in Figure 3.2. Lens parameters $[\mu, s]$ of examples: A_1 $[0.1, 1.5]$, A_2 $[0.95, 1.45]$, B_1 $[0.2, 0.8]$, B_2 $[0.2, 0.5]$, B_3 $[0.04, 0.6]$, C_1 $[0.04, 0.47]$, D_1 $[0.7, 0.65]$, D_2 $[0.2, 0.4]$, E_1 $[0.15, 0.36]$, E_2 $[0.155, 0.35]$, E_3 $[1/9, 0.35]$, E_4 $[0.08, 0.35]$, F_1 $[0.07, 0.36]$; BCEF $[0.07530, 0.37866]$, BDE $[1/5, 5^{-1/2}]$.

(C_1 - F_1). However, we find the transition may just as well result in the opposite, i.e., the merger of two loops. This can be seen here in transitions C-B (C_1 - B_3), D-E (D_2 - E_2), and F-E (F_1 - E_4), always starting from overlapping loops and ending in a self-intersecting loop. Hence, in the triple lens the formation of a cusp pair in the beak-to-beak metamorphosis may either increase or decrease the number of caustic loops.

Studying the new boundaries in the right panel of Figure 3.2, we note they are formed by three curves, all ending at $[\mu, s] = [1/9, 0]$. The curve leading from $[1, \sqrt{2} + 1]$ through regions A, B, E, and the curve leading from $[1, \sqrt{2} - 1]$ through regions D, E are both associated with butterfly metamorphoses. The specific transitions include A_1 - A_2 , B_1 - B_2 , E_3 - E_1 along the first, and D_2 - D_1 , E_1 - E_2 along the second curve. The third curve leads from $[0, 1]$ and shadows the adjacent topology boundary from the right side through regions B and E, as seen better in Figure 3.5.2. This curve is associated with swallow-tail metamorphoses (B_1 - B_3 , E_3 - E_4).

The total cusp number in the LS model varies from 8 (subregion B_1 marked gray in Figures 3.2 and 3.5.2) via 12 (A_1, B_2, C_1, E_3 – red) and 16 (A_2, B_3, D_2, E_1, F_1 – cyan) to 20 (D_1, E_2, E_4 – brown). Due to the high symmetry of the model, single metamorphoses never occur – always at least two occur simultaneously. As a result, the total cusp number in this case always changes in multiples of four, with the largest number of cusps appearing in the local transition from B_1 (8 cusps) to E_4 (20 cusps) just to the right of boundary intersection BCEF. There is more diversity in cusp numbers of individual caustic loops, which have 3, 4, 6, 8, 12 (B_2) or 16 (B_3) cusps. The occurrence of different loop combinations is summarized in column LS of Table 3.2.

Jacobian Contour Plots — Following the examples given by (21), we present in Figure 3.7 Jacobian contour plots for three special cases: $\mu \approx 0.0753$, $\mu = 1/9$, and $\mu = 1/5$. The panels in the upper row illustrate the critical-curve sequences along vertical $\mu = \text{const.}$ cuts in the parameter-space plots. In each panel we mark the $d = 0.5$ critical curve in bold for orientation. We recall that for lower d values the critical curves correspond to the outer contours plus the inner loops around the Jacobian maxima, while for higher d values they correspond to the inner contours around the lens positions. Note that the central ($\mu = 1/9$) and right ($\mu = 1/5$) columns are the only cases of the LS model with four saddles instead of the generic six, as discussed above.

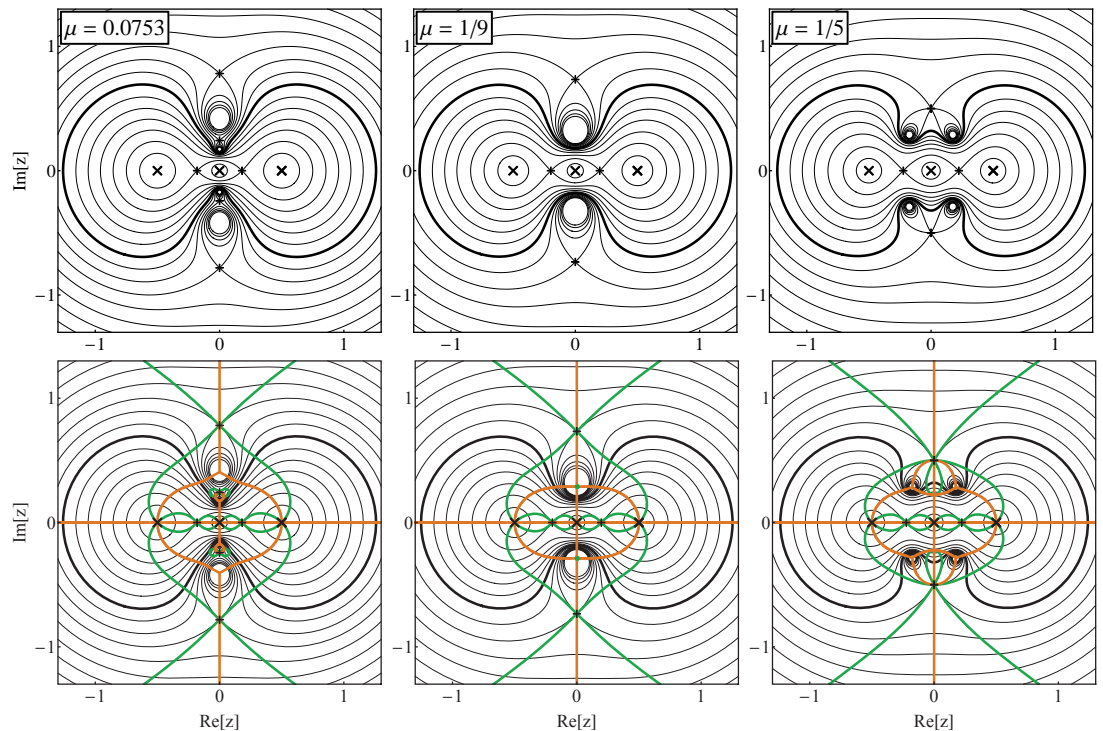


Figure 3.7 LS model: Jacobian contour plots for BCEF boundary intersection at $\mu \approx 0.0753$ (left column), for double maxima at $\mu = 1/9$ (central column), and for BDE monkey saddles at $\mu = 1/5$ (right column). Lower row includes cusp curves (orange) and morph curves (green). Contour values differ from column to column. Bold black contour: critical curve for $s = 0.5$; crosses: lens components; pluses: Jacobian saddle points.

The panels in the lower row include the corresponding cusp (orange) and

morph (green) curves, which identify the number and distribution of cusps on the corresponding caustics. In all cases the contours closest to the lenses have four intersections with the cusp curve around each lens, corresponding to three 4-cusped caustic loops in the wide-limit subregion A_1 . The outermost contours corresponding to the close-limit Einstein ring have four cusp-curve intersections too. Hence, the central caustic loop has four cusps as well, whether in subregion F_1 (left), E_3 (central), or D_2 (right column).

At $\mu \approx 0.0753$ (left column) the critical-curve sequence is A-B-F, and the caustic sequence is A_1 - B_1 - B_3 - F_1 . The transition from B via the boundary intersection BCEF directly to region F splits off simultaneously all four inner loops along the imaginary axis. The tiny loops around the inner pair of maxima are barely discernible just interior of the inner pair of saddles along the imaginary axis (see also Figure 3.5). Each of the small contours around the maxima has three cusp-curve intersections, implying a set of four 3-cusped caustic loops in the corresponding region F_1 . Inspecting the morph curve, note the somewhat hard-to-see four simultaneous B_1 - B_3 swallow-tail metamorphoses. These are indicated by the four simple intersections of the small figure-eight parts of the morph curve with the small loops of the cusp curve.

In the $\mu = 1/9$ case (central column), the critical-curve sequence is A-B-E, and the caustic sequence is A_1 - B_1 - E_3 . Here there are only two double maxima, so that the critical curve stays in region E even in the limit $s \rightarrow 0$. For this value of μ the close-limit topology of the critical curve has an outer Einstein ring with only two small loops inside. In the lower panel we see that either of these loops has four intersections with the cusp curve. This means that the corresponding caustic loops have four instead of three cusps in the $s \rightarrow 0$ limit in subregion E_3 . This configuration is an example of the “multiple caustics” case studied by (14).

The $\mu = 1/9$ case is generally the only case with neither butterfly nor swallow-tail metamorphoses, as seen also from the right panel of Figure 3.2. The cusp and morph curves intersect only at the positions of the lenses, saddles, and higher-order maxima. The higher-order maxima are isolated solutions of the morph-curve equation (3.28). When perturbed to lower μ values, these points turn into the horizontal figure-eight loops of the morph curve, as seen in the left $\mu \approx 0.0753$ column. Similarly, when perturbed to higher μ values, they turn into vertical figure-eight loops that eventually merge with the outer part of the morph curve at the $\mu = 1/5$ monkey saddles.

At $\mu = 1/5$ (right column) the critical-curve sequence is A-B-D, and the caustic sequence is A_1 - B_1 - B_2 - D_2 . Here the transition from B to D via the pair of monkey-saddle points at BDE splits off simultaneously all four inner loops around off-axis maxima, with the splitting occurring pairwise from the two monkey saddles (see also Figure 3.5). The small contours around the maxima each have three cusp-curve intersections, hence they correspond to four 3-cusped caustic loops in subregion D_2 . Inspecting the morph curves in the lower panel, we first notice the characteristic structure at the monkey saddles. In each of them the cusp curve arrives from four perpendicular directions, while the morph curve arrives from six symmetric directions. The corresponding caustic has two beak-to-beak metamorphoses with each involving three beaks. These can be seen in the BDE case triple-loop contact in the last panel of Figure 3.6. Note also the additional tangent intersections of the cusp and morph curves on the imaginary

axis closer to the origin. These correspond to two simultaneous B₁-B₂ butterfly metamorphoses, as expected from Figure 3.2.

Note that yet another LS-model Jacobian plot (for the $\mu = 1/3$ equal-mass case) can be found further in the right column of Figure 3.10, where it corresponds to the LA model with position parameter $p = 1/2$. Its LS-model sequence of caustic subregions is A₁-B₁-B₂-D₁-D₂.

Planetary Limits — The LS model has two different planetary-mass limits. In the $\mu \rightarrow 0$ case we have an equal-mass binary with separation $2s$ and a planet of mass μ placed exactly between its components (at the L1 Lagrangian point). In order of decreasing s the caustic sequence is A₁-B₁-B₃-C₁-F₁. At both limits, the planet merely adds tiny extra loops to the binary caustic: the central loop in A₁, and the pair of extra 3-cusped loops in C₁ and F₁. The planet perturbs primarily the $s = 1$ wide – intermediate binary transition, which occurs at the position of the planet. Here, in the single-loop subregions B₁ and B₃ the planet adds extra cusps to the caustic perpendicularly to the binary axis.

In the $\mu \rightarrow 1$ case we have a star with two equal-mass planets at opposite sides at a separation s . Here the caustic sequence is A₁-A₂-B₂-D₁-D₂. In the limiting subregions A₁ and D₂ the planets perturb the point-like single-lens caustic to form the central 4-cusped loop (16), adding two (A₁) or four (D₂) extra tiny loops. However, in subregions A₂, B₂, D₁ covering the separation range $s \in [\sqrt{2} - 1, \sqrt{2} + 1]$ the planets generate extra cusps on the central loop at positions perpendicular to the orientation of the system. The strongest effect occurs when the planets lie at the $s = 1$ Einstein radius, generating the single-loop caustic B₂.

Close Limit — For $\mu \neq 1/9$ (subregions F₁, D₂): critical curve = Einstein ring + four small loops around Jacobian maxima; caustic = central 4-cusped loop + four 3-cusped loops escaping to ∞ . For $\mu = 1/9$ (E₃): critical curve = Einstein ring + two small loops around Jacobian maxima; caustic = central 4-cusped loop + two 4-cusped loops escaping to ∞ (see also 14).

Wide Limit — For any μ (subregion A₁): critical curve = three independent Einstein rings with radii $\{\sqrt{(1-\mu)/2}, \sqrt{\mu}, \sqrt{(1-\mu)/2}\}$; caustic = three 4-cusped weak-shear Chang-Refsdal loops.

3.5.3 LA Model: Linear Asymmetric Configuration

Model Description — In the LA model three equal-mass lens components lie along a line with a variable separation of the outer two components, marked $2s$ to conform with the previous LS model. Here the second parameter is the relative separation p of the central component from the left component in units of the outer component separation (see second sketch in Figure 3.1). Placing the origin at the geometrical center and the lenses along the real axis, the positions and masses of the components are $\{z_1, z_2, z_3\} = \{-p - 1, 2p - 1, 2 - p\} 2s/3$ and $\{\mu_1, \mu_2, \mu_3\} = \{1/3, 1/3, 1/3\}$, with parameter ranges $p \in (0, 1)$ and $s \in (0, \infty)$.

The parametrization is symmetric about $p = 1/2$, so that the configurations, critical curves, and caustics for p and $1 - p$ are mutual mirror images. In the $p \rightarrow 0$ limit components 1 & 2 merge, so that the lens is reduced to a binary lens with masses $2/3, 1/3$. Similarly, in the $p \rightarrow 1$ limit components 2 & 3 merge. For $p = 1/2$ the components are spaced symmetrically, hence these configurations are identical with the $\mu = 1/3$ configurations of the LS model and with the $\theta = \pi$

configurations of the TI model discussed further in § 3.5.5.

Jacobian Surface Character — For any p : four simple maxima + six simple saddles.

Topology Boundaries — Due to the components having equal masses, we get the center of mass $d_1 = 0$, and the remaining three moments are $c_2 = 4 s^2(1-p+p^2)/3$, $d_2 = 2 c_2/3$, and $c_3 = 8 s^3(-p-1)(2p-1)(2-p)/27$. The critical-curve polynomial

$$p_{crit}(z) = z^6 - (2c_2 + e^{2i\phi})z^4 - 2c_3z^3 + c_2^2z^2 + 2c_3(c_2 - e^{2i\phi})z + c_3^2 - c_2^2e^{2i\phi}/3 = 0 \quad (3.39)$$

and the saddle-point polynomial

$$p_{sadd}(z) = z^6 + c_2z^4 + 7c_3z^3 + c_2^2z^2 - c_3c_2z + c_3^2 - c_2^3/3 = 0 \quad (3.40)$$

generally cannot be solved analytically. We proceed to identify the boundaries of parameter-space regions with different critical-curve topologies using the resultant method described in § 3.3.2 applied directly to polynomials p_{crit} and p_{sadd} .

The first resultant yields the polynomial equation

$$p_{res}(w) = (8 - \nu)w^6 + 6(12 - \nu)c_2w^5 + 216c_2^2w^4 - (216 - 198\nu + 11\nu^2)c_2^3w^3 - 3\nu(45 - 14\nu)c_2^4w^2 - 18\nu^2c_2^5w + \nu^3c_2^6 = 0, \quad (3.41)$$

where $w = e^{2i\phi}$ and the parameter $\nu \equiv 27p^2(1-p)^2/(1-p+p^2)^3$. The equation depends on s through the moment c_2 . The second resultant can be factorized to yield three independent conditions. The first, $p_{res}(1) = 0$, describes the splitting of the critical curve at $\phi = 0$ as a 6th-degree polynomial in s^2 . The second, $p_{res}(-1) = 0$, would describe the splitting of the critical curve at $\phi = \pi/2$. However, this condition has no solution in our parameter space, hence such splitting does not occur in the LA model. The third condition describes the splitting of the critical curve at any other value of ϕ . It has the form of a 15th-degree polynomial in s^4 , which we do not present here explicitly. An inspection following Appendix B reveals an entire spurious branch of the corresponding curve in parameter space.

The $p_{res}(1) = 0$ and the 15th-degree polynomial boundaries are marked in the parameter-space plot in the left panel of Figure 3.8 by the black and cyan curves, respectively. The curves meet the $p = 0, 1$ limits at $s = (\sqrt[3]{2} - 1)^{-1/2}/2 \approx 0.981$ and $s = (\sqrt[3]{2} - 1)^{1/4}/2 \approx 0.357$, respectively.

Critical-curve Topologies — The division of parameter space by critical-curve topology is shown in the left panel of Figure 3.8. In view of the $p \leftrightarrow (1-p)$ symmetry, we use letters to mark the six different regions within the left half of the parameter space (from top to bottom and left to right), and mark their symmetric counterparts by the same letters.

The topologies corresponding to all regions are illustrated by the examples presented in Figure 3.9 together with their caustics. The LA model permits a greater range of critical-curve topologies than the LS model, with each region having a unique topology. In addition to all the topologies seen previously in the LS model (Figure 3.4), there is a 2-loop (region B) and a 4-loop (region A) topology. In region B one of the two independent loops contains two lens components, while in region A there is a simple loop plus a close-binary set of loops (two small loops within an outer loop). Neither of these can be achieved

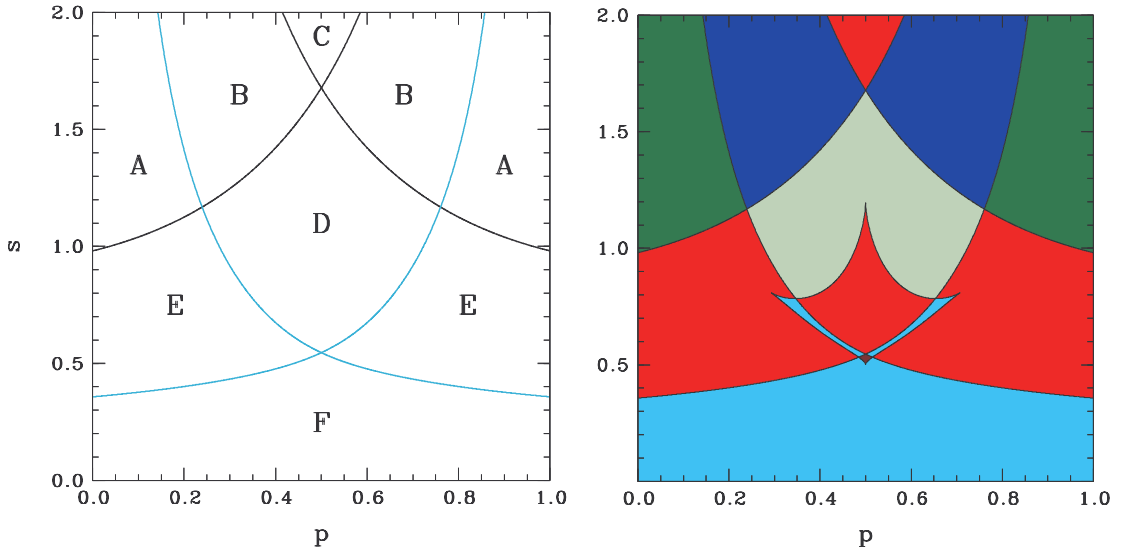


Figure 3.8 LA model parameter-space division. Left panel: by critical-curve topology (marked by letters), with black boundary given by $p_{res}(1) = 0$, cyan by 15th-degree polynomial in s^4 (see § 3.5.3). Right panel: by total number of cusps on caustic [8 cusps – gray; 10 – blue; 12 – red; 14 – green; 16 – cyan; 20 – brown].

in the symmetric LS model. Note also that the single-loop topology (region D) occurs only for $p \in (0.239, 0.761)$. In other cases with decreasing s the loop around the pair of components undergoes the intermediate – close binary transition (B-A) before connecting with the third-component loop (A-E). All topologies are summarized in the LA row of Table 3.1.

Caustic Structure — The further subdivision of parameter space according to total cusp number is shown in the right panel of Figure 3.8. The number of cusps on the caustic changes primarily in beak-to-beak metamorphoses. Unlike in the case of the LS model, all are of the standard type with cusp formation accompanying the splitting of caustic loops. Other metamorphoses occur only in the limited range $p \in (0.292, 0.708)$, as seen from the extent of the additional duck-foot-shaped boundary in Figure 3.8. The curve corresponds to a pair of swallow-tail metamorphoses, with the exception of its two points on the $p = 1/2$ midline. The higher symmetry at these points leads to a pair of butterfly metamorphoses at each. The new boundary divides regions D, E, and F into two subregions each, while the other regions remain undivided. In comparison with the other models, each of the nine subregions has a unique caustic structure, as seen from column LA of Table 3.2.

The LA model has a lower degree of symmetry than the LS model, so that beak-to-beak metamorphoses along the real axis may occur singly and the total cusp number thus may change by 2. The total cusp number varies from 8 to 20 in steps of two, with one exception: there is no 18-cusped caustic in the LA model. The newly occurring totals are 10 cusps (subregion B_1 marked blue in Figure 3.8) and 14 cusps (A_1 – green). In comparison with the LS model, there are caustic loops with 10 cusps (B_1), but there are no loops with 16 cusps.

Jacobian Contour Plots — In Figure 3.10 we present Jacobian contour plots for three cases: $p = 0.18, 0.45, 1/2$. The latter two were used by (21) to illustrate the swallow-tail and butterfly metamorphoses, respectively. The $p = 1/2$ caustic

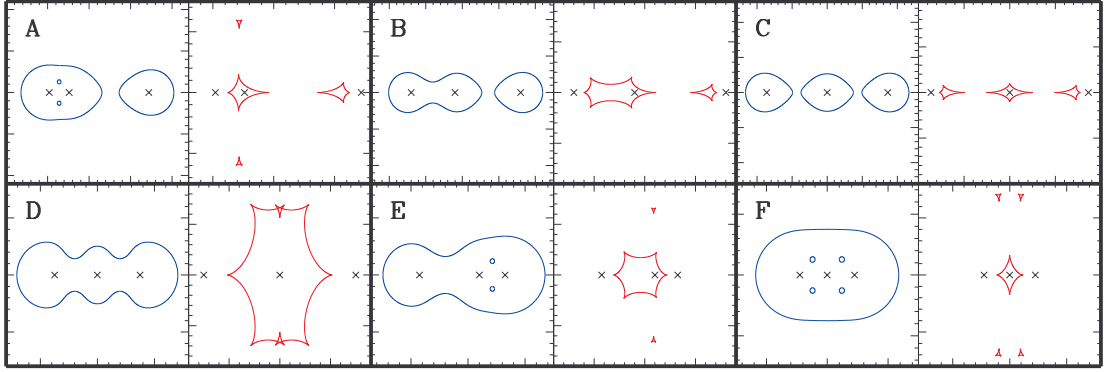


Figure 3.9 LA model: Gallery of topologies of critical curves (blue) and corresponding caustics (red) with lens positions marked by black crosses. Letters correspond to regions marked in Figure 3.8. Caustic subregions and lens parameters $[p, d]$ of examples: A_1 $[0.2, 1.2]$, B_1 $[0.4, 1.5]$, C_1 $[0.5, 1.725]$, D_2 $[0.5, 0.75]$, E_1 $[0.7, 0.75]$, F_2 $[0.5, 0.45]$.

sequence from wide to close limit is C_1 - D_1 - D_2 - F_1 - F_2 , with transitions D_1 - D_2 and F_2 - F_1 each involving a pair of simultaneous butterfly metamorphoses. The $p = 0.45$ caustic sequence is C_1 - B_1 - D_1 - D_2 - E_2 - E_1 - F_2 , with transitions D_1 - D_2 and E_1 - E_2 each involving a pair of simultaneous swallow-tail metamorphoses.

The $p = 0.18$ case in the left column illustrates a hierarchical triple system, with components 1 and 2 forming a binary and component 3 as a distant companion. The structure of the contours and curves near the first two components resembles a simple equal-mass binary (see 21) with its wide, intermediate, and close regimes. If we ignore the local structure around components 1 & 2, on the large scale the contours and curves again resemble a binary system with its three regimes, here with a 2:1 mass ratio since components 1 & 2 act as a single body. The caustic sequence C_1 - B_1 - A_1 - E_1 - F_2 undergoes no swallow-tail, no butterfly, and no single-loop topology.

Planetary Limits — The LA model has no planetary limit.

Close Limit — For any p (subregion F_2): critical curve = Einstein ring + four small loops around Jacobian maxima; caustic = central 4-cusped loop + four 3-cusped loops escaping to ∞ .

Wide Limit — The wide limit is more interesting, with three different regimes for arbitrarily large separation $s \rightarrow \infty$. In this limit the model behaves as an equal-mass binary lens plus an independent single lens. The three regimes are simply the close (subregion A_1), intermediate (B_1), and wide (C_1) regimes of the binary lens. The wide regime, which eventually dominates, leads to three independent single lenses with Einstein radii $\sqrt{1/3}$.

This behavior can be proved by the $s \rightarrow \infty$ asymptotic form of the boundaries in Figure 3.8: in the $p < 1/2$ part the A-B boundary is given by $2ps = \sqrt{1/3}$, and the B-C boundary by $2ps = \sqrt{8/3}$. Noting that $2ps$ is the separation between lens components 1 and 2 (see Figure 3.1), if we divide the two values by the Einstein radius of the binary ($\sqrt{2/3}$), we get the close – intermediate and intermediate – wide boundaries of the equal-mass binary lens. To summarize: critical curve = binary critical curve + Einstein ring with radius $\sqrt{1/3}$; caustic = binary caustic + 4-cusped weak-shear Chang-Refsdal loop.

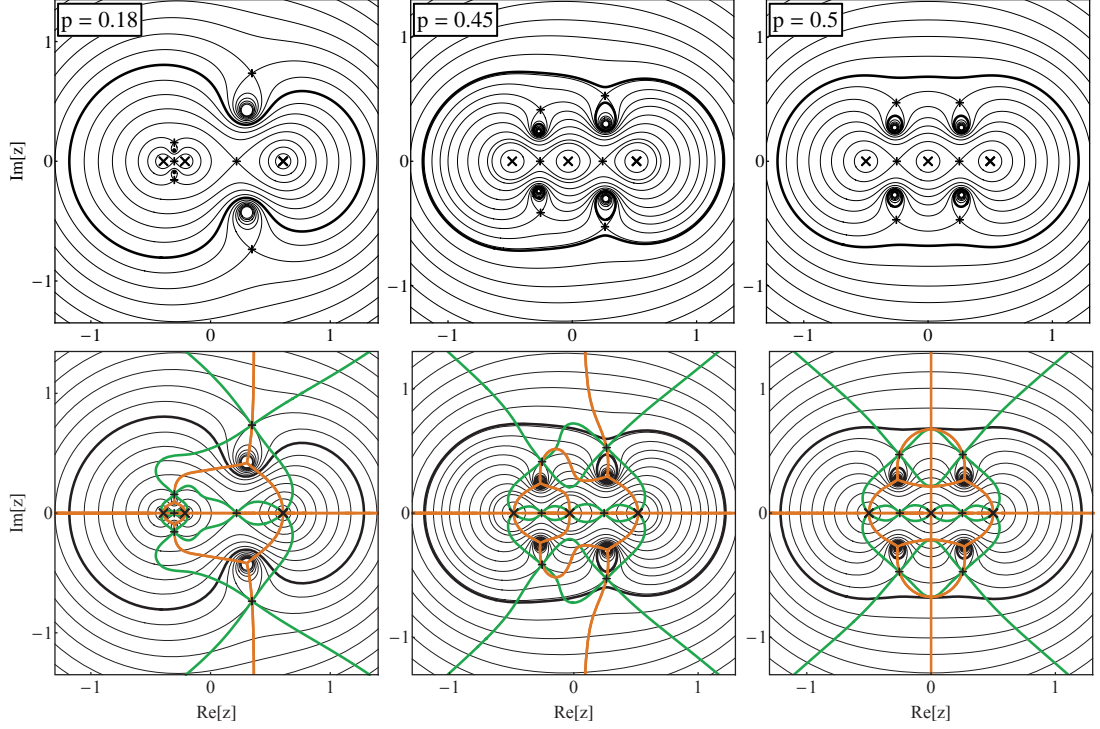


Figure 3.10 LA model: Jacobian contour plots in regime of binary lens with distant companion at $p = 0.18$ (left column), for the nearly symmetric $p = 0.45$ (central column), and the symmetric case $p = 0.5$ (right column). Lower row includes cusp curves (orange) and morph curves (green). Contour values differ from column to column. Notation as in Figure 3.7.

It is worth noticing that the presence of the distant third body along the binary axis has no effect on the critical curve topology or caustic structure of the binary lens, it merely adds a distant loop. Similarly, the structure of the plots in Figure 3.8 near the left boundary indicates that a tiny separation of components 1 & 2 along the axis to component 3 has no effect on the critical curve topology or caustic structure of the 2:1 mass-ratio binary lens, it merely adds two tiny loops.

3.5.4 TE Model: Equilateral Triangle Configuration

Model Description — In the TE model the lens components lie at the vertices of an equilateral triangle with side length s (see third sketch in Figure 3.1). We use the fractional mass μ of component 1 as the second parameter. Placing the origin at the geometrical center and aligning the real axis with the median passing through component 1, the positions and masses of the components are $\{z_1, z_2, z_3\} = \{-1, e^{-i\pi/3}, e^{i\pi/3}\} s/\sqrt{3}$ and $\{\mu_1, \mu_2, \mu_3\} = \{\mu, (1-\mu)/2, (1-\mu)/2\}$, with parameter ranges $\mu \in (0, 1)$ and $s \in (0, \infty)$.

The $\mu = 0$ limit corresponds to an equal-mass binary formed by components 2 & 3, while the $\mu = 1$ limit corresponds to component 1 as a single lens. The $\mu = 1/3$ case is the most symmetric triple lens: three equal masses in an equilateral configuration. It is identical with the $\theta = \pi/3$ case of the TI model discussed further in § 3.5.5.

Jacobian Surface Character — For $\mu \neq 0.768, 8/9$: four simple maxima + six simple saddles; for $\mu \approx 0.768$: two simple maxima + one double maximum + five simple saddles; for $\mu = 8/9$: four simple maxima + four simple saddles + one monkey saddle. In addition, note that the $\mu = 1/3$ equal-mass case is unique due to its global three-fold symmetry.

Topology Boundaries — Due to the equilateral configuration $c_2 = 0$, the center of mass $d_1 = (1 - 3\mu)s/\sqrt{12}$, $c_3 = -s^3/\sqrt{27}$, and $d_2 = -(1 - 3\mu)s^2/6$. The critical-curve polynomial

$$p_{crit}(z) = z^6 - e^{2i\phi} z^4 - 2(c_3 + d_1 e^{2i\phi}) z^3 - 3d_2 e^{2i\phi} z^2 - 2c_3 e^{2i\phi} z + c_3(c_3 - d_1 e^{2i\phi}) = 0 \quad (3.42)$$

and the saddle-point polynomial

$$p_{sadd}(z) = z^6 + 3d_1 z^5 + 6d_2 z^4 + 7c_3 z^3 + 6c_3 d_1 z^2 + 3c_3 d_2 z + c_3^2 = 0 \quad (3.43)$$

cannot be solved analytically for a general μ . We use the resultant method described in § 3.3.2 applied to polynomials p_{crit} and p_{sadd} to identify the boundaries of regions in parameter space with different critical-curve topologies.

The first resultant yields the polynomial equation

$$\begin{aligned} p_{res}(w) = & (\tau^3 - 3\tau^2 + 1) w^6 \\ & - 3\tau (3\tau^4 - 12\tau^3 + 8\tau^2 + 3\tau - 3) s^2 w^5 - 3\tau (23\tau^3 - 20\tau^2 - 8\tau + 7) s^4 w^4 \\ & + (6\tau^3 + 12\tau^2 - 11) s^6 w^3 + 6\tau (\tau - 2) s^8 w^2 + 3\tau s^{10} w - s^{12} = 0, \end{aligned} \quad (3.44)$$

where $w = e^{2i\phi}$ and the parameter $\tau \equiv (3\mu - 1)/2$ is equal to zero for an equal-mass lens. The second resultant can be factorized to yield four independent conditions. The first two, $p_{res}(1) = 0$ and $p_{res}(-1) = 0$, describe the splitting of the critical curve at $\phi = 0$ and $\phi = \pi/2$, respectively, in the form of 6th-degree polynomials in s^2 . The other two conditions describe the splitting of the critical curve at other values of ϕ . Both have the form of polynomials in s^4 (3rd and 12th degree, respectively), which we do not present here explicitly. An inspection following Appendix B reveals that only a segment of the 3rd-degree polynomial curve corresponds to topology transitions, the rest is spurious.

The $p_{res}(1) = 0$, $p_{res}(-1) = 0$, the 3rd- and 12th-degree polynomial boundaries are marked in the parameter-space plot in the left panel of Figure 3.11 by the black, orange, cyan, and green curves, respectively. The boundaries reach the $\mu = 0$ side of the plot at $s = \sqrt{1/2}$ and $s = 2$, the $\mu = 1$ side at $s = 1$, and the $s = 0$ side at $\mu = 1 - (4/3)\sin \pi/18 \approx 0.768$. At the $[\mu, s] = [8/9, \sqrt{1/2}]$ triple point the critical curve passes through a monkey saddle.

Critical-curve Topologies — The division of parameter space by critical-curve topology is shown in the left panel of Figure 3.11. The right panel and its blown-up details in Figure 3.12 include the further subdivision according to total cusp number. The four curves identified above carve the parameter space in the left panel into ten different topology regions, marked by letters from top to bottom and left to right.

For each region examples of critical curves with their corresponding caustics are presented in Figure 3.13. We see that the critical curve may have anywhere from 1 to 5 loops. In comparison with the previous models, there are two new topologies: a small loop within an outer loop (region D), and three small loops

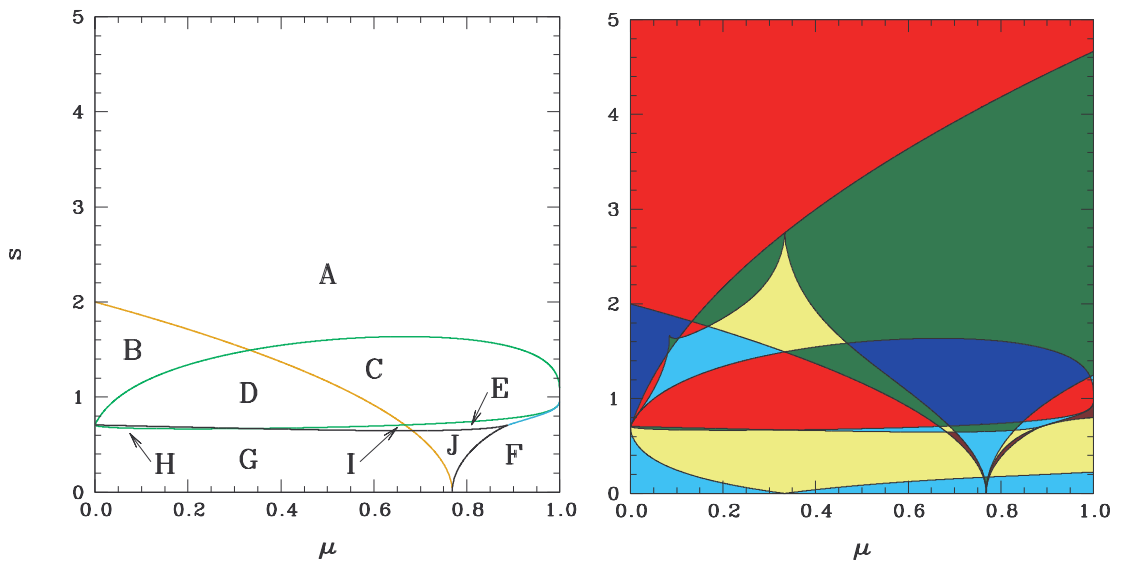


Figure 3.11 TE model parameter-space division. Left panel: by critical-curve topology (marked by letters), with black boundary given by $p_{res}(1) = 0$, orange by $p_{res}(-1) = 0$, cyan by 3rd-degree and green by 12th-degree polynomials in s^4 (see § 3.5.4). Right panel: by total number of cusps on caustic [10 cusps – blue; 12 – red; 14 – green; 16 – cyan; 18 – yellow; 20 – brown]. Region near lower right corner of right panel is blown up in Figure 3.12.

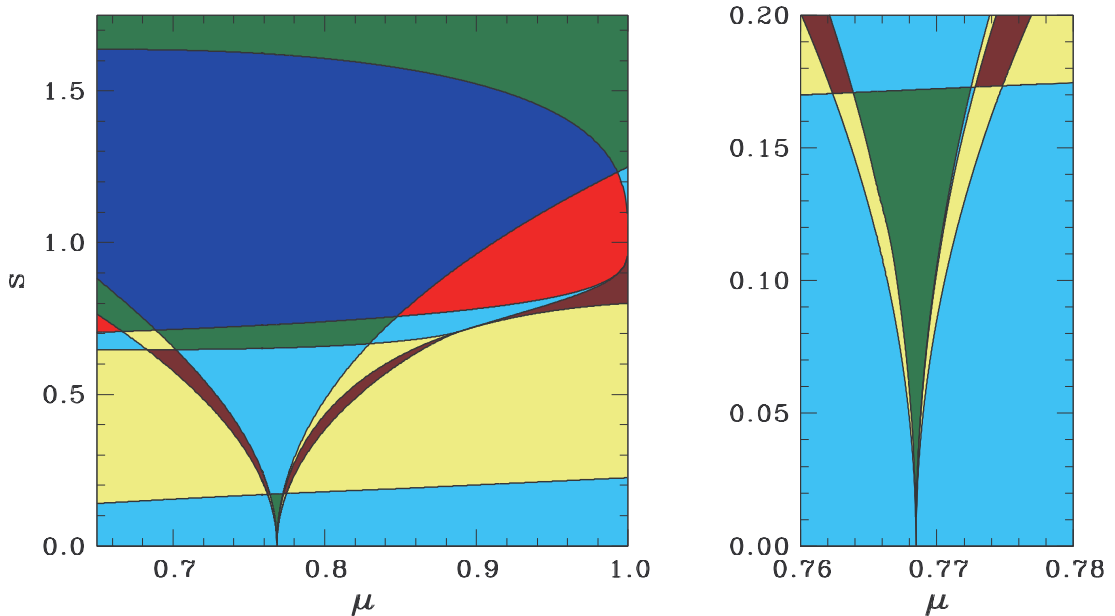


Figure 3.12 TE model: Parameter-space division by total cusp number. Left panel: Detail from Figure 3.11. Right panel: Detail from left panel near close limit of double-maximum configuration.

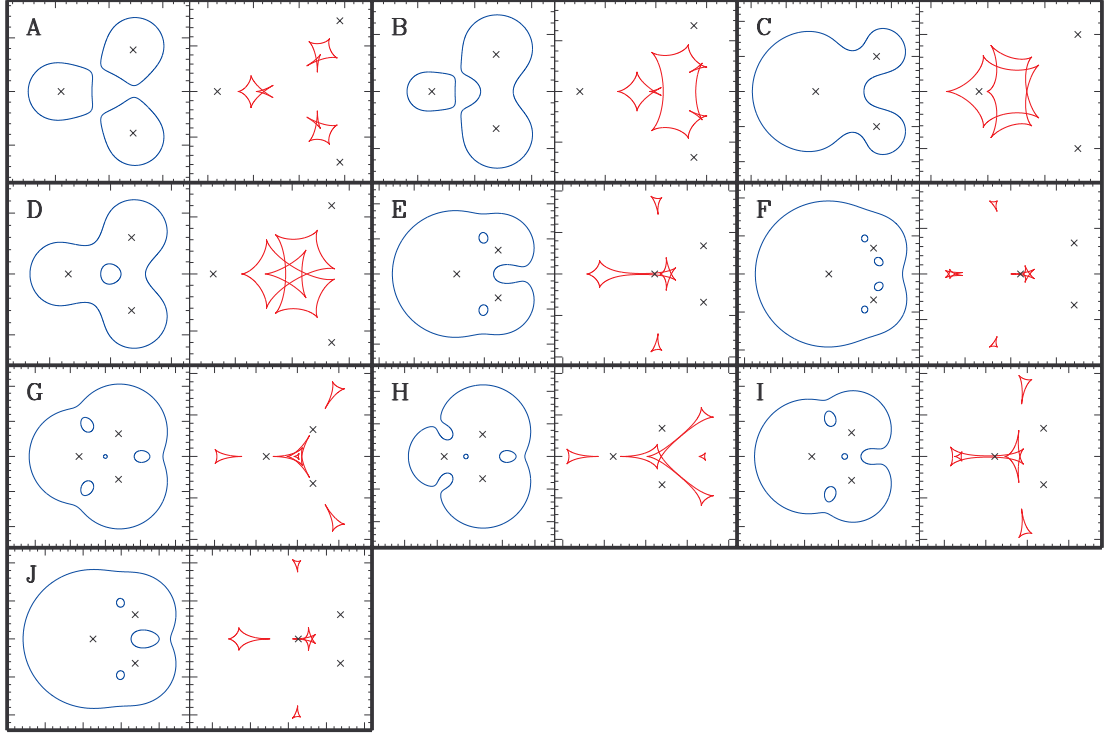


Figure 3.13 TE model: Gallery of topologies of critical curves (blue) and corresponding caustics (red) with lens positions marked by black crosses. Letters correspond to regions marked in Figure 3.11. Caustic subregions and lens parameters $[\mu, s]$ of examples: A_4 $[1/3, 1.55]$, B_3 $[0.15, 1.3]$, C_1 $[0.7685, 1.0]$, D_1 $[1/3, 1.2]$, E_2 $[0.7685, 0.68]$, F_2 $[0.9, 0.68]$, G_2 $[1/3, 0.65]$, H_1 $[0.15, 0.68]$, I_1 $[0.6, 0.68]$, J_3 $[0.7685, 0.64]$.

within an outer loop (I, J). Only one of the previous models' topologies doesn't occur here: the simple loop plus a close-binary set of loops (model LA region A). As seen from the TE row of Table 3.1, this model permits altogether 7 different critical topologies, since the pairs of regions E+H, F+G, and I+J each share the same topology.

The beak-to-beak metamorphoses along most of the topology boundaries increase the number of critical-curve loops, with a decrease occurring only for the D-C, I-E, G-J, and F-J transitions. In addition, the TE model has the special case of the D-B transition, in which two simultaneous beak-to-beaks convert an outer-plus-inner loop combination to two separate loops, thus preserving the total number of loops.

Caustic Structure — The subdivision of parameter space by number of cusps on the caustic is shown in the right panel of Figure 3.11 and in Figure 3.12. As seen in both figures, many additional metamorphoses change the cusp number. There are four curves corresponding to butterfly and one curve corresponding to swallow-tail metamorphoses.

Two of the butterfly curves start from $[0, \sqrt{1/2}]$: one leading down through G to $[1/3, 0]$, returning back through G, J, and F to $s = -1 + \sqrt{3} - \sqrt{2 - \sqrt{3}} \approx 0.214$ at the right edge; the second goes up through B and A to $s = 1 + \sqrt{3} + \sqrt{2 + \sqrt{3}} \approx 4.66$ at the right edge. The other two butterfly curves rise monotonously from

$[0.768, 0]$ toward the right side: the third through J and F to $s = 1 + \sqrt{3} - \sqrt{2 + \sqrt{3}} \approx 0.800$; the fourth through J, E, C, and A to $s = -1 + \sqrt{3} + \sqrt{2 - \sqrt{3}} \approx 1.25$.

Finally, the swallow-tail curve starts from $[0, \sqrt{1/2}]$ and leads up through B with a small sharp peak at $\mu \approx 0.084$ to A, where it peaks sharply when it meets the butterfly curve at $\mu = 1/3$, dropping down through A, C, E, and J to $[0.768, 0]$. The curve corresponds to a complex-conjugate pair of swallow-tail metamorphoses everywhere except at the two sharp peaks. At the $\mu = 1/3$ peak three symmetric butterfly metamorphoses occur simultaneously, while at the $\mu \approx 0.084$ peak there is a complex-conjugate pair of butterfly metamorphoses.

The additional set of curves in the right panel of Figure 3.11 (with details better seen in Figure 3.12) divides regions C, E, F, and G into three subregions each, regions A and B into five subregions, and region J into eight subregions. Regions D, H, and I remain undivided. The parameter space of the TE model is thus divided into 33 subregions, corresponding to 24 different loop combinations. These are sorted by cusp number and listed in column TE of Table 3.2. The total cusp number varies from 10 to 20 in steps of two; i.e., there is no 8-cusped caustic. Caustics with 18 cusps that appear newly in this model occur in 7 different subregions (see Table 3.2). Individual caustic loops have 3, 4, 6, 7, 8, 9, 10, 12 or 14 cusps. In comparison with the previous models there is no 16-cusped loop (B_3 in LS model), while 7-cusped (I_1 shown in Figure 3.13) and 9-cusped loops (D_1 in Figure 3.13) are new here.

Jacobian Contour Plots — Figure 3.14 includes contour plots for three special cases: $\mu = 1/3$, $\mu \approx 0.768$, and $\mu = 8/9$. In the symmetric $\mu = 1/3$ case the caustic sequence from wide to close limit is A_1 - A_4 - D_1 - G_2 , with the A_1 - A_4 three simultaneous butterfly metamorphoses at $s = 2^{2/3} 3^{1/2} \approx 2.75$. The D_1 - A_4 three simultaneous beak-to-beaks occur at $s = [(5\sqrt{5} + 11)/2]^{1/6} \approx 1.49$, and the D_1 - G_2 three simultaneous beak-to-beaks occur at $s = [(5\sqrt{5} - 11)/2]^{1/6} \approx 0.670$. There is no single-loop topology, but with the slightest perturbation to a higher μ the sequence would visit the C_2 single-loop region with a 14-cusped caustic.

The double-maximum case in the central $\mu \approx 0.768$ column has a caustic sequence A_1 - A_2 - C_1 - E_2 - J_3 - J_7 with two butterfly metamorphoses along the real axis. The plot requires a larger scale due to the close-limit J_7 - J_3 butterfly point near the right edge of the inset.

The same holds also for the $\mu = 8/9$ monkey-saddle case in the right column. The caustic sequence A_1 - A_2 - C_1 - C_3 - E_1 - F_2 - F_3 starts out similarly, but differs once the components get closer. The three butterfly points all lie on the real axis.

Planetary Limits — The TE model has two different planetary-mass limits, similar to those of the LS model. The $\mu \rightarrow 0$ limit describes an equal-mass binary separated by s with a planet of mass μ offset perpendicularly at the vertex of an equilateral triangle (at the L4 Lagrangian point for a face-on coplanar orbit⁴). In order of decreasing s , the caustic undergoes a sequence of seven metamorphoses: A_1 - B_1 - B_5 - B_3 - D_1 - H_1 - G_2 - G_1 . The two widest regimes, A_1 and B_1 , correspond to a wide and intermediate binary caustic, respectively, each with an additional 4-cusped loop due to the planet. Similarly, G_1 corresponds to a close binary caustic with two additional 3-cusped loops due to the planet.

All six metamorphoses between B_1 and G_1 occur close to the $s = 1/\sqrt{2}$

⁴Note that in this case L4 is unstable, since $\mu_2 = \mu_3$.

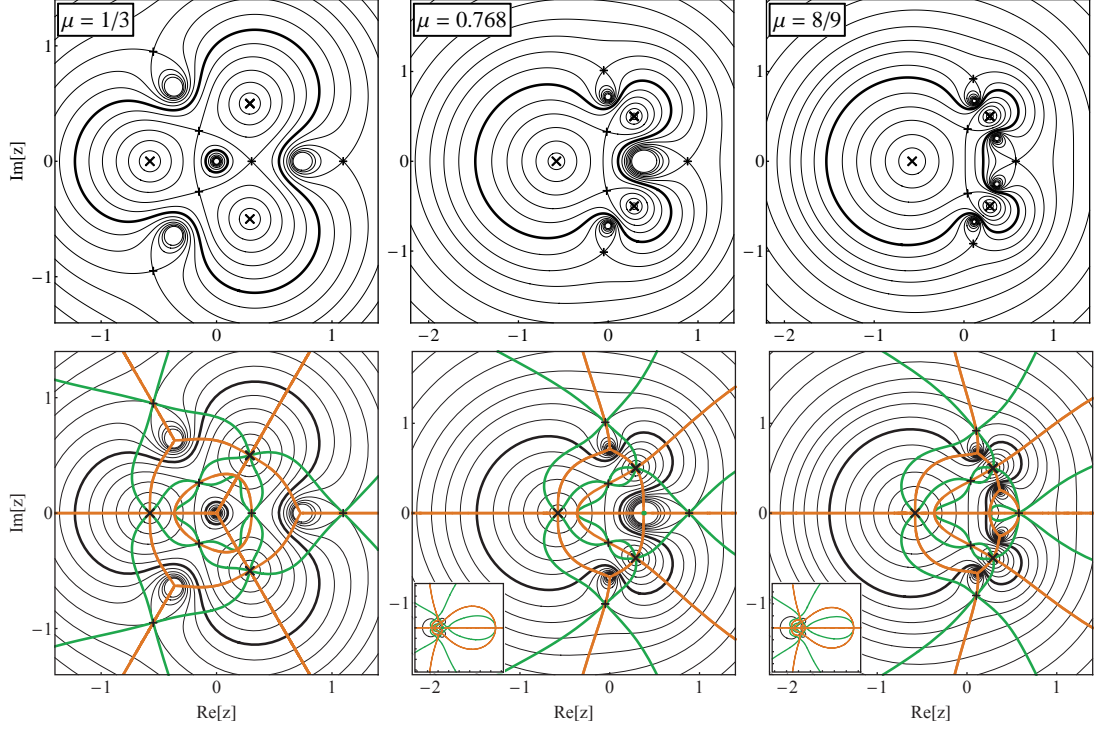


Figure 3.14 TE model: Jacobian contour plots for equal masses $\mu = 1/3$ (left column), for double maximum at $\mu \approx 0.768$ (central column), and for monkey saddle at $\mu = 8/9$ (right column). Lower row includes cusp curves (orange) and morph curves (green). Contour values differ from column to column. Insets in lower central and right panels: zoomed-out plots of critical, cusp, and morph curves. Notation as in Figure 3.7.

intermediate – close binary transition, since the planet lies exactly at the location at which one 3-cusped loop would split off in the binary limit. The sequence begins with a butterfly on the planetary loop leading to B_5 , followed by a pair of swallow tails on the binary-caustic loop to B_3 . In the peculiar transition to D_1 both loops connect in a pair of reverse beak-to-beaks, which simultaneously split off a 3-cusped loop. A second 3-cusped loop is formed along the real axis in a beak-to-beak to H_1 , and a third and fourth 3-cusped loop appear simultaneously in a pair of beak-to-beaks to G_2 . Finally, the main caustic loop loses two cusps in a reverse butterfly to G_1 .

The $\mu \rightarrow 1$ limit describes a single lens with two equal-mass planets at the same distance s , an angle of $\pi/3$ apart. Even in this case the caustic undergoes seven metamorphoses with decreasing s : A_1 - A_2 - A_5 - C_3 - E_1 - F_1 - F_2 - F_3 . In the A_1 wide limit, the caustic consists of three 4-cusped weak-shear Chang-Refsdal loops (16). In the F_3 close limit, the caustic has one 4-cusped weak-shear Chang-Refsdal loop for the star, plus two pairs of 3-cusped strong-shear Chang-Refsdal loops for the planets.

The butterfly metamorphosis from A_1 to A_2 , found on the caustic loop of the star at the cusp facing the planets, occurs already at a large distance of the planets – approaching $s \approx 4.66$ for $\mu \rightarrow 1$. The next butterfly to A_5 near $s \approx 1.25$ occurs on the caustic loop of the star at the tip of the first butterfly feature. The three following beak-to-beak transitions all occur near $s = 1$, the Einstein radius of the

single lens. First, the two planetary 4-cusped loops connect with the star's loop leading to C_3 , one pair of 3-cusped planetary loops then disconnects to E_1 , and another pair disconnects to F_1 . The last two metamorphoses occur on the star's loop: reverse butterflies near $s \approx 0.800$ to F_2 , and $s \approx 0.214$ to F_3 . We point out that even though the planetary loops of the caustic connect and disconnect when the planets lie close to the star's Einstein ring, the star's loop of the caustic is affected by having extra cusps for a much wider range of planetary distances, $s \in (0.214, 4.66)$.

Close Limit — For $\mu \neq 1/3, 0.768$ (subregions F_3, G_1, G_3): critical curve = Einstein ring + four small loops around Jacobian maxima; caustic = central 4-cusped loop + four 3-cusped loops escaping to ∞ . For $\mu = 1/3$ (G_2): critical curve = Einstein ring + four small loops around Jacobian maxima; caustic = central 6-cusped loop + three 3-cusped loops escaping to ∞ + one 3-cusped loop staying at center. For $\mu = 0.768$ (J_7): critical curve = Einstein ring + three small loops around Jacobian maxima; caustic = central 4-cusped loop + one 4-cusped and two 3-cusped loops escaping to ∞ .

The $\mu = 1/3$ equal-mass case exhibits a new close-limit behavior: the central caustic loop has six instead of four cusps, and one of the four 3-cusped loops stays at the center instead of escaping to ∞ (see Figure 3.13). The central caustic loop is self-intersecting with a three-fold symmetry, so that a pair of cusps points in the direction of each of the lens components. In the $s \rightarrow 0$ limit each pair rapidly converges to a point, so that the shape of the shrinking caustic loop approaches a simple symmetric 3-cusped loop, which is traced twice as one follows the corresponding Einstein ring. The nature of the central loop can be seen also from the contour plot in the left column of Figure 3.14. The six branches of the cusp curve extending symmetrically to the outer edges have six intersections with the outer contours, which represent the perturbed Einstein-ring loop in the close limit.

Wide Limit — For any μ (subregion A_1): critical curve = three independent Einstein rings with radii $\{\sqrt{\mu}, \sqrt{(1-\mu)/2}, \sqrt{(1-\mu)/2}\}$; caustic = three 4-cusped weak-shear Chang-Refsdal loops.

3.5.5 TI Model: Isosceles Triangle Configuration

Model Description — The final, topologically richest model has three equal-mass lens components lying at the vertices of an isosceles triangle, with legs of length s spanning a vertex angle θ (see fourth sketch in Figure 3.1). If we place the origin at the geometrical center, align the axis of symmetry with the real axis, and set component 1 at the vertex angle, the positions and masses of the components are $\{z_1, z_2, z_3\} = \{-e^{i\theta/2} - e^{-i\theta/2}, -e^{i\theta/2} + 2e^{-i\theta/2}, 2e^{i\theta/2} - e^{-i\theta/2}\} s/3$ and $\{\mu_1, \mu_2, \mu_3\} = \{1/3, 1/3, 1/3\}$, with parameter ranges $\theta \in (0, \pi)$ and $s \in (0, \infty)$.

In the $\theta = 0$ limit components 2 & 3 coincide, reducing the system to a binary lens with masses $\{1/3, 2/3\}$ and separation s . We recall that in the LA model both $p = 0$ and $p = 1$ edges correspond to a binary lens with the same mass ratio but with separation $2s$. The $\theta = \pi$ case corresponds to the collinear limit with component 1 at the center. Hence, the corresponding configurations are identical with the $\mu = 1/3$ case of the LS model, as well as the $p = 1/2$ case of the LA model. Similarly, configurations with vertex angle $\theta = \pi/3$ are identical with the

$\mu = 1/3$ configurations of the TE model.

Jacobian Surface Character — For $\theta \neq 0.124\pi, 0.708\pi, 0.847\pi$: four simple maxima + six simple saddles; for $\theta \approx 0.708\pi$: two simple maxima + one double maximum + five simple saddles; for $\theta \approx 0.124\pi$ and $\theta \approx 0.847\pi$: four simple maxima + four simple saddles + one monkey saddle. In addition, the $\theta = \pi/3$ equilateral case has global three-fold symmetry, as discussed in § 3.5.4.

Topology Boundaries — Since the masses are equal, the center of mass $d_1 = 0$, $c_2 = [1 - 4 \sin^2(\theta/2)] s^2/3$, $d_2 = 2c_2/3$, and $c_3 = -2 \cos(\theta/2)[1 + 8 \sin^2(\theta/2)] s^3/27$. The critical-curve polynomial

$$p_{crit}(z) = z^6 - (2c_2 + e^{2i\phi})z^4 - 2c_3z^3 + c_2^2z^2 + 2c_3(c_2 - e^{2i\phi})z + c_3^2 - c_2^2e^{2i\phi}/3 = 0 \quad (3.45)$$

and the saddle-point polynomial

$$p_{sadd}(z) = z^6 + c_2z^4 + 7c_3z^3 + c_2^2z^2 - c_2c_3z - c_2^3/3 + c_3^2 = 0 \quad (3.46)$$

cannot be solved analytically for a general θ . We use the resultant method described in § 3.3.2 applied to polynomials p_{crit} and p_{sadd} to identify the boundaries of regions in parameter space with different critical-curve topologies.

The first resultant yields the polynomial equation

$$\begin{aligned} p_{res}(w) = & [8(1-\kappa)^3 + 27\kappa]w^6 + 6(1-\kappa)[4(1-\kappa)^3 + 9\kappa]s^2w^5 \\ & + 24(1-\kappa)^5s^4w^4 - [8(1-\kappa)^6 + 198\kappa(1-\kappa)^3 + 297\kappa^2]s^6w^3 \\ & + 9\kappa(1-\kappa)[5(1-\kappa)^3 + 42\kappa]s^8w^2 - 54\kappa^2(1-\kappa)^2s^{10}w \\ & - 27\kappa^3s^{12} = 0, \end{aligned} \quad (3.47)$$

where $w = e^{2i\phi}$ and the parameter $\kappa \equiv 4 \sin^2 \theta/2$ is equal to unity for an equilateral configuration. The second resultant can be factorized to yield three independent conditions. The first two, $p_{res}(1) = 0$ and $p_{res}(-1) = 0$, describe the splitting of the critical curve at $\phi = 0$ and $\phi = \pi/2$, respectively, in the form of 6th-degree polynomials in s^2 . The third condition describes the splitting of the critical curve at other values of ϕ . It has the form of a 15th-degree polynomial in s^4 , which we do not present here explicitly. An inspection following Appendix B reveals that two segments of the corresponding curve have to be omitted, since they yield spurious solutions with no change in critical-curve topology.

The $p_{res}(1) = 0$, $p_{res}(-1) = 0$, and the 15th-degree polynomial boundaries are marked in the parameter-space plot in the left panel of Figure 3.15 by the black, orange, and cyan curves, respectively. The boundaries reach the $\theta = 0$ side of the plot at $s = (\sqrt[3]{2} - 1)^{1/4} \approx 0.714$ and $s = (\sqrt[3]{2} - 1)^{-1/2} \approx 1.96$, the $\theta = \pi$ side at $s \approx 0.546$ and $s \approx 1.68$, and the $s = 0$ side at $\theta \approx 0.708\pi$. At either of the $[\theta, s] \approx [0.124\pi, 1.76]$ and $[0.847\pi, 0.478]$ triple points the critical curve passes through a monkey saddle.

Critical-curve Topologies — The division of parameter space by critical-curve topology is shown in the left panel of Figure 3.15. The cusp-number map in the right panel and its blown-up details in Figure 3.16 include further subdivision by cusp number. The three curves obtained from the resultant analysis carve the parameter space into twelve different regions, marked by letters A – L in the left panel, from top to bottom and left to right.

For each region, examples of critical curves with their corresponding caustics are shown in Figure 3.17. The critical curve may have anywhere from 1 to 5 loops.

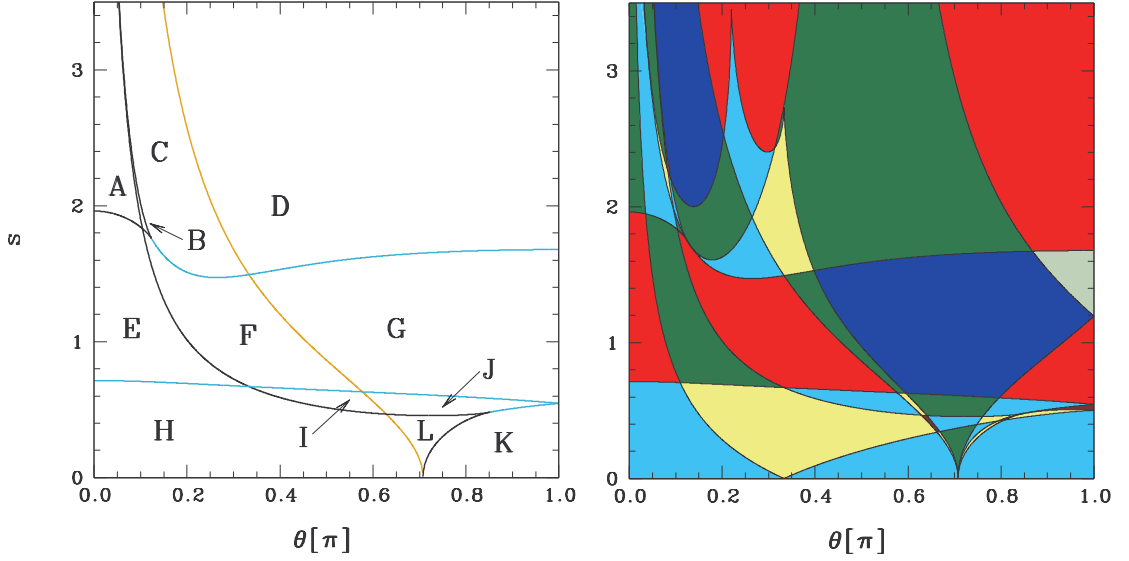


Figure 3.15 TI model parameter-space division. Left panel: by critical-curve topology (marked by letters), with black boundary given by $p_{res}(1) = 0$, orange by $p_{res}(-1) = 0$, cyan by 15th-degree polynomial in s^4 (see § 3.5.5). Right panel: by total number of cusps on caustic [8 cusps – gray; 10 cusps – blue; 12 – red; 14 – green; 16 – cyan; 18 – yellow; 20 – brown]. Regions near upper left and lower right corners of right panel are blown up in Figure 3.16.

The TI model has all the topologies found in the three previous models, plus one new topology: two separate loops, one of which contains a small third loop (region B). As seen from the TI row of Table 3.1, this model permits altogether 9 different critical topologies, since the pairs of regions E+J, I+L, and H+K each share the same topology.

The beak-to-beak metamorphoses along most of the topology boundaries increase the number of critical-curve loops, with a decrease occurring only for the F-G, I-J, H-L, and K-L transitions. Similarly to the D-B transition of the TE model, the TI model has the special F-C transition, in which two simultaneous beak-to-beaks convert an outer-plus-inner loop combination to two separate loops, preserving the total number of loops.

Caustic Structure — The cusp-number maps in the right panel of Figure 3.15 and in Figure 3.16 include subdivision due to additional caustic metamorphoses. Four of the five additional curves define conditions for butterfly, one for swallow-tail metamorphoses. Two of the butterfly curves asymptotically approach $\theta \rightarrow 0$ as $s \rightarrow \infty$: one leads down through A, E, and H to $[\theta, s] = [\pi/3, 0]$, rising back through H, L, and K to $s \approx 0.502$ at the right edge; the other leads down through A, B, and C, rising up through C and D to $s = \infty$ at $\theta = \pi/2$, dropping down through D and G to $s \approx 1.20$ at the right edge. The second pair of butterfly curves rises from $[0.708\pi, 0]$ to the right edge: one through L and K to $[\pi, 0.502]$; the other through L, J, and G to $[\pi, 1.20]$. All the butterfly metamorphoses defined by these four curves occur along the symmetry axis of the lens.

The swallow-tail curve starts asymptotically at $s \rightarrow \infty$ as $\theta \rightarrow 0$, dropping down through A, B, and C, rising up through C and D to a sharp peak at $\theta \approx 0.220\pi$, bouncing back to another sharp peak reaching the second butterfly

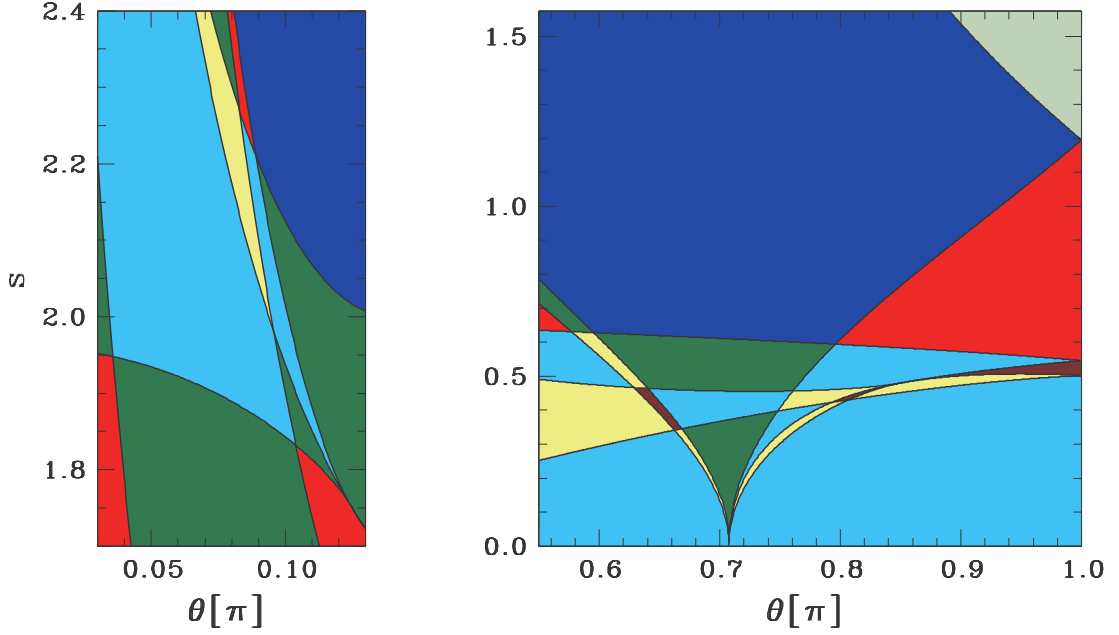


Figure 3.16 TI model: Parameter-space division by total cusp number. Left panel: Detail from upper left part of Figure 3.15. Right panel: Detail of lower right corner of Figure 3.15.

curve at $\theta = \pi/3$, dropping finally through D, G, J, and L to $[0.708\pi, 0]$. Just as in the TE model, the curve corresponds to a complex-conjugate pair of swallow-tail metamorphoses everywhere except at the two sharp peaks. At the $\theta = \pi/3$ peak, three symmetric butterfly metamorphoses occur simultaneously, while at the $\theta \approx 0.220\pi$ peak there is a complex-conjugate pair of butterfly metamorphoses. These are the only two cases within the TI model with butterflies occurring off the symmetry axis.

The additional set of curves divides region E into two subregions, regions B, C, H, J, and K into three subregions each, regions A and G into four, region D into six, and region L into eight subregions, with regions F and I remaining undivided. The parameter space of the TI model is thus divided into 41 subregions, corresponding to 28 different caustic-loop combinations. All are sorted by cusp number and listed in column TI of Table 3.2. The total cusp number varies from 8 to 20 in steps of two. Individual caustic loops have 3, 4, 5, 6, 7, 8, 9, 10, 12 or 14 cusps. In comparison with the previous models there is no 16-cusped loop (B_3 in LS model), while 5-cusped loops appear here newly (in subregion B_1).

Jacobian Contour Plots — Figure 3.18 includes contour plots for three special vertical transects through the parameter space. Vertex angle $\theta \approx 0.220\pi$ in the left column corresponds to the left sharp peak of the swallow-tail curve in Figure 3.15. The caustic sequence from wide to close limit is D_1 - D_4 - C_2 - C_3 - F_1 - E_2 - H_2 - H_1 , with no single-loop topology and no swallow-tail metamorphosis. The inset includes the H_1 - H_2 butterfly metamorphosis close to its right edge. Note the special F-C pair of beak-to-beaks at the $\text{Re}[z] \approx -0.14$ saddle points, in which two nested loops reconnect to form two separate loops.

The D_1 - D_4 simultaneous complex-conjugate pair of butterflies is indicated by the morph curve passing through self-intersection points of the cusp curve near $\text{Re}[z] \approx 0.15$. These self-intersections disappear for any perturbation of θ . For

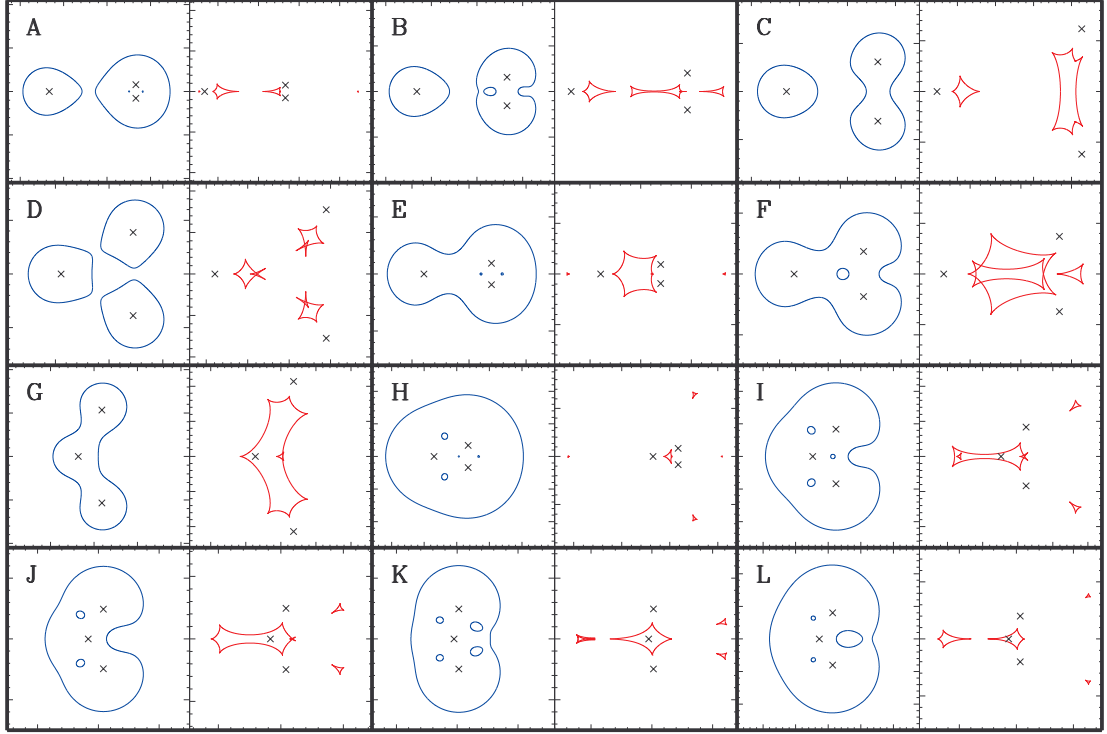


Figure 3.17 TI model: Gallery of topologies of critical curves (blue) and corresponding caustics (red) with lens positions marked by black crosses. Letters correspond to regions marked in Figure 3.15. Caustic subregions and lens parameters $[\theta, s]$ of examples: A_2 $[0.05\pi, 2]$, B_2 $[0.1\pi, 2]$, C_2 $[0.2\pi, 2]$, D_6 $[\pi/3, 1.55]$, E_2 $[0.1\pi, 1.2]$, F_1 $[0.2\pi, 1.2]$, G_2 $[0.7\pi, 1.2]$, H_2 $[0.2\pi, 0.55]$, I_1 $[0.55\pi, 0.55]$, J_2 $[0.7\pi, 0.55]$, K_2 $[0.9\pi, 0.5]$, L_4 $[0.7\pi, 0.45]$.

lower values the cusp curve at the upper point splits along a SW-NE axis, for higher values along a NW-SE axis. In either case only one of the two separated branches intersects the morph curve, corresponding to a complex-conjugate pair of swallow tails.

The central $\theta = \pi/2$ column has the caustic sequence D_2 - G_2 - G_3 - F_1 - I_1 - H_2 - H_1 . The G_2 - G_3 pair of swallow tails occurs in the image plane on the central small figure-8 loop of the morph curve, and the H_1 - H_2 butterfly can be seen at the left edge of the inset. The peculiar feature occurring at this angle is the six-cusped loop around the left component in the wide limit (D_2). In the double-maximum $\theta \approx 0.708\pi$ case in the right column the caustic sequence D_3 - D_2 - G_2 - J_2 - L_4 - L_7 ends with a 4-cusped caustic loop corresponding to the double-maximum critical-curve loop.

Two further transects of the TI model can be found in contour plots of other models. The symmetric $\theta = \pi/3$ case appears as the $\mu = 1/3$ left column of the TE-model Figure 3.14 (TI-model caustic sequence: D_1 - D_6 - F_1 - H_2). The linear $\theta = \pi$ case appears rotated by $\pi/2$ as the $p = 0.5$ plot of the LA model in Figure 3.10 (TI-model: D_3 - G_1 - G_4 - K_1 - K_3).

Planetary Limits — The TI model has no planetary limit.

Close Limit — For $\theta \neq \pi/3, 0.708\pi$ (subregions H_1, H_3, K_3): critical curve = Einstein ring + four small loops around Jacobian maxima; caustic = central 4-cusped loop + four 3-cusped loops escaping to ∞ . For $\theta = \pi/3$ (H_2): critical

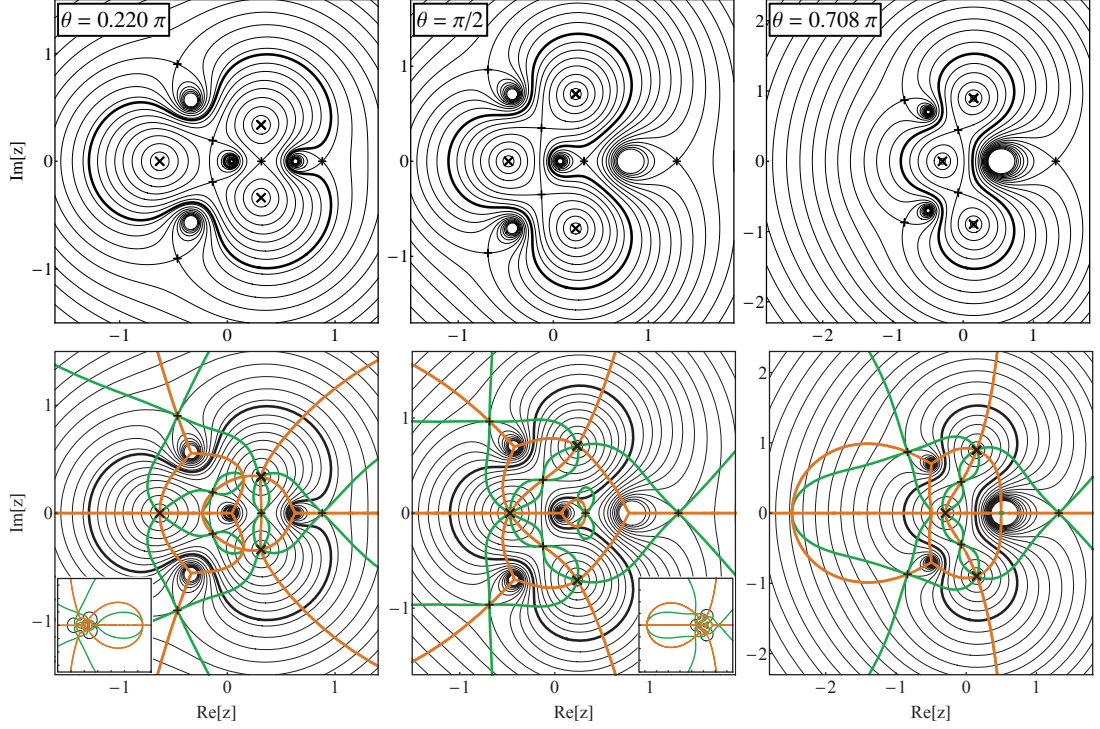


Figure 3.18 TI model: Jacobian contour plots for off-axis butterflies at $\theta \approx 0.220 \pi$ (left column), for Chang-Refsdal violating $\theta = \pi/2$ (central column), and for double maximum at $\theta \approx 0.708 \pi$ (right column). Lower row includes cusp curves (orange) and morph curves (green). Contour values differ from column to column. Insets in lower panels: zoomed-out plots of critical, cusp, and morph curves. Notation as in Figure 3.7.

curve = Einstein ring + four small loops around Jacobian maxima; caustic = central 6-cusped loop + three 3-cusped loops escaping to ∞ + one 3-cusped loop staying at center. For $\theta = 0.708 \pi$ (L_7): critical curve = Einstein ring + three small loops around Jacobian maxima; caustic = central 4-cusped loop + one 4-cusped and two 3-cusped loops escaping to ∞ .

Wide Limit — It is the wide limit that is particularly interesting here. For any fixed θ the $s \rightarrow \infty$ limit corresponds to three single lenses with Einstein radii $\sqrt{1/3}$. However, for $\theta \sim s^{-1}$ the wide limit describes an equal-mass binary formed by components 2 & 3 with a distant object offset perpendicularly from the binary axis. This is analogous to the $p \sim s^{-1}$ wide limit in the LA model with a distant object lying along the binary axis (see § 3.5.3). The TI model has a total of nine different caustic regimes for arbitrarily large leg length $s \rightarrow \infty$. In order of increasing vertex angle θ these are: $A_1, A_2, A_3, A_4, B_1, C_1, D_1, D_2,$ and D_3 . The regimes can be grouped by the character of the binary lens formed by components 2 & 3: close (topology region A), intermediate (C), and wide (D). Topology B and the caustic subregion structure are the results of perturbation of the binary by the distant companion – as well as perturbation of the companion by the binary.

The additional topology B (see Figure 3.17) occurs at the close – intermediate boundary. The influence of the companion causes the opposite inner loop to connect with the outer loop before the adjacent one, rather than both con-

necting simultaneously. In the asymptotic $s \rightarrow \infty$ regime B becomes negligible, as can be seen from the topology boundaries. The separation of binary components 2 & 3 (see Figure 3.1) along the A-B boundary is asymptotically $2s \sin(\theta/2) \simeq (1 + s^{-2}/6 - s^{-3}/6)/\sqrt{3}$, while along the B-C boundary we get $2s \sin(\theta/2) \simeq (1 + s^{-2}/6 + s^{-3}/6)/\sqrt{3}$. The two expressions differ only at the s^{-3} order. For completeness, the asymptotic C-D boundary yields $2s \sin(\theta/2) \simeq \sqrt{8/3}$. Normalizing the asymptotic separations by the $\sqrt{2/3}$ Einstein radius of the binary, we recover the standard close – intermediate A-(B)-C and intermediate – wide C-D boundaries of an equal-mass binary.

The wide-limit caustic in regions A through C always has a 4-cusped weak-shear Chang-Refsdal loop for the distant companion. The binary part of the caustic is dominated by the close-binary structure in A_1 : three loops with 4+3+3 cusps. Increasing the separation causes the main loop to undergo two subsequent butterfly metamorphoses to A_2 (6+3+3) and A_3 (8+3+3), followed by a pair of reverse swallow tails to A_4 (4+3+3). One 3-cusped loop merges with the main loop to B_1 (5+3), followed by the other to reach the intermediate regime C_1 (6), which then splits into two in the wide-binary regime D_1 (4+4). The structure of the binary part does not change further in the D region.

At larger vertex angles in region D, it is the companion loop of the caustic that undergoes an interesting transition. The butterfly entrance to D_2 turns the loop into a 6-cusped self-intersecting curve. This structure disappears in a reverse butterfly when exiting to D_3 . While for any other angle an increase in s would eventually return the 6-cusped loop to the regular 4-cusped regime, for $\theta = \pi/2$ the peculiar shape persists for $s \rightarrow \infty$. In this limit each of the three pairs of cusps converge to a point, so that the shape approaches a 3-cusped loop traced twice. The caustic loop is similar to the 6-cusped loop in the close limit of the equal-mass TE model.

We stress that in this regime all three components lie at arbitrarily large separations. Still, the configuration alters the caustic loop of the component at the vertex fundamentally. This effect is caused by the gravitational fields of the other two components, which combine so that they exactly cancel the lensing shear term. Hence, the Chang-Refsdal limit is not valid in this special case. Even though this occurs in the TI model for $s \rightarrow \infty$ only for $\theta = \pi/2$, for any fixed not-too-large value of s there is an interval of angles, for which the simple Change-Refsdal shape of the caustic loop cannot be assumed.

3.5.6 Overview of critical-curve topologies and caustic structures

In Table 3.1 we summarize the occurrence of the nine different critical-curve topologies in the parameter spaces of the four studied triple-lens models. The topologies are listed first in order of increasing total number of loops, then by decreasing number of separate outer loops.

The total loop number ranges from one to five, with single 1-loop and 5-loop topologies, two different 2-loop and 4-loop topologies, and three different 3-loop topologies. The number of outer separate loops ranges from one to three, and the number of inner loops ranges from zero to four. Four of the topologies occur in all studied models: single loop, three separate loops (the generic wide limit), an outer

loop with two inner loops, and an outer loop with four inner loops (the typical close limit). These four are the only topologies found in the LS model. The LA model has six, the TE model seven, and the TI model has all nine topologies.

The topologies found in the analyzed models are only examples of the possible topologies of triple-lens critical curves, so the list in Table 3.1 is by no means exhaustive. All of the studied models are symmetric by their geometry and mass combination; all have at least one reflection symmetry. Breaking the symmetries of the models opens up the possibility of additional critical-curve topologies. However, finding the overall number of topologies of the triple lens is beyond the scope of this work. Such a survey would require a detailed investigation of the geometry of the Jacobian surface and the positions and types of its maxima, saddles, and poles. The correspondence with Jacobian contours may prove to be another useful tool, which may identify the possible sequences of topology changes when scaling the lens from the wide to the close limit.

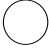









Finally, we point out that the topologies discussed here are those that occur in two-dimensional areas of the parameter space of their models. One may proceed further and classify also the critical-curve topologies of all transitions between the different marked topology regions, such as those shown in Figure 3.5. While this would be a straightforward extension, we do not include it here since the present work is extended enough already.

Table 3.2 presents an overview of all 32 different caustic structures in the parameter spaces of the four studied triple-lens models. Here we identify the caustic structure purely by the combination of cusp numbers on the individual loops. In the notation used in the first column of the table, for example $16/10+3+3$ identifies a caustic with a total 16 cusps on three loops: one with 10, and two with 3 cusps each. The caustics are ordered in the table first by increasing total cusp number, then in decreasing order by the number of cusps on individual loops.

The total cusp number runs from 8 to 20 in increments of 2. The 8-cusped caustics have only a single-loop structure, the 10-cusped caustics have two, 12-cusped caustics three, 14-cusped caustics four, 16-cusped caustics five, 18-cusped caustics six, and 20-cusped caustics seven. Individual loops have 3 – 10, 12, 14, or 16 cusps. Least common are the 5-cusped loop (the $12/5+4+3$ caustic in the TI/B₁ subregion), and the 16-cusped loop (the $16/16$ caustic in the LS/B₃ subregion). There are only 4 caustic structures that occur in all four studied models: $12/12$, $12/4+4+4$ (includes the generic wide limit), $16/4+3+3+3+3$ (includes the generic close limit), and $20/8+3+3+3+3$. The LS model has 10, the LA model has only 9, the TE model has 24, and the TI model has 28 different caustic structures, lacking only four of all the found possibilities.

The list in Table 3.2 is based purely on the cusp numbers on loops of the caustic. If we took into account the combination of critical-curve topology and caustic structure, the list would expand to 37 different cases. The reason for this is that a given caustic structure may occur for different mutual positions of critical-curve loops. For example, two 4-cusped loops of the caustic may correspond to two separate loops of the critical curve, or to an outer and inner loop of the critical curve. An inspection of the topologies in Table 3.1 shows that this is the case for the $12/4+4+4$ caustic in the LS model from the A vs. E regions; the $16/6+6+4$ caustic in the TI model D region vs. LS model E region; the $14/4+4+3+3$ caustic in the LA and TI model A regions vs. the TE model J region and TI model L

Table 3.1. Critical-curve Topology Occurrence in Triple-lens Models

Model										
LS	B	-	-	A	-	C,E	-	-	D,F	
LA	D	B	-	C	-	E	A	-	F	
TE	C	B	D	A	-	E,H	-	I,J	F,G	
TI	G	C	F	D	B	E,J	A	I,L	H,K	

Note. — Topology regions of the model parameter spaces are marked by letters, as defined in Figure 3.2 for the LS model, Figure 3.8 for the LA model, Figure 3.11 for the TE model, and Figure 3.15 for the TI model.

region; the $16/6+4+3+3$ caustic in the TI model A region vs. the TE model J region and TI model L region; and the $18/8+4+3+3$ caustic in the TI model A region vs. the TE model J region and TI model L region.

The list in Table 3.2 does not include the caustics of lens configurations at metamorphosis points. The classification along subregion boundaries in parameter space would require additional counting of beak-to-beak, swallow-tail, and butterfly points. Even here we note that the caustic structures of the analyzed models are only examples of triple-lens caustics, and the list in Table 3.2 is not exhaustive. Analyzing less symmetric systems reveals that the frequency of metamorphosis types is different from most of the analyzed models, with swallow tails occurring more frequently than butterflies (as seen here in the LA model).

Table 3.2. Caustic Structure Occurrence in Triple-lens Models

Cusps Total/By Loop	Triple-lens Model Parameter-space Subregions [Sample Parameter Combination]			
	LS [μ, d]	LA [p, d]	TE [μ, d]	TI [$\theta/\pi, d$]
8/8	B ₁ [0.2,0.8]	D ₁ [0.45,1.2]	...	G ₁ [0.95,1.5]
10/10	C ₁ [0.6,1.35]	G ₂ [0.7,1.2]
10/6+4	...	B ₁ [0.3,1.5]	B ₁ [0.05,1.5]	C ₁ [0.1,3]
12/12	B ₂ [0.2,0.5]	D ₂ [0.45,0.7]	C ₃ [0.95,0.95]	G ₄ [0.95,0.8]
12/9+3	D ₁ [0.33,1.2]	F ₁ [0.33,1]
12/6+6	B ₂ [0.13,1.73],B ₅ [0.05,1.13]	...
12/6+3+3	C ₁ [0.04,0.5]	E ₁ [0.35,0.65]	...	E ₁ [0.05,1]
12/5+4+3	B ₁ [0.08,2.38]
12/4+4+4	A ₁ [0.25,1.75],E ₃ [0.09,0.36]	C ₁ [0.45,1.95]	A ₁ [0.25,3]	D ₁ [0.3,3],D ₃ [0.9,3]
14/14	C ₂ [0.6,0.95]	G ₃ [0.4,1.3]
14/10+4	B ₄ [0.09,1.58]	C ₂ [0.2,2]
14/8+3+3	E ₂ [0.7,0.7],H ₁ [0.05,0.69]	E ₂ [0.15,1],J ₂ [0.7,0.55]
14/7+4+3	B ₃ [0.11,1.83]
14/6+4+4	A ₂ [0.6,2],A ₃ [0.25,2.1]	D ₂ [0.5,2.5],D ₅ [0.32,2.5]
14/4+4+3+3	...	A ₁ [0.1,1.5]	J ₇ [0.768,0.14]	A ₁ [0.01,2.1],A ₄ [0.05,3.1],L ₇ [0.7,0.34]
16/16	B ₃ [0.04,0.6]
16/10+6	B ₃ [0.25,1.45]	C ₃ [0.25,1.6]
16/10+3+3	...	E ₂ [0.35,0.75]	E ₁ [0.85,0.7]	J ₃ [0.84,0.55]
16/9+4+3	B ₂ [0.1,1.98]
16/8+4+4	A ₂ [0.95,1.45]	...	A ₅ [0.995,1.1]	...
16/7+3+3+3	I ₁ [0.6,0.67]	I ₁ [0.5,0.6]
16/6+6+4	E ₁ [0.15,0.36]	D ₄ [0.25,2.3]
16/6+4+3+3	J ₃ [0.77,0.6],J ₆ [0.772,0.158]	A ₂ [0.05,2.1],L ₄ [0.7,0.4],L ₆ [0.76,0.39]
16/4+3+3+3+3	D ₂ [0.7,0.4],F ₁ [0.04,0.36]	F ₂ [0.5,0.45]	F ₃ [0.95,0.15],G ₁ [0.05,0.34],G ₃ [0.6,0.1]	H ₁ [0.1,0.5],H ₃ [0.65,0.2],K ₃ [0.85,0.25]
18/12+3+3	E ₃ [0.69,0.67]	J ₁ [0.62,0.52]

Table 3.2 (cont'd)

Cusps Total/By Loop	Triple-lens Model Parameter-space Subregions [Sample Parameter Combination]			
	LS [μ, d]	LA [p, d]	TE [μ, d]	TI [$\theta/\pi, d$]
18/8+4+3+3	J ₅ [0.773,0.16],J ₈ [0.764,0.155]	A ₃ [0.08,2.24],L ₅ [0.77,0.37],L ₈ [0.67,0.33]
18/6+6+6	A ₄ [0.3,1.7]	D ₆ [0.33,2]
18/6+6+3+3	J ₁ [0.8,0.45]	L ₁ [0.78,0.44]
18/6+3+3+3+3	F ₂ [0.95,0.35],G ₂ [0.25,0.6]	H ₂ [0.33,0.5],K ₂ [0.88,0.48]
20/8+8+4	E ₂ [0.15,0.34],E ₄ [0.09,0.29]
20/8+6+3+3	J ₂ [0.8,0.4],J ₄ [0.7,0.6]	L ₂ [0.81,0.44],L ₃ [0.66,0.36]
20/8+3+3+3+3	D ₁ [0.7,0.65]	F ₁ [0.5,0.53]	F ₁ [0.99,0.85]	K ₁ [0.94,0.52]

Note. — Caustic-structure subregions of the model parameter spaces are marked by letters and numerals. The sample parameter combinations in square brackets identify their position in Figures 3.2 and 3.5.2 for the LS model, Figure 3.8 for the LA model, Figures 3.11 and 3.12 for the TE model, and Figures 3.15 and 3.16 for the TI model.

3.6 Summary

Our approach is based on analyzing the properties of the lens in the image plane, with the main relevant results from (21) introduced in § 2.2. We describe in detail in § 3.3 and § 3.4 several analytical and numerical methods for parameter-space mapping of the topology of the critical curve and the number of cusps of the caustic. The methods are presented in a form applicable to any n -point-mass lens.

In § 3.5.1 we present the main relevant polynomial equations for triple lenses in a compact form in terms of moments of the mass distribution. In the following § 3.5.2 – § 3.5.5 we apply the described methods to the analysis of four simple two-parameter models of triple lenses. For each of them in turn we discuss separately the Jacobian surface character, topology boundaries, critical-curve topologies, caustic structure, Jacobian contour plots, planetary limits, close limit, and wide limit. The combined results explain the properties of lenses on four 2D cuts through the full 5D parameter space of the general triple lens. Since each of the studied models intersects at least one other along a 1D set of parameter combinations, the presented results may serve as a reference framework for further studies.

The results include the description of a range of triple-lens features, such as the occurrence of swallow-tail and butterfly metamorphoses, Jacobian monkey saddles, or double maxima. We demonstrated that the appearance of two new cusps in the beak-to-beak metamorphosis is not always accompanied by the splitting of critical-curve loops. It may lead to the opposite, the merger of loops, as discussed in the caustic structure paragraphs of § 3.5.2. Finally, two simultaneous beak-to-beaks may lead to a reconnection preserving the number of loops. Within the studied models this occurs along the D-B transition in the TE model, and along the F-C transition in the TI model.

The planetary limits are particularly noteworthy in the equilateral TE model. The $\mu \rightarrow 0$ limit shows that a planet placed near the close – intermediate beak-to-beak point of a binary lens may turn the single transition into a sequence of six caustic metamorphoses. The $\mu \rightarrow 1$ limit demonstrates that a pair of planets may form additional cusps on the Chang-Refsdal four-cusped caustic of the star at a very broad range of separations, in this case $s \in (0.214, 4.66)$ Einstein radii.

Unusual behavior in the close limit occurs in the presence of double maxima (LS, TE, and TI models), and in the equal-mass equilateral lens (TE and TI models). Any double maximum causes the lens to have a four-cusped escaping caustic loop instead of a pair of three-cusped loops (14). The symmetry of the equal-mass equilateral lens causes it to have a self-intersecting six-cusped (asymptotically three-cusped) primary caustic loop, instead of the generic four-cusped loop. In addition, one of the weak three-cusped caustics stays at the origin instead of escaping away.

Very interesting wide-limit behavior was found in the TI model with vertex angle $\theta = \pi/2$. Here one of the caustic loops retains a self-intersecting six-cusped shape approaching a three-cusped shape for arbitrarily large separations of all components. Such a lens violates the generic Chang-Refsdal limit (16). In this case the gravitational fields of the two other components exactly combine to cancel the lensing shear term. The shape is thus dominated by higher-order

terms, leading to its different geometry.

For smaller angles, the wide limit of the TI model demonstrates the sensitivity of the binary caustic structure of the two close components to a distant companion. Here the presence of the third perpendicularly offset body perturbs primarily the caustic structure near the close – intermediate transition. As a result, the caustic undergoes a sequence of five metamorphoses instead of a single one.

We compiled the results found for all four models in the tables presented in § 3.5.6. The critical curves have 9 different topologies, and the caustics have 32 different structures, when identified by the combination of numbers of cusps on individual loops. A joint classification of critical-curve topologies and caustic structures increases the number further to 37 different situations. The lists are just a sample of the full range provided by the general triple lens.

In Table 3.2 we provided for each model the parameters of examples of all different caustic structures. These can be used to guide more detailed studies of critical-curve and caustic metamorphoses, to generate examples for testing light-curve fitting codes and algorithms, or as a starting point for exploring the behavior of less symmetric triple lenses.

4. Mapping critical-curve topologies of triple lens with fixed fractional masses

4.1 Parameters-space visualization

Even if it is possible to use Jacobian-contour correspondence (see section 3.3.4) to find critical-curve topology transitions for any n -point mass lens, it is rather intricate to visualize a parameter space of more than two dimensions. For three-dimensional models we may use a series of two-dimensional cuts. In this chapter, we discuss the dependence of critical-curve topology on lens positions only. Relative positions of three points can be described by the properties of a triangle with vertices in lens positions. Since we are using Jacobian-contour correspondence to determine topology changes, it is convenient to use a parameter describing size of the system and two other parameters to describe shape of the triangle. For scale we chose perimeter of the triangle p .

The most intuitive characterization of the shape of the triangle would be the use of two angles of the triangle. Unfortunately, such a parametrization of shape-space fails to characterize collinear configurations of triple lens as any collinear configuration correspond to one set of angles $0, 0, \pi$.

Our choice is a parametrization using length of sides a, b, c relative to the scale perimeter p , so that $\alpha = a/p, \beta = b/p, \gamma = c/p$.

In order to retain all symmetry of the problem, we use ternary plot to depict the shape-space. The ternary plot is a plot of three variables α, β, γ with a constant sum $\alpha + \beta + \gamma = 1$. Every point of the ternary plot unambiguously determines the shape of the lens configuration as is shown in Figure 4.1, e.g., the centroid of the plot corresponds to a triple lens with the shape of an equilateral triangle, the points along the medians of the ternary plot correspond to the isosceles-triangle configuration of the triple lens, points on the sides correspond to collinear configuration and vertices correspond to degenerate triple lens with two lens points overlapping. The whole parameter space of a triple lens with fixed masses can be visualized by a sequence of ternary plots of different values of perimeter.

Our numerical search for topology changes in parameter space uses a 1000×1000 grid in (α, β) coordinates with boundary $\frac{1}{2} \leq \alpha + \beta \leq 1$. For each grid point, we determine six values of perimeter where the critical-curve topology changes as per Jacobian-contour correspondence (see Section 3.3.4). We then assume that the values of the perimeter form six smooth surfaces in (α, β, p) . In order to obtain the surfaces as functions $p(\alpha, \beta)$, we identify the six perimeter values for each pixel with the six surfaces. The identification is based on requirement that the sum of the second derivatives of p with respect to α or β for each surface is minimized. The surfaces are then represented by a $1000 \times 1000 \times 6$ matrix of permutations of perimeter values for each grid point. Unfortunately, the assumption that the critical-curve topology transitions form six separate surfaces is not valid; rather there is a lower number of self-intersecting surfaces. For that reason, the resulting

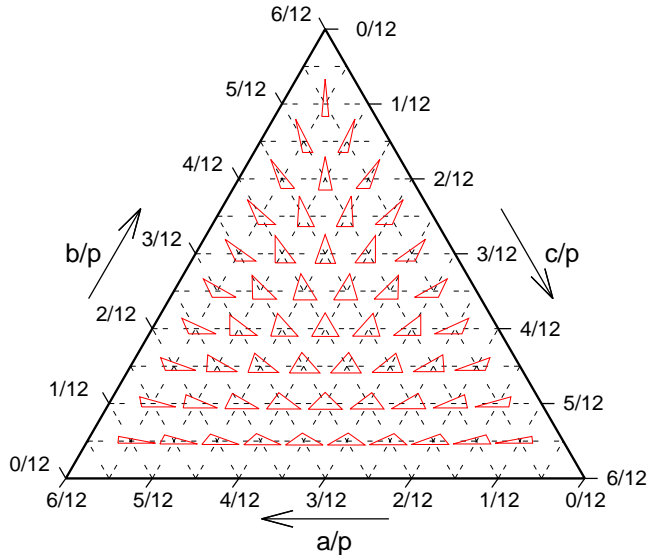


Figure 4.1 Ternary plot: Red triangles for for shapes of triple-lens configurations corresponding to point in centroid of the triangles.

permutations are ambiguous and depend on the path the sorting algorithm has undertaken in (α, β) space.

Then we introduce a grid in perimeter and for each value of perimeter on the grid we identify different topology regions using a 6-way flood-fill algorithm. The flood-filling algorithm both integrates the volume and checks for changes in perimeter permutation to avoid flooding of additional regions. After the routine is finished with given perimeter section, it identifies filled regions with those from previous perimeter section.

4.2 Probability of topology occurrence

The main drawback of using the scale-less lengths of sides on ternary plot is that it may offer a limited intuition frequency of the occurrence of different critical-curve topologies.

To give the reader some measure of relevance of different topologies we find, for each topology region, corresponding volumes in lens-component position space z_i for $i = 1, 2, 3$. The volumes can be used in the following way to obtain probabilities: if we have three lens components each with homogeneous probability distribution in some region of the lens plane, what is the probability that they will be located in given region of (α, β, p) space. We define Probability of topology occurrence for fixed perimeter as probability for a critical-curve to have a given topology if the lens components are positioned, in the lens plane, randomly with constraint that their perimeter is fixed. Similarly, we define Probability of topology occurrence for perimeter interval as probability for a critical-curve to have a given topology if the lens component have random position in the lens plane and perimeter lies in range $(0, p)$.

The actual integration is done in (α, β, p) space. For that reason we need to add weight function given by determinant of Jacobian matrix of transformation

from Cartesian lens coordinates $(\text{Re}(z_1), \text{Im}(z_1), \text{Re}(z_2), \text{Im}(z_2), \text{Re}(z_3), \text{Im}(z_3))$ to $\text{Re}(C), \text{Im}(C), \psi, \alpha, \beta, p$, where C stands for the geometrical center of the lens coordinates and θ is the phase of $z_2 - z_1$. In such a parametrization the determinant has the following form:

$$\frac{2\alpha\beta\gamma p^3}{\sqrt{(1-2\alpha)(1-2\beta)(1-2\gamma)}} \quad (4.1)$$

where $\gamma = 1 - \alpha - \beta$. The weight is independent of both C and ψ and we will ignore these in the integration as we are not interested in shifts and rotations of the whole coordinate system either in lens plane and in (α, β, p) space.

Recalling Heron's formula, the denominator equals four times the area of the triangle of the same shape and unit perimeter. The Jacobian determinant has a minimum at the centroid of the ternary plot and diverges at sides of the parameter triangle except for vertices. In a vertex, the limit of the Jacobian determinant depends on the direction we approach a vertex, e. g., limit $\gamma \rightarrow 0$ along either $\alpha = 1/2$ or $\beta = 1/2$ axes is infinite while has a finite value when approaching the vertex under different angle.

The weight given by equation (4.1) is proportional to the third power of the perimeter p . This reflects the fact that by increasing the separations of lenses the volume in z_i -space also increases.

The probabilities of observing microlensing event by the triple lens system with particular triple-lens topology might have completely different dependence on perimeter p . It is beyond the scope of this work to discuss actual probabilities of detection or even actual frequency of tree-point-mass lens systems based on further physical considerations.

4.3 Equal-mass model

The first model to discuss here is a triple lens with equal masses in an arbitrary position. Such a model has a full set of symmetries of ternary plot, i. e., symmetry to all permutations of lenses.

The equal-mass triple lens model can stand for triple-star system and it can serve as a fitting illustration of the method of the critical-curve topology analysis.

The three-dimensional parameter space of this model include parameter spaces of models discussed in Chapter 3. Those are equal-mass models LA model and TI model (see Sections 3.5.3 and Section 3.5.5). Parameter space of LA model corresponds to each of the slides of (vertically) stacked ternary plots. The perimeter p of the three-parameter model is equal to four separation parameters s of LA model $p = 4s$. The positioning parameter of the LA model p_{LA} relates to the ternary-plot side $\alpha = 1/2 p_{LA} = 2\beta = 1 - 2\gamma$ or $1 - p_{LA} = 2\beta = 1 - 2\gamma$. The TI model corresponds to each of the planes going perpendicularly through the median of the stacked ternary plots. The perimeter for the TI model is given by $p = 2s(1 + \sin(\frac{\theta}{2}))$ and the distance from $\gamma = 0$ vertex along $\alpha = \beta$ median relates to the angle between isosceles by $\sin(\frac{\theta}{2}) = \gamma/(1 - \gamma)$.

Other two-parametric models of Chapter 3 are not fully covered by the three-parametric model as they have one fractional mass as variable. The middle point of each side of perimeter section correspond to $\mu = \frac{1}{3}$ of LS model. The centroids of ternary plots correspond to TE model with $\mu = \frac{1}{3}$.

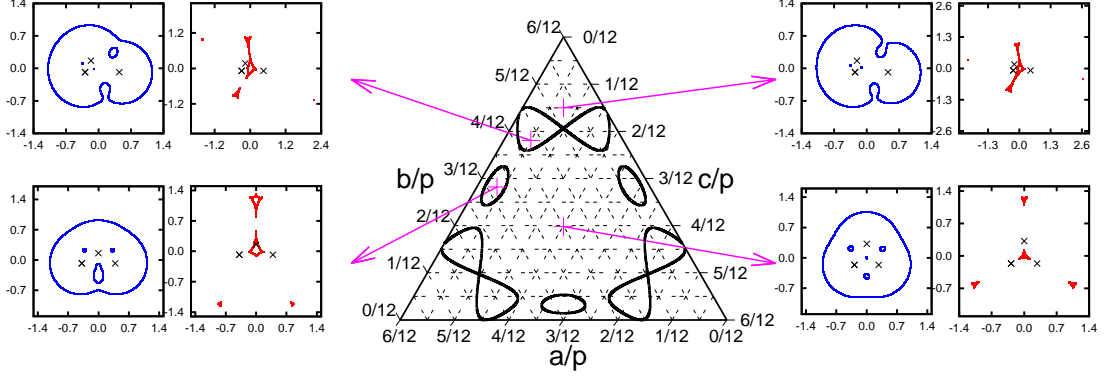


Figure 4.2 Equal-mass model: Perimeter section $p = 1.68$ with samples of critical curves and caustics. Central panel: ternary plot of the section. Black curves for topology boundaries. Purple arrows connect points in parameter space and sample critical curves and caustics. Panels on sides critical curves (blue) and caustics (red). Black crosses for lens positions.

In Figure 4.2 a single perimeter section $p = 1.68$ of parameter space of Equal mass model is shown. The section is plotted in ternary plot with curves corresponding to the transitions between critical-curve topologies. Along with the perimeter space section, there are examples of critical curves and caustics corresponding to four types of critical-curve topology regions that do not project on each other under a permutation of the lenses. There are three critical-curve topologies in thirteen topology regions.

To complete a topology analysis of the triple-lens model, we have to determine topologies of regions in (α, β, p) space, i. e., to determine a topology of each region of (α, β) space for each constant- p section of constant p .

Using the method described in section 4.1, we obtained 39 topology regions. Due to the symmetry, only 13 of the topology regions correspond to different lens geometries yielding only 9 topologies in total.

In the Figure 4.3, we plotted a sequence of ternary plots for different-perimeter sections of the parameter space. In the low perimeter limit, there are two topologies present. Critical curve in the first topology consists of one outer loop and four nested loops around Jacobian maxima. Critical curve of the second topology has one pair of the nested loops merged into one as lens configuration approaches special lens positions leading to a double Jacobian maxima. The third critical-curve topology appears for $p = 2(\sqrt[3]{1/3} + \sqrt[3]{2/3})^{-3/4} \approx 1.43$ at vertices of the ternary plot. At that point, a pair of the nested loops is merged with the non-nested loop. At $p = 1.5$, we have the first example of the perimeter cut present in Figure 4.3. In this cut, new figure-8-shaped regions with the second topology are present. Those lie along the border between mentioned regions of the first and third topology and represent configurations without axial symmetry, i. e., are not of isosceles triangle configuration. At $p \approx 1.861$, the first topology is no longer present and for higher perimeters more regions appear and disappear.

Eventually, asymptotic regime is reached at $p \approx 6.71$ where four topologies are present. Critical curves of the four asymptotic topologies can be understood as a combination of single lens and two-point-mass lens topologies, i. e., one isolated

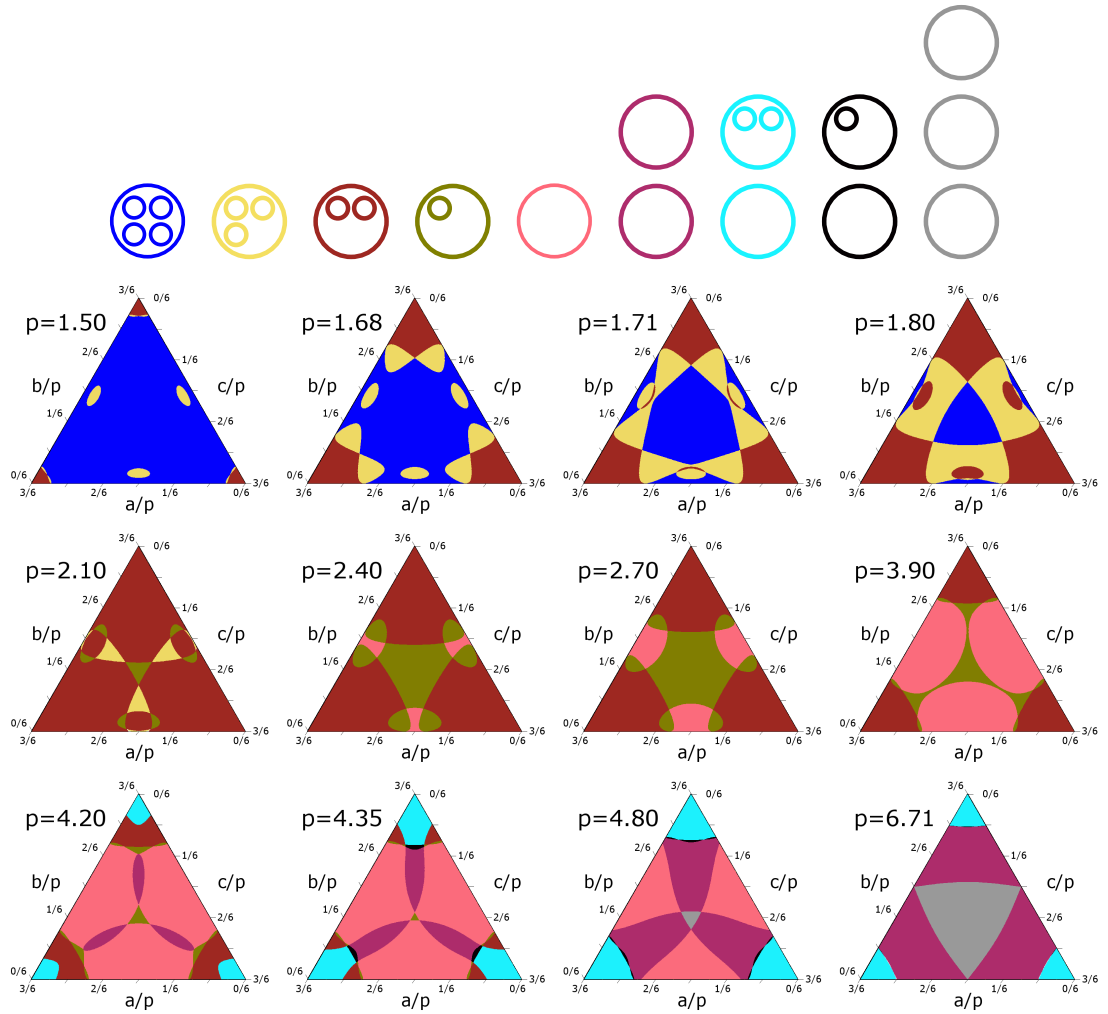











Figure 4.3 Equal-mass model: Sequence of perimeter sections through parameter space. Top row: sketches of topologies in order of appearance. Color-coding of the sketches correspond to critical-curve topologies in the sections.

critical curve loop plus one to three loops resembling close, resonant or wide critical curve of two-point-mass lens. There is a topology of three non-nested loops at the centroid of the ternary plot. This topology can be understood as three single lenses, or a single lens and a wide binary lens. Then moving in the direction of a ternary-plot vertex, i. e., decreasing one separation while increasing the two other separations, we enter a region corresponding to two critical-curve loops obtained by merging the two of critical-curve loops analogous to a single lens and binary lens in resonant topology. Finally, we enter regions with topologies similar to single plus close type binary topology or perturbed close binary topology. By perturbed close binary topology we mean two outer loops with one nested loop.

We obtained the probabilities of topology occurrence by integrating weight function (4.1) on regular rectangular grid. The domain of integration over perimeter is $p \in (0, 6.71)$. We summarized the result in Table 4.1. Close-type topologies are highly disfavored due to the fact that weight function given by equation (4.1) is proportional to the third power of the perimeter. Since we cut-off the integration when the asymptotic $p \rightarrow \infty$ regime is reached, the $T1$, $T2$, $T3$ and $T4$ topology regions have finite volume. The most disfavored of these is topology

Table 4.1. Equal-mass model: Probability of topology occurrence

Topology Label	Topology Schema	Volume
T1		$(7.99 \pm 0.12) \times 10^{-2}$
T2		$(4.88 \pm 0.02) \times 10^{-1}$
T3		$(3.42 \pm 0.56) \times 10^{-3}$
T4		$(1.25 \pm 0.01) \times 10^{-1}$
T5		$(2.09 \pm 0.01) \times 10^{-1}$
T6		$(2.12 \pm 0.05) \times 10^{-2}$
T7		$(6.48 \pm 0.03) \times 10^{-2}$
T8		$(1.49 \pm 0.03) \times 10^{-3}$
T9		$(4.10 \pm 0.03) \times 10^{-3}$

T3. Uncertainties of the probabilities are mostly given by discretization in α, β plane and inability of the algorithm to determine exact positions of borders of the regions. In total 0.05% of pixels were not identified with any topology region leaving probability of 0.01% not attributed to any topology. The probability corresponding to noncharacterized pixels poses upper bound on the maximum probability of occurrence of topology that could have been missed in our analysis. The range of error of the probabilities is given by probability corresponding to points on the surface of all the regions of the same topology.

In order to give a more complete view of the shapes of the topology regions, we depicted in Figure 4.4 perimeter dependence of the probability of occurrence for fixed perimeter. Topologies are presented in order of appearance in sequence of plots from low perimeter asymptotic topology *T9* regions at the top panel to high perimeter asymptotic topology *T1* at the bottom panel. Range of perimeters is cut off at $p = 6.71$ when the asymptotic regime is reached. At that perimeter, section *T2* still dominates, while at $p \rightarrow \infty$ limit *T1* is the only one that does not go to zero. Of all topologies only *T5* covers more than a half of integrated interval, while *T8* covers the shortest interval and is concentrated in a rather sharp peak.

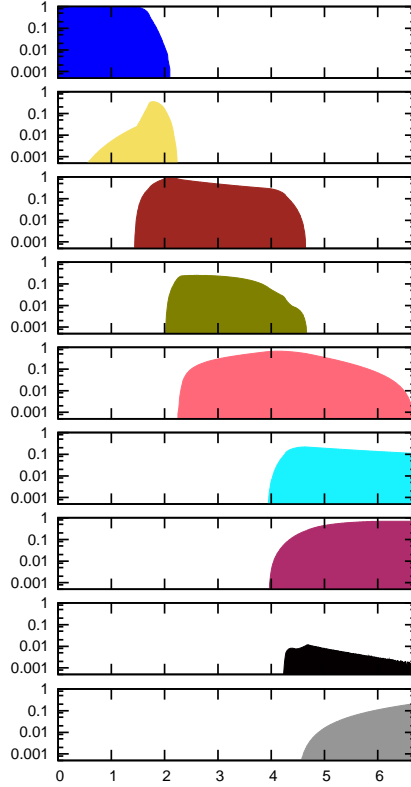


Figure 4.4 Equal-mass model: Perimeter vs. probability of topology occurrence for fixed perimeter. Topologies from top to bottom T_9 , T_8 , T_7 , T_6 , T_5 , T_2 , T_4 , T_3 , T_1 . Color-coding correspond to Figure 4.3.

4.4 Planet-in-binary model

By the Planet-in-binary system we mean triple lens consisting of three lenses with fractional masses $\mu_1 = \mu_2 = 0.49995$, $\mu_3 = 0.0001$.

With the introduction of unequal masses we lose symmetry. Having two equal masses for stars we still have reflection symmetry along one of the medians, i.e., the stars have the same mass and are thus interchangeable.

Combination of masses of this model can represent a planet orbiting one of the stars in the binary star system or circumbinary planet or any intermediate configurations.

The parameter space of the model has no overlap with equal-mass models of Chapter 3 and remaining models TE and LS models have only 1D intersection. The intersection of Planet-in-binary model and LS model is represented by a line through the center of $a/p = 1/2$ side in Planet-in-binary model and $\mu = 0.0001$ of LS model.

The multitude of critical-curve topologies of the Planet-in-binary system can be understood easily as a perturbation to the binary lens due to the planet. A perturbation to a n -point-mass lens by a lensing point results in one additional pole, two maxima and three saddle points to a lens-equation Jacobian. For infinitesimal mass of the additional lens point, all the additional extrema of Jacobian surface shrink to a small region around the lensing point position. Thus, the simplest critical-curve behavior of the planet-like perturbation of n -star mi-

croLens is of the following types: (a) if the planet is placed in a region of positive n -point lens Jacobian, the critical curve has one extra loop around the planet; (b) if the planet is placed in a region of negative n -point lens Jacobian, the critical curve has two additional loops around two $(n + 1)$ -point lens Jacobian maxima in the vicinity of the planet. The situation becomes more complicated if the planet is placed close to n -point lens critical curve. Additional planet can also change parameters of n -point lens critical-curve topology transitions as will be discussed below.

Sequence of ternary plots along with summary of topology sketches are plotted in Figure 4.5. The sequence goes in direction of rising perimeter from top left to bottom right. At perimeter $p = 1.02$ only those regions are present that are also present in limit $p \rightarrow 0$ and at perimeter $p = 5.64$ asymptotic regime $p \rightarrow \infty$ is reached.

By comparison of Figure 4.5 to Figure 4.3 we can see the same generic behavior of the regions in both asymptotic regimes. In $p \rightarrow 0$ we have $T9$ close topology combined with $T8$ around three point where lens-equation Jacobian has double maxima. For $p \rightarrow \infty$ asymptotic we again have $T1$ topology from which going along a line in direction of any vertex we cross $T2$, then $T3$ and, finally, we reach $T4$. We used dashed line for the sketch of $T10$ topology as it is too small to be clearly visible in the ternary plot.

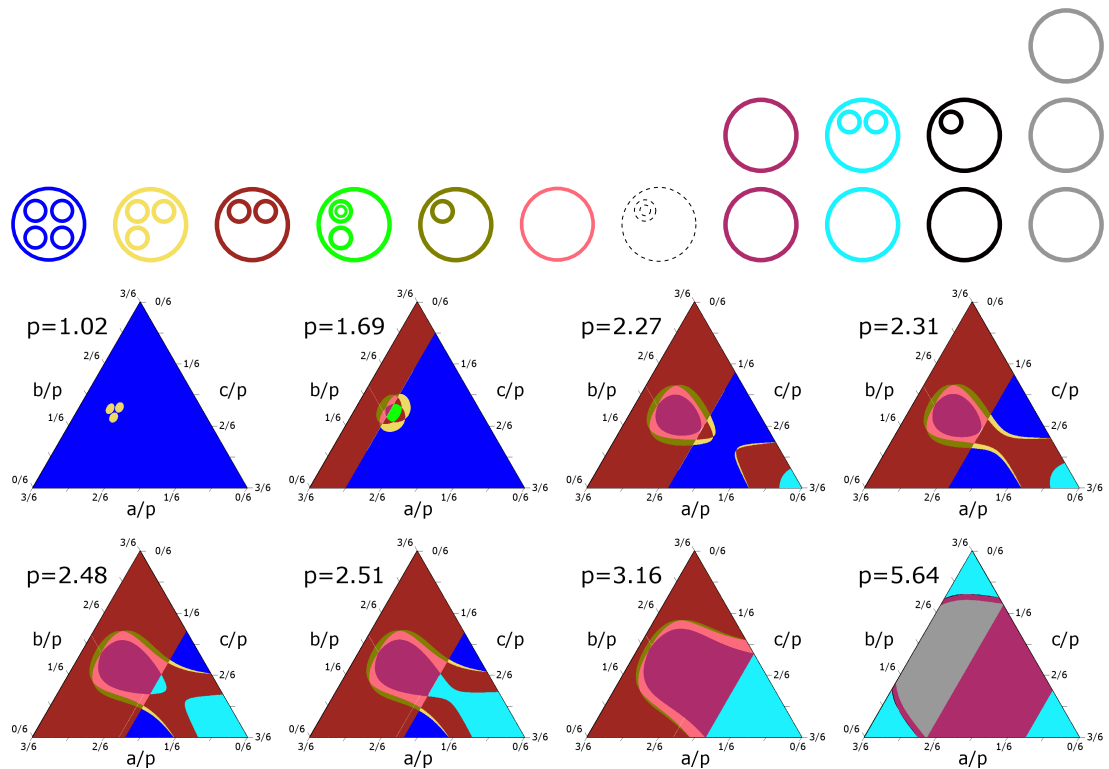


Figure 4.5 Planet-in-binary triple lens model: Sequence of perimeter sections through parameter space. Top row: sketches of topologies in order of appearance. Topologies of the regions and the sketches correspond by color-coding.

Although we have similar behavior of asymptotic regimes of both Equal-mass and Planet-in-binary triple-lens models, other topology regions are deformed be-












yond recognition and disallow identification with topology regions of Equal mass model. Also, new regions emerge. Some of the topology-region border seem to form a straight line perpendicular to the axis of symmetry of the model. This means that the topology changes for some value of the star-star separation no matter what the position of the planet is. A finer grid can reveal several thin topology regions along the border. This is to be expected if the linear border represents simultaneous merging of several critical-curve loops, e.g. a transition between close and resonant topology of binary lens critical curve. The planet then acts as perturbation to the binary lens that in effect causes loss of symmetry and the transition to occur for different values of the parameters. Thus instead of one borderline representing several simultaneous critical-curve transition we have several narrow regions representing topologies that underwent only some of the topology changes. This type of regions are present even in Equal-mass model, e.g. in instances of $T3$ topologies in $p \rightarrow \infty$ asymptotic regime and $T8$ in $p \rightarrow 0$ asymptotic regime. Unfortunately, in the case of the Planet-in-binary model, these regions get too thin to be analyzed easily.

There are two new topologies, $T10$ and $T11$, in the Planet-in-binary model. The $T11$ topology can be constructed as a small-mass perturbation by lensing point put in nested loop of binary close type critical-curve topology. Such a topology has an additional, twice nested, critical-curve loop inside the nested loop of binary critical curve. In case of topology $T10$, the planetary perturbation in addition to $T11$ disturbs one binary transition so that resulting topology consists of one loop, one nested loop and one doubly nested loop. While $T11$ topology correspond to substantial topology region depicted in perimeter section $p = 1.69$ of Figure 4.5, $T10$ is shrunk along linear border between $T11$ region and $T2$ region.

Our inquiry cannot yet determine conditions for the planet to be detected in binary star system. Nevertheless, it is quite natural to assume that for a planet to be detected in binary star system, strong disruption of a binary star caustic is needed. Such a disruption can occur when the planet is positioned close to the critical curve of the binary system. Topologies that necessarily have planetary and binary critical-curve loops merged are: $T8$, $T5$, $T6$. On the other hand, there are topologies whose planetary and binary loops cannot be merged in topologies $T1$, $T9$, $T10$, $T11$. Topologies $T11$ and $T10$ require the planet to be positioned in vicinity of nested binary loop and thus are expected to distort corresponding caustic loop. Regions of parameter space, where the topology is sensitive to planetary position starts from $T8$ regions of configurations with double Jacobian maxima at $p \rightarrow 0$ limit. Then going in direction of rising perimeter, the $T7$ regions overlap resulting in $T6$ and $T11$ regions. Those correspond to various interaction between planetary loops and binary nested loops. After that are planetary-sensitive regions shrunk along circumference of $T2$ region as is seen from perimeter cuts $p = 2.27$, $p = 2.31$, $p = 2.48$, $p = 2.51$, $p = 3.16$ of Figure 4.5. These narrow regions represent interaction of planetary loops and the binary loop of resonant topology. Finally, the planet can be positioned on the binary critical curve loop of the wide topology resulting in topologies $T2$, $T3$ and $T4$ at the off-axis vertices at perimeters $p = 4.35$, $p = 5.64$.

In Table 4.2 probabilities corresponding to the topology regions are listed. The domain of integration over perimeter is $p \in (0.0, 5.64)$. Of all pixels of all

Table 4.2. Planet-in-binary model: Probability of topology occurrence

Topology Label	Topology Sketch	Probability of occurrence
T1		$(1.38 \pm 0.01) \times 10^{-1}$
T2		$(4.54 \pm 0.02) \times 10^{-1}$
T3		$(2.57 \pm 0.56) \times 10^{-3}$
T4		$(2.18 \pm 0.01) \times 10^{-1}$
T5		$(2.95 \pm 0.10) \times 10^{-2}$
T6		$(6.64 \pm 0.08) \times 10^{-3}$
T7		$(1.32 \pm 0.01) \times 10^{-1}$
T8		$(3.88 \pm 0.39) \times 10^{-4}$
T9		$(1.87 \pm 0.005) \times 10^{-2}$
T10		$< 3 \times 10^{-6}$
T11		$(3.08 \pm 0.12) \times 10^{-5}$

perimeter sections only 0.03% were not identified with any topology region leaving 0.04% of probability of occurrence not attributed to any topology. The unidentified pixels resulted from rather complex topology regions evolution along linearized boundaries. Moreover, in the case of long thin regions, most of their volume may be attributed to the regions with different topology, since many pixels lie inside one region while they contribute to the integrated probability also with area that may be part of different region. The range of error of the probabilities is given by probability corresponding to the points on the surface of all the regions of the same topology. We determine upper bound for such a probability corresponding to unidentified long thin regions as probability of one-pixel breadth in s/p and height 5.64×10^{-3} around the linear boundaries. We approximate the boundaries by surfaces of constant d corresponding to topology transitions of equal-mass binary lens $\{s_{close}, s_{wide}\} = \{2^{-1/2}, 2\}$. For integration ranges of perimeter $(2 s_{close}, 5.64)$ and $(2 s_{wide}, 5.64)$ we obtain probability along pixel-thin slice along the linear boundaries to be 0.001%, i.e. the same order of magnitude as $T11$ topology region while one order of magnitude lower than portion of unidentified regions. Thus sub-pixel-thin regions do not present considerable addition to uncertainty already given by unidentified pixels.

Perimeter dependences of the the probabilities of given topology are plotted in Figure 4.6. Topologies are presented in order of appearance in sequence of plot from low perimeter asymptotic topology $T9$ regions at the top panel to high perimeter asymptotic topology $T1$ at the bottom panel. The range of perimeters is cut off at $p = 5.64$ when the asymptotic regime is reached. At that perimeter section $T2$ still dominates, while at $p \rightarrow \infty$ limit only $T1$ region does not go to zero. In comparison to Equal mass model, regions cover a broader interval.

Topology region T_{11} is concentrated only to small interval. Region of T_{10} was too small to be evaluated accurately so only an estimate of the range in perimeter is presented.

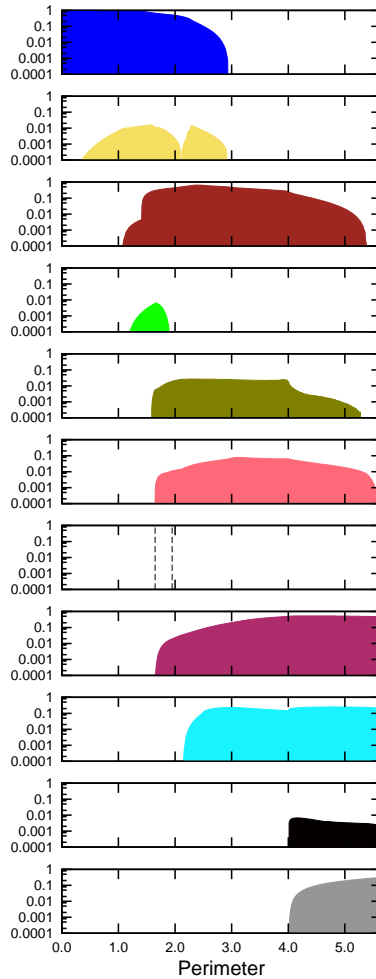


Figure 4.6 Planet-in-binary model: Perimeter vs. probability of topology occurrence for fixed perimeter. Topologies from top to bottom T_9 , T_8 , T_7 , T_{11} , T_6 , T_5 , T_{10} , T_2 , T_4 , T_3 , T_1 . Color-coding correspond to Figure 4.5.

4.5 Hierarchical-mass model

In this section we analyze fixed mass triple lens model of masses $q_1 = 1.0$, $q_2 = \mu_2/\mu_1 = 10^{-2}$, $q_3 = \mu_3/\mu_1 = 10^{-4}$. Such a system can represent a star with two planets, a star with a planet and a moon or a planet in a binary star system. We will refer to the lens components of fractional masses q_1 , q_2 , q_3 as to the star, planet and moon respectively.

This system does not retain any symmetry of the Equal mass system and we are using ternary plots only for the sake of comparison.

The parameter space of the model is disjoint to parameter spaces of other triple-lens models discussed previously.

Again, in the Hierarchical-mass system, it is possible to utilize the perturbative understanding of the critical curve. In this case the two low-mass lens components act as a perturbation to the Einstein ring of a single lens. Perturbation, again, cause two nested critical-curve loops, if we place the low-mass lens point well inside the Einstein ring; and one loop if the low-mass lens point is placed well outside the Einstein ring. When the two low-mass lens components are placed close enough, i.e. approximately closer than one tenth of Einstein radius, they can no longer be understood as two independent perturbations but their mutual interaction takes place. At the same time, the moon can act as a perturbation to star-planet system and topology $T11$ can be obtained in that way.

In Figure 4.7 we plotted a sequence of perimeter cuts. As with the Planet-in-binary model, we can see linear region boundaries.

In contrast to Planet-in-binary model, there are linear boundaries going along both constant a/p or b/p rather than a/p only. Model includes all topologies of Equal-mass and Planet-in-binary model while $T10$ occupies only small elongated region between regions of topologies $T11$ and $T2$.

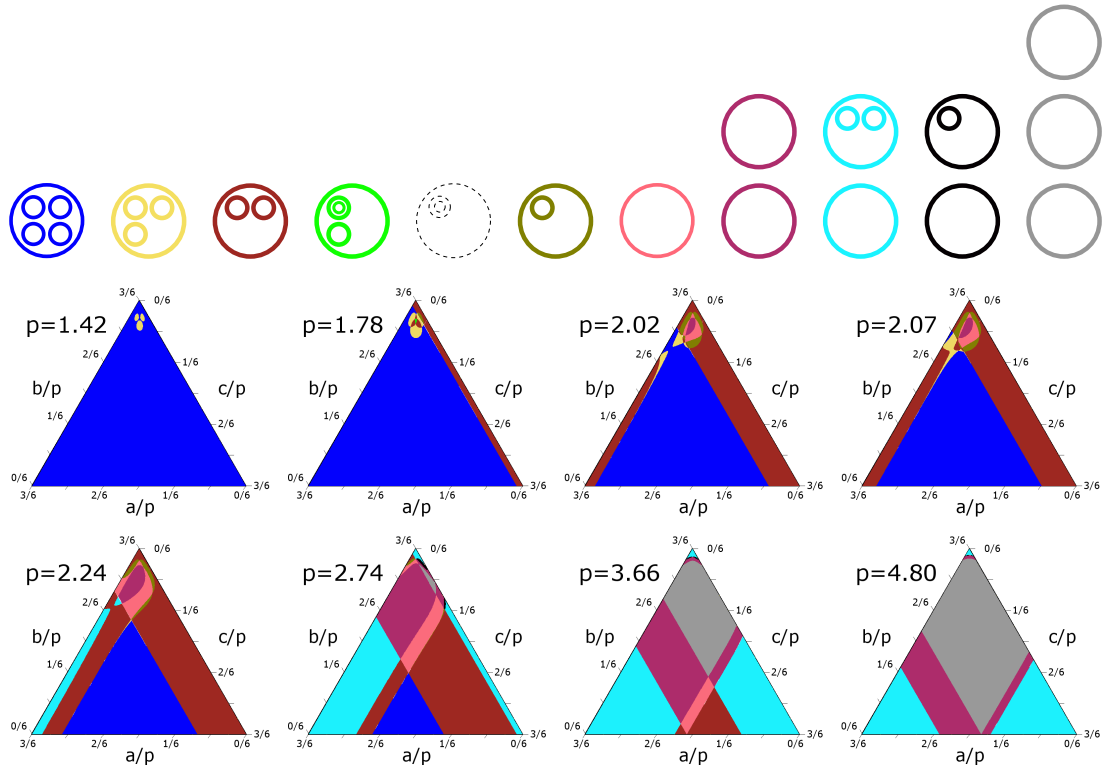
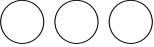







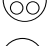
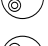



Figure 4.7 Hierarchical-mass model: Sequence of perimeter sections through parameter space. Top row for sketches of topologies in order of appearance. Color-coding of the sketches correspond to critical-curve topologies of the in the sections.

The sequence starts with four low-perimeter asymptotic regions: dominant region of topology $T9$ and three regions of topology $T8$ located close to the ternary-plot vertex corresponding to planet-moon approach. With increasing perimeter, the $T8$ regions overlap giving rise to $T7$ and $T11$ for pair or triple regions overlapping respectively. At $p = 1.78$ we can see all $T9, T8, T7$ and

Table 4.3. Hierarchical-mass model: Probability of topology occurrence

Topology Label	Topology Schema	Probability of occurrence
T1		$(2.59 \pm 0.01) \times 10^{-1}$
T2		$(2.01 \pm 0.02) \times 10^{-1}$
T3		$(7.69 \pm 1.68) \times 10^{-4}$
T4		$(3.79 \pm 0.02) \times 10^{-1}$
T5		$(1.67 \pm 0.04) \times 10^{-2}$
T6		$(1.09 \pm 0.09) \times 10^{-3}$
T7		$(8.76 \pm 0.06) \times 10^{-2}$
T8		$(2.39 \pm 0.16) \times 10^{-4}$
T9		$(5.52 \pm 0.02) \times 10^{-2}$
T10		$< 10^{-7}$
T11		$(1.66 \pm 0.23) \times 10^{-6}$

*T*11 regions with *T*7 and *T*6 regions emerging from linear boundary between *T*9 and *T*7 and between *T*8 and *T*6. The boundary itself represents a transition of planet-star critical curve from close to resonant type of topology while the exact planet-star separation of the transition is slightly influenced by moon position. The behavior that deviates from a simple combination of the two two-point-mass critical curves occurs mainly in the region of $c/p < 1/10$ where complex star-planet-moon interaction occurs. These deviations can occur for even bigger planet-moon separations as we can see in $p = 2.07$ ternary plot of Figure 4.7 where the *T*7 stretches beyond $c/p < 1/2$ due to the planet perturbation to moon-star close→resonant topology transitions. Finally, at $p = 4.80$ the asymptotic regime with several regions separated by linear boundaries and 8-figure-shaped *T*3 regions shrinks to $c/p \rightarrow 0$. We used hashed line for the sketch of the *T*10 topology as the corresponding regions is too small to be visible in the ternary plot.

The probabilities corresponding to each topology region are shown in Table 4.3. The integration was cut off at $p = 4.80$. Of all pixels included, 0.03% were not identified with any topology region leaving probability 0.03% not attributed to any topology. Again, the majority of unidentified pixels lie on linear borders. Pixel-wide region along the linear border estimate leads to 0.002% which is still one order of magnitude lower than probability due to unidentified pixels.

In Figure 4.8 we plotted the perimeter dependence of probability of occurrence for fixed perimeter. The probability corresponding to *T*10 region was omitted because of high error of its evaluation. The range of perimeters is cut off at $p = 4.80$ when the asymptotic regime is reached. At that perimeter section *T*1 still dominates the section's area. Regions of this models tend to be even more

evenly distributed in p than in the previous model. Low perimeter asymptotic regions of $T9$ stretch to regions where high p asymptotic regions are present.

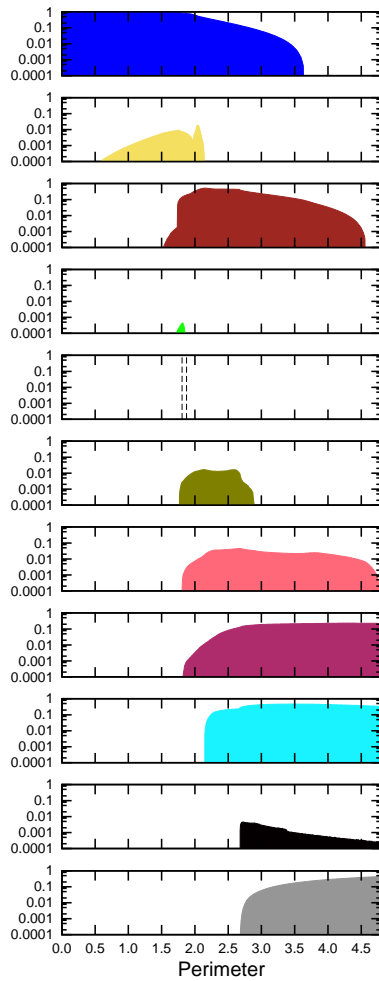


Figure 4.8 Hierarchical-mass model: Perimeter vs. probability of topology occurrence for fixed perimeter. Topologies from top to bottom $T9$, $T8$, $T7$, $T11$, $T10$, $T6$, $T5$, $T2$, $T4$, $T3$, $T1$. Color-coding correspond to Figure 4.7.

5. Light curves and amplification maps

Amplification map represents dependence of amplification on the source position in 2D region of the source plane. A linear cut through the map represents a light curve due to a straight trajectory of a source and a static configuration of the lens. For a the triple-lens configuration that changes in time a sequence of amplification maps is needed to obtain the light curve.

The caustics form the most distinctive features in amplification map. However, even the most profound knowledge of these curves is not sufficient for the understanding of the amplification map as a whole. Firstly, just looking at the caustic and given the source trajectory we can tell, when the caustic-crossing peak occurs on the light curve. But in the case of planetary microlensing the caustic-crossing manifests itself mostly as a short-time perturbation of Paczyński’s curve.

Secondly, there are not only peaks in amplification maps but also dips. One good example of a dip is in the star+planet system between the two triangular caustic loops corresponding to the close topology. Such a feature can be an indication of the presence of the planet but does not necessarily require a caustic crossing.

Thirdly, around the cusp there are lobes of increased amplification stretching far away from the caustic. In some cases, these lobes are far bigger than a caustic itself. In some cases of triple lens a small feature on the caustic is produced that consists of caustic self-intersection and cusps that are not clearly visible in the amplification map but the lobes disrupt the amplification map greatly.

Fourthly, some of the caustics can be “weak”, meaning that pace of the amplification decrease inside the caustic can be different for different caustics or even for different parts of one caustic. Basically, the weak caustic also produces divergences on the point-source light curve but the peaks will be very narrow with very fast drop to the amplification minimum. For an extended source, a caustic crossing of a weak caustic can produce very small peaks. Hence in an extended-source amplification pattern due to such a caustic might be insignificant.

Finally and most importantly, the pivotal topic of this thesis are topology changes of critical curves and changes in numbers of cusps. These qualitative changes do not necessarily imply great changes in amplification maps. For an extended the caustics are blurred and smoothed. Actually, due to extended source, it is quite difficult to tell whether two caustic loops of nearly merging topology are connected or disconnected just by looking at the amplification map while it is clear if we plot also the caustic. So we categorize discrete groups of caustics while the amplification pattern changes continuously with changes of lens parameters.

In case of lens systems composed of one star object and multiple planets, the resulting amplification further away from the star can often be successfully approximated by the superposition of amplification patterns of each planet+star system taken separately as two-point mass lens. This approximation was discussed by Han (36) and used in preliminary fitting of OGLE-2006-BLG-109L event (7). Thus in the case of similar systems that are in the center of interest of the contemporary planetary microlensing even amplification map of intricate

caustic can be understood by dividing it into several much simpler patterns. And that is another thing that we can learn from amplification map and not from caustic itself.

Studying amplification along with our topology analysis does not only bring our work closer to observers' needs but also helps us to understand the relevance of particular caustic behavior.

5.1 Summary of methods

The amplification of a point source can be obtained as a sum of absolute reciprocal values of Jacobian (given by equation 3.4) in image positions. To obtain the image positions the lens equation (1.4) must be inverted. As described in Chapter 2, the inversion has form of a polynomial. Not all its roots stand for true images because the inversion introduces spurious roots. The number of true images changes by two when source enters the caustic.

To produce more realistic light curves, the extended nature of a source has to be included. Most natural way would be to integrate amplification over source area using point-amplification (see equation 1.5). Unfortunately, the polynomial for the image positions of n -point-mass lens is of order $n^2 + 1$ and thus cannot be solved analytically for any but single lens. The fact that not all the roots of the polynomial stand for true images does not simplify the problem. The numerical polynomial solving is time-demanding so that the direct source integration is never used for evaluation of the extended-source light curve. Luckily, there are several other methods of the light-curve calculation to choose from.

Firstly, it is not necessary to invert the lens equation in order to evaluate the source amplification. Instead, we can substitute a test image position z into the lens equation (1.4) and see whether thus obtained source position ζ truly lies in the source disc. If it does, the test point z lies in a true image of the source. In this way, by shooting rays backward from the observer to the source plane, we can obtain total area of the images of the source and the total flux if we weight each point by the intensity profile of the source. This ray-tracing method became known as the Inverse Ray Shooting (IRS) and was first used in the context of gravitational lensing by Kayser et al. 1986 (44) for the study of quasar microlensing. There are two ways of obtaining light curve via IRS. By the first method, a large number of rays is shot at all points on the lens plane, chosen either on a grid or randomly. The pixel where the ray landed on the source plane is then registered and in this way whole amplification map of point source amplification is constructed. From the point-source amplification map the extended-source light curve is obtained by integration of the amplification map over the source area for each source position. Alternatively, some estimate of the image position is made for a given source position and then the rays are shot only to small area around the estimated positions.

Another class of methods avoid using Inverse Ray Shooting by application of Green's theorem. In this way the area of an image is calculated by integrating along the image boundary. The image contour itself is obtained by finding images of points on source boundary as roots of inverted lens equation. Producing the light curve in this way can be very fast compared to methods based on Inverse Ray Shooting since the IRS requires a huge number of rays to be shot to achieve

the sufficient accuracy. A drawback of contour-integration methods is that the amplification obtained from a single contour of a source is valid only for uniform brightness profile of the source. In order to take into account realistic brightness profile with limb darkening tens to hundreds contour integrations have to be calculated (15). This slows down the algorithm especially when the source is highly magnified; the Inverse Ray Shooting can include limb darkening cheaply by extra evaluation of brightness profile for each ray that hits the source.

When the source is far enough from the areas of high amplification like caustics' interiors and cusps' lobes, an approximation of amplification can be used. A method using the first two terms of amplification expansion was discussed by Pejcha & Heyrovsky (57) and Gould (30). For a brightness profile of circular symmetry the method requires five point-source evaluations or two point-source evaluation if points from previous steps are used.

5.2 Description of the code

The code we used is a version of inverse-ray-shooting method that uses roots of inverted lens equation (1.4) to estimate the image positions of the source center and proceeds by integrating over images. The idea was firstly implemented by Rhie & Bennett (8). As a method of sampling the image effectively a flood-fill routine was proposed by Vermaak (80). The routine was then described in detail and applied in study of extended source effect of binary lenses by Pejcha & Heyrovsky (57).

Our code is an alternative version of the code proposed by Pejcha & Heyrovský (57). Apart from the features included in algorithm of Pejcha & Heyrovský, a subdivision of image plane is introduced. Such a subdivision is needed to cover too small or thin images present in lensing of sources smaller than 10^{-2} . Such diminutive sources are not uncommon in planetary microlensing, e.g., OGLE-2006-BLG-109 (7) with the source size of $\rho \doteq 3 \times 10^{-4}$.

The algorithm undergoes following steps to determine extended source amplification:

1. For a given lens configuration the caustic is discretized as a set of polygons.
2. Intersections of source boundary with caustic are recorded. Since each overlap of the source area with inner region of some caustic loop can yield extra images, for each such part of the source area that overlaps with the caustic an inner source point is recorded.
3. For the center and for each point emerging from source-caustic overlaps images are found by inversion of equation (1.4). Those images become seeds for the flood-filling routine.
4. For each seed the flood-filling routine is started on a single big $10^4 \times 10^4$ grid in the image plane. The image-plane area covered by the grid is based on critical-curve size. The routine firstly checks if the position is visited for the first time and then IRS checks whether the point on the image plane correspond to a point in source area. If both conditions are satisfied the

point on the image plane makes a contribution to the amplification of the image based on the source brightness in the corresponding source point.

5. There are four possible results of flood-filling of an image on the big grid:
 - (a) No point on the image plane passes the test. This is either due to spurious results of inverted equation (1.4) or due to merged images, i. e., the point was already counted in as a part of another image.
 - (b) A single point on the image plane was evaluated. This means that at the point is a real image of the source, but the image is too small to be recorded on the grid. Therefore, some sub-grid has to be used. Amplification obtained from the flood fill on the big grid is not added to the total source amplification.
 - (c) Some small number of points on the image plane passes the test. Amplification obtained from the flood fill on big grid is not sufficiently accurate is not added to total amplification. Nevertheless, the filled area serves as an estimate of the image size for some further use of a finer grid.
 - (d) The flood-filled area is big enough to contribute to the total source amplification with sufficient accuracy. This can happen in three possible scenarios. Firstly, the image or a merged set of images is big enough to be evaluated accurately on $10^4 \times 10^4$ grid. Secondly, the image evaluation is not accurate enough but the grid size of a finer grid chosen by us would not yield sufficient increase in accuracy. Thirdly, the area is not sufficient for accurate amplification evaluation but is sufficient to indicate that the image is small enough and computational time should not be wasted on improving its accuracy.
6. If (b) or (c) occur, a finer grid is used. To do that, we use fixed size grid of the size of 2000×2000 . In the case (c) the finer grid covers a rectangular area given by coarse grid estimate. In the case (b) the square area of size 3×3 of coarse grid is chosen as an estimate for the image size. The image size estimates might be wrong so if flood-fill reaches the edge of the grid, it checks outside area. If valid image point is found outside the grid, the finer-grid flood-fill starts again on a bigger area.
7. Even for finer grid results can be (b),(c) or (d). In the case of (b) and (c) a further refinement of the grid is used.
8. It is possible that a coarse grid can overlook the merging of images. Thus finer-grid flood-fill can be used twice on one set of merged images and thus arrive to the higher value of amplification. To avoid that, each image or merged set of images has its own bounding box. If the bounding boxes overlap a new filling routine of a grid of $10^4 \times 10^4$ is called on area given by combination of the two bounding boxes.
9. The amplification of different image/merged set of images is summed up to give a total amplification of the source.

Pejcha & Heyrovský (57) avoided the need of image-plane subdivision by using a row flood-filling integration. In this approach the flood-fill starts from a trial point and continues firstly to the right then to the left until it gets outside of the image. Having found the strip of an image it continues, within the row, from another initial trial point on another row. In this way, the whole image can be filled. Main advantage of this method over 4- or 8-way approach to flood filling is that the positions visited can be represented by a list of integer pairs for each row corresponding to intersection of images' borders with the row. In this way, the code do not need to represent all coordinate positions on the image plane but only an array of lists suffices. This greatly reduce the memory requirements. The memory needed scale linearly with the grid size a row flood-filling with an efficient data representation. Although Pejcha & Heyrovský method satisfies precision requirements, i.e., precision of 10^{-3} for a source of $\rho = 10^{-3}$ Einstein radii, it does not bring a substantial improvement for the speed of algorithm. This is due to the fact that the most time-expensive part of the algorithm is IRS. A straightforward way of reducing the computational time would be reducing the number of rays shot for fixed accuracy. For that reason a subdivision of image plane is important step in evolution of IRS based approach since it affords an opportunity to use best suited coordinates on the finer grid.

5.3 Precision of the algorithm

For most of our calculation we used 2000×2000 grid for finer grid. Such a grid leads to lengthy calculations especially for sources of size bigger than 10^{-2} . Our goal is to keep errors around 0.1% of total amplification that is necessary to discuss extended source effect (57)

The most important source of errors in the area evaluation comes from the uncertainty in integrated area borders. It is an inherent property of the method that it can only determine whether a point is inside an image or not. It lacks a tool of localizing exact boundary position. Supposing an image border locally approximated by a straight line, the error is up to half of area of rectangle corresponding to pixels close to the image boundary. This leads us to worst-case scenario, when the image position and the grid are correlated that error equals half of area corresponding to image boundary pixels. In such a case the error to area ratio is proportional to $N^{-\frac{1}{2}}$ where N is number of pixels included in the image. To achieve 0.1% accuracy under such circumstances a 10^6 rays shot per image is required, i.e., tens of millions float operations per single source position.

If we are more interested in an ordinary rather than extremal case, we should consider that approximately half of points on the boundary of discretized image have positive deviation from correct value and another half have negative deviation. Thus expected error equals variation of statistical distribution of deviations of points on the border of discretized image. For binomial distribution this leads to $N^{-\frac{3}{4}}$. Hence $N \approx 10^4$ is the order of magnitude estimate of the number of rays required for the wanted accuracy.

This also answers the question when a finer grid method can be used and when much simpler single grid algorithm is sufficient. Having image plane of unit square covered by grid of $10^4 \times 10^4$ points we need a source of radius at least 10^{-2} . With increasing amplification also N increases but so does the total

perimeter of images that become extremely elongated. If the increment in area is proportional to the increment in perimeter, the lower boundary of the source size for the applicability of single $10^4 \times 10^4$ grid method is roughly $\rho = 10^{-2}$.

The aforementioned statistical discussion does not take into account a systematic error of flood-filling of thin images. While all boundary points can deviate by at most half of their area, pixels that become disconnected due to coarse grid are lost completely. This becomes extreme both for images of small source that are typically very thin for high amplifications and for image mergers. So, an error of caustic fold crossing on coarse grid is not well bounded.

In Figure 5.1 we plotted numerical noise, i.e. relative deviation from accurate amplification, of light curve resulting from a source crossing a caustic. Left column of panels is for source of radius 2×10^{-2} and the right column for source of radius 2×10^{-3} . Both sources have brightness profile given by equation ?? with parameter $v = 0.5$. At the top panel, there are light curves parametrized by x -coordinate of the source. Going in direction of increasing x -coordinate the source leaves the caustic. The amplification increases with decreasing distance from caustic. The light curve touches the caustic and the amplification increases further. Then the amplification reaches its peak and the amplification drops again as overlap between source and inner area of the caustic. The light curve has another jump in derivative when the source leaves the caustic completely.

Both light curves were obtained by 5000×5000 secondary grid, while the same grid was used as accurate value for the numerical noise evaluation. The second row from the top is for numerical noise of the corresponding light curve obtained from secondary grid of 2000×2000 points. For the both source sizes this resolution of the secondary grid yield deviation of less than 0.01% from accurate values. The relative deviation increases when the source and caustic overlap and decreases when the source leaves the caustic. The third row is for 500 points of secondary grid. For source radius of 2×10^{-2} is the deviation ratio well under 0.1% but for $\rho = 2 \times 10^{-3}$ the ratio increases up to 0.2% so it is advisable to use finer grid. The fourth row is for the light curve calculation on primary grid only. Both latter cases exhibit increase of the relative deviation for $\rho = 2 \times 10^{-3}$ when the source is outside the caustic and the amplification is small. While in the case of $\rho = 2 \times 10^{-2}$ the primary grid is sufficient to keep the errors under 0.1%, smaller source of $\rho = 2 \times 10^{-3}$ produces error of several percent of the amplification and thus secondary grid should be used.

The Figure 5.1 serves only as a generic case. One of class of microlens configuration that leads to significantly higher error are high amplification events of either single lens microlensing or planetary microlensing. In such scenarios the amplification is dominated by two thin images stretched along the Einstein ring of the single lens. Our approach to the problem of amplification computation is therefore limited by source sizes of several multiples of 10^{-4} in the high-amplification-event case.

Unfortunately, such a source sizes are not uncommon in planetary microlensing, e. g., OGLE-2006-BLG-109 with $\rho \approx 3 \times 10^{-4}$, OGLE-2008-BLG-310 with $\rho \approx 5 \times 10^{-4}$ and OGLE-2007-BLG-192 with $\rho \approx 9 \times 10^{-4}$. Version of image oriented IRS code dedicated to high-amplification events is discussed in (10). The difficulty of extremely thin images is overcome by use of polar grid centered in the star position.

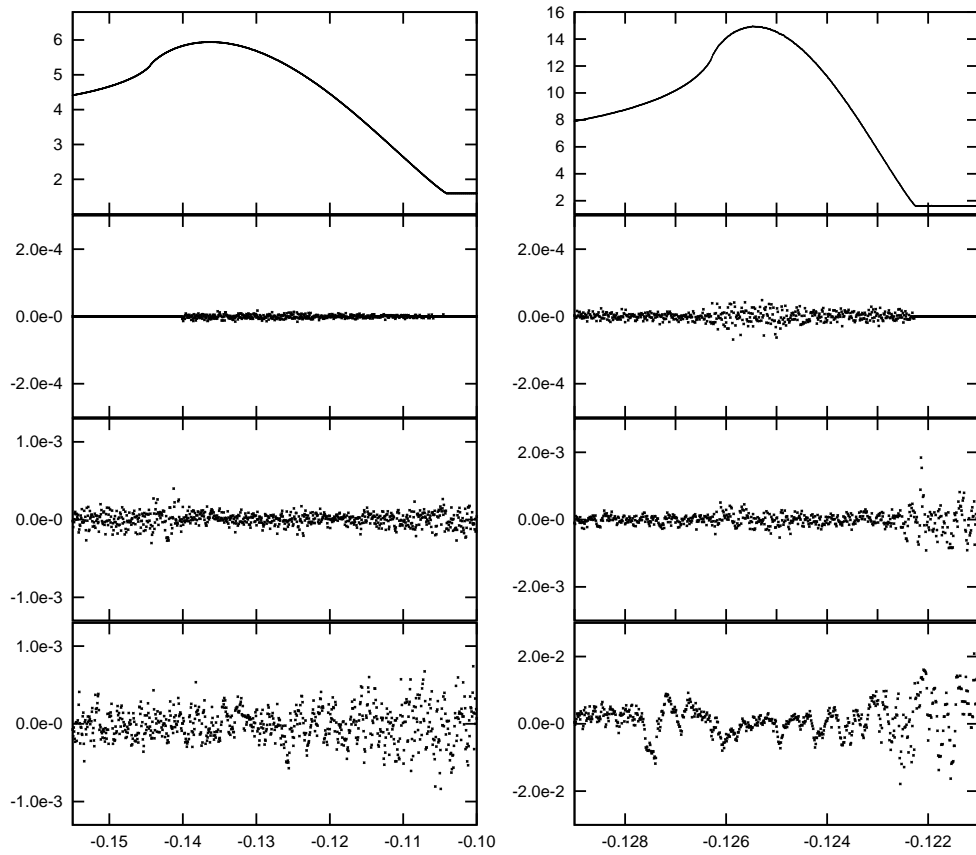


Figure 5.1 Numerical noise of the extended-source algorithm for caustic crossing. Top row for the light curve of secondary grid 5000×5000 , assumed accurate. Lower rows for relative deviation accurate amplification ratio: Second row for secondary grid 2000×2000 , third row for 500×500 , fourth row for primary grid only. Left column, source radius $\rho = 2 \times 10^{-2}$, the right column $\rho = 2 \times 10^{-3}$. x -axis ticks for x -component of source position.

5.4 Amplification maps

Although the observed microlensing events are recorded in form of light curves, we focus on amplification maps to give more complete account of the range of possible light curves for the given lens configuration.

Throughout the section radially symmetric source brightness profile $I(r)$ is used. For simplicity, we describe $I(r)$ by linear limb-darkening law described by equation 1.6.

An amplification map of a single lens is radially symmetric around the lens position given by equation (1.8), an extended source only smears the divergence at lens position. For multiple-point-mass lens the caustic appear, so that a amplification map of a point source diverges along the caustic. Again, the extended source smears out the divergences and blurs the caustic into band of width equal to source diameter.

In Figure 5.2 we present examples of amplification maps of an extended source lensed by a triple lens. For source radius of $\rho = 2 \times 10^{-3}$, the amplification map on larger scale is almost indistinguishable from point source amplification map, hence it is good for discussion of properties shared by both point-source and extended source maps. Such a map changes continuously outside the caustic with lobes of higher amplification around the cusps. Caustic folds present a discontinuity in amplification with much higher amplification inside the caustic loop. In inward direction of caustic the amplification decreases until it reaches plateau of slowly-changing values.

New features of the triple lens amplification maps in comparison to two-point-mass-lens ones are those that illustrate new caustic properties. Firstly, we have inward-pointing cusps. This type of cusps seem to develop lobes of higher amplification that distorts amplification of interior of the caustic. More importantly, the lobes reach out of caustic deforming the contour lines as seen in the detailed examples of Figure 5.2 for $\rho = 2 \times 10^{-3}$. Secondly, due to caustic self-intersection, multiply nested interior regions of caustic appear, e.g., the region in coordinates around coordinates (0.15, 0.05) in Figure 5.2. These regions have more images and tend to have higher amplifications in comparison to regions separated by single caustic crossing from exterior caustic regions.

Features of amplification extended-source maps are well demonstrated on case of $\rho = 2 \times 10^{-2}$ in Figure 5.2. At this source size the caustic pattern in the map becomes so blurred that the contour can pass through the caustic line freely. Small features on the caustic, like the post-swallow-tail pair of cusps in vicinity of caustic self-intersection of the right panel, are blurred beyond recognition, as shown in the detail of Figure 5.2.

For lens systems consisting of a star and multiple planet the amplification map is dominated by single-lens radially symmetric increase of amplification in direction of the star position. Of course, as for any n -point-mass lens system, the amplification map involves caustic divergences but with exception of small area around the star position the caustic tend to be “weak”, i.e., the caustic divergences are followed by steep downfall of amplification in interior of caustic for the point source. For extended source the “weak” caustic causes only a perturbation in amplification map of single lens in the star position.

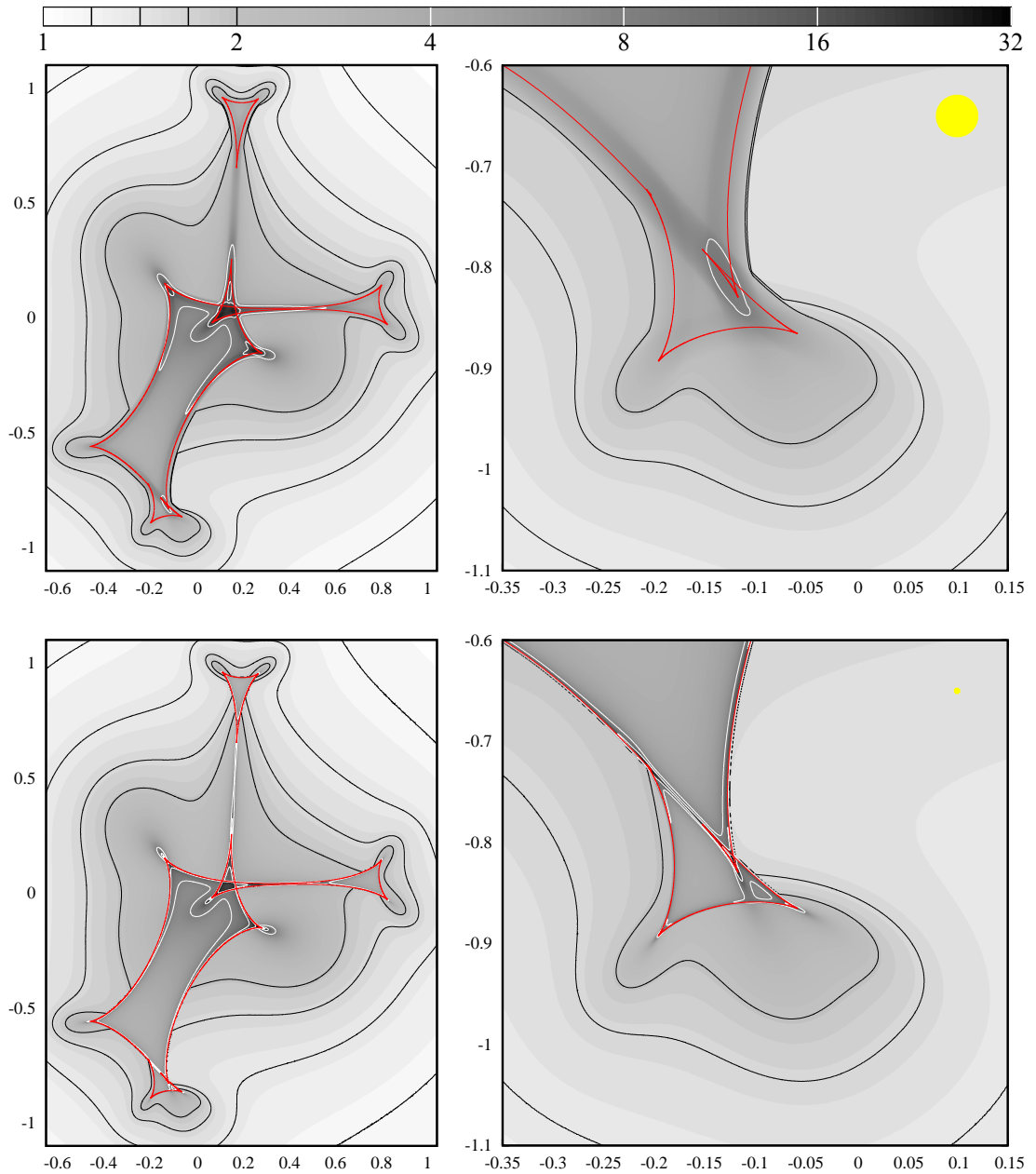


Figure 5.2 Extended source amplification maps with contours. The top row for source radius $\rho = 2 \times 10^{-2}$, the bottom row for $\rho = 2 \times 10^{-3}$; both with the same lens parameters and the linear limb darkening parameter $v = 0.5$. Lens component positions $z_1 = (-0.1578, -0.2034)$, $z_2 = (0.4722, -0.2034)$, $z_3 = (-0.31444975, 0.40680493)$, fractional masses $\mu_1 = 1/3$, $\mu_2 = 13/30$, $\mu_3 = 7/30$. Left column includes whole caustic, right column for detail of caustic self intersection. Yellow circle for source size. Red curve for caustic, black and white curves for amplification contour. Contours plotted for values of amplification $A = 2^k$: black contours $k = 0.25, 0.5, 0.75, 1$, white contours $k = 2, 3, 4, 5$ as shown in the color bar.

5.5 Sensitivity to an extended source

In this section we discuss the sensitivity of the microlensing amplification to the extended nature of the source. We follow the discussion of (57) and we expand it to case of triple lens. Our investigation uses only simple fixed brightness profile given by equation (1.6) so the dependence of amplification maps on limb-darkening profiles is not discussed.

We define the sensitivity to the extended nature of source δ_{ex} as the difference between point-source and extended source amplification over point source amplification

$$\delta_{ex}(\zeta_c) = \frac{A_*(\zeta_c) - A_0(\zeta_c)}{A_0(\zeta_c)}, \quad (5.1)$$

where ζ_c is position of the source center, A_* stands for extended-source amplification, A_0 stands for point-source amplification.

In Figure 5.3 sensitivity maps corresponding to the amplification maps of Figure 5.2 are shown. We omitted caustics since they stands out as boundary between areas of high positive deviation with deep red and high negative deviation in deep blue. This jump in sensitivity is due to the fact that an extended source whose center is outside a caustic while its limb stretches to caustic interior yields higher total amplification than a point source at its center, thanks to the additional images of the limb. On the other hand, extended source whose center is just inside the caustic lacks in amplification of limb area that is outside the caustic thus has negative δ_{ex} . The sensitivity rises again when the whole area of the source is inside the caustic.

More peculiar behavior of extended-source sensitivity maps can be observed around the cusps on the outer side of caustics. There is much steeper decrease of amplification in direction perpendicular to cusp axis than in direction parallel to the axis. For that reason there is negative δ_{ex} along a cusp axis because most of the source lies in areas of lower amplification than its center, similarly positive amplification excess is present off a cusp axis due to a limb being in area of higher amplification. In addition, opposite lobes of both negative and positive δ_{ex} along the cusp can connect while the caustic is in the state close to beak-to-beak metamorphosis, e. g., the uppermost triangular caustic loop disconnected from the main loop of caustics in Figure 5.2.

The generic behavior of sensitivity to extended nature of the source mentioned above was already discussed by Pejcha & Heyrovsky 2010 (57). New behavior of the triple-lens sensitivity is connected with the inward pointing cusps. In the details of $\rho = 0.002$ example, the inward pointing cusps has lobe of negative δ_{ex} along cusp axis with two lobes of positive δ_{ex} . The otherwise generic cusp pattern is interrupted by typical caustic fold pattern and then the two of three lobes continue outside the caustic while the right positive lobe is merged with a lobe of another cusp. The similar behavior is present for $\rho = 0.02$. Although various patterns are merged inside the caustic, the negative δ_{ex} lobe of inward pointing cusp is clearly visible outside of caustic while its the positive lobes are merged with positive lobes from other cusps.

Also caustic intersections can exhibit special pattern in extended-source-effect maps. In detailed plots of Figure 5.3, there is insufficient evidence of suppression

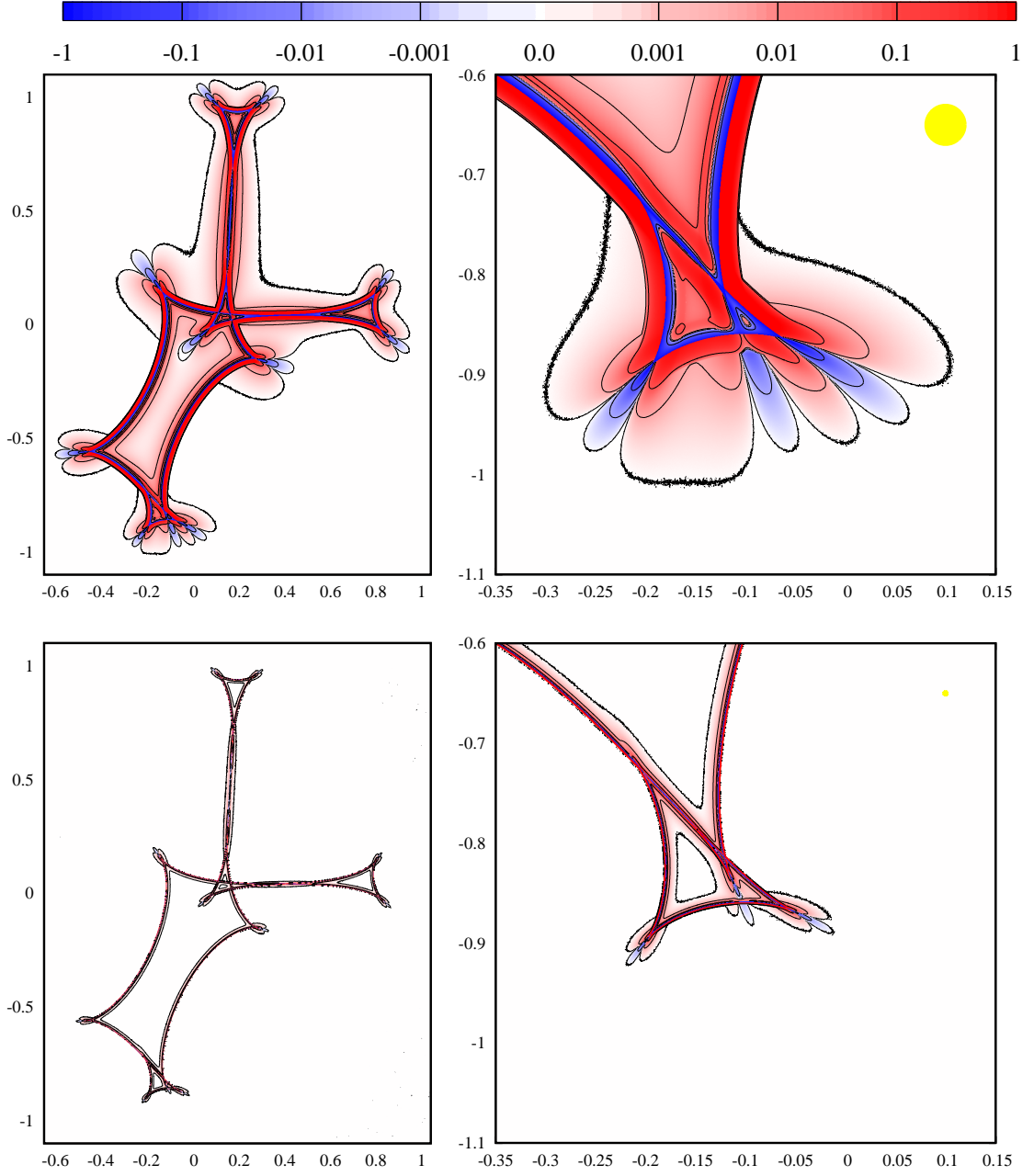


Figure 5.3 Extended-source sensitivity δ_{ex} maps corresponding to amplification maps in Figure 5.2. The top row for source radius $\rho = 2 \times 10^{-2}$, the bottom row for $\rho = 2 \times 10^{-3}$; both with the same lens parameters and linear limb-darkening parameter $v = 0.5$. Lens component positions $z_1 = (-0.1578, -0.2034)$, $z_2 = (0.4722, -0.2034)$, $z_3 = (-0.31444975, 0.40680493)$, fractional masses $\mu_1 = 1/3$, $\mu_2 = 13/30$, $\mu_3 = 7/30$. Left column includes whole caustic pattern, right column for detail of caustic self intersection. Yellow circle for source size. Plotted contours $\delta_{ex} = -0.1, -0.01, -0.001, 0.001, 0.01, 0.1$ as shown color bar.

of negative area along the fold just inside the caustic. However, for $\rho = 0.02$ detail panel shows thinning of negative δ_{ex} bands along the folds near the caustic intersection connected with two inward pointing cusps. The intersecting caustic is border between source plane domains with n , $n + 2$ and $n + 4$ images. If we place the source in such a position that its center lies in $n + 2$ domain but its limbs overlaps with both n and $n + 4$ regions the value of δ_{ex} can be either positive or negative depending on how balance between amplification with missing images of limb in n region and additional amplification due to the limb in region with $n + 4$ images.

Grainy ± 0.001 contours of $\rho = 0.02$ illustrate limits of numerical accuracy.

5.6 Amplification maps in vicinity of swallow-tail and butterfly metamorphoses

At this point we can combine the results from this chapter with theory developed in Chapter 2. In that way we benefit from the fact that we are able to localize swallow-tail and butterfly metamorphoses in parameter space of triple lens and to investigate the amplification maps in the vicinity of the metamorphosis points where the caustic metamorphoses occur. We are particularly interested in the way an amplification map change in order to accommodate extra cusps whose lobes can stretch far away from the metamorphosis itself.

For a caustic fold or caustic cusp the amplification maps have already been investigated in some detail in Section 5.4. The local approximation of the lens equation in the vicinity of caustic fold and cusp is summarized, e.g., in (70), while more recent and more comprehensive study for case for two-point mass lens can be found in Pejcha & Heyrovský (57). Up to this point, there is no study dedicated to the amplification maps due to caustic metamorphoses. However, our analysis of caustic-metamorphosis amplification maps is to be considered preliminary. We work only with some chosen examples of the metamorphoses without a general analytical model.

The caustic metamorphoses are explained in Chapter 2 with Figure 2.5 illustrating both swallow-tail and butterfly metamorphoses. In this Chapter we will add amplification maps do demonstrate the amplification behavior off the caustic. We skip discussion of beak-to-beak metamorphosis which is also common in triple lens. However, the beak-to-beak metamorphosis is already well known from the two-point-mass-lens model. Good example of amplification and extended-source sensitivity in vicinity of the metamorphosis can be found, e.g., in (57).

In Figure 5.4 we plotted sequence of point-source amplification maps for swallowtail metamorphosis. The metamorphosis starts with fold on the left then continues through the swallow-tail metamorphosis point in middle panel to pair of cusp and caustic self-intersection point in the right panel. In the first panel from the left we can see almost parallel amplification contours from the fold. The second panel shows almost no change in the caustics while the contours are distorted so that they do not follow the curvature of the fold but are rather linear in the region of interest. In vicinity of the metamorphosis point itself the caustic has discontinuity in the tangent vector. The contour have curvature opposite to the

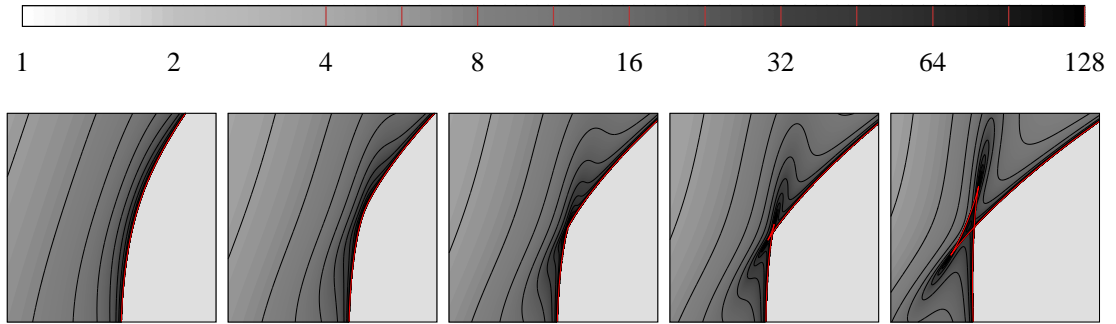


Figure 5.4 Sequence of point-source amplification maps undergoing swallowtail metamorphosis. Amplification in grayscale. Caustic in red. LA model of triple lens with equal masses discussed in section 3.5.3. Lens positions $z_1 = -29/60\alpha$, $z_2 = -1/30\alpha$, $z_3 = 31/60\alpha$ with $\alpha = \{2.0, 1.85, 1.79465, 1.74, 1.66\}$.

fold with very steep decrease of amplification in direction pointing inwards from the caustic perpendicular to the original fold. In direction tangent to the original fold, there are triangular areas of increased amplification after which the contours again lean back to the fold. In the fourth panel the caustic has two extra cusps and self-intersection. Caustic structure itself is not visible clearly but the triangular areas of higher amplification are transformed into characteristic cusp lobes with the contours on the side of the fold merging with the fold structures. In the last panel the caustic structure is more evident with clear cusp-lobe contours starting at the fold nearby the cusp ending on the other side of the cusp.

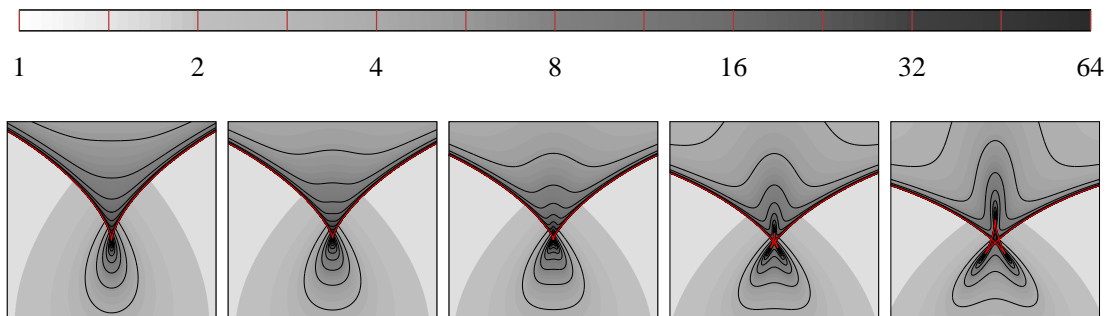


Figure 5.5 Sequence of point-source amplification maps undergoing butterfly metamorphosis. Amplification in greyscale. Caustic in red. LA model of triple lens with equal masses discussed in section 3.5.3. Lens positions $z_1 = -1/2\alpha$, $z_2 = 0$, $z_3 = 1/2\alpha$ with $\alpha = \{1.4, 1.19492, 1.1, 1.0, 0.92\}$.

The sequence of point-source amplification maps for butterfly metamorphosis is plotted in Figure 5.5. It starts from cusp and then transforms, via butterfly metamorphosis point, to three cusps with three caustic self-intersection. The left panel is for the cusp. Amplification contours inside the caustic follow the fold lines and they connect in the middle. There is a simple ditch along cusp axis with amplification increasing towards the cusp. Outside the caustics the contours shows behavior of simple cusp lobe. The second panel from the left is for butterfly metamorphosis point itself. The contours within the caustic are bent

in opposite direction along the cusp axis as the ditch bifurcates. The lobe outside the caustic becomes flattened along the cusp axis. There are three cusps in the third panel. The upward bend of the inside contours is more pronounced. The outside lobe bifurcates having two bumps at the bottom for contours of $A > 16$. In the fourth panel the three cusps are further away allowing us to see all three cusps. The three cusps have lobes of higher amplification. The bent contours within the caustic are clear extension of the inward-pointing cusp. In the last panel, the additional areas due to caustic intersection are visible.

The main observation about the amplification maps in vicinity of the caustic metamorphoses is that their effect is extended both in the source plane and in the parameter space. Typical pattern connected with those metamorphoses is obvious in amplification map long before the actual metamorphosis occur and the caustic changes number of its cusps. The swallowtail metamorphosis clearly disturbs fold amplification patten effectively changing shape of the light curve for both caustic crossing and caustic-grazing event. This can result in either steeper or flatter decrease of the amplification with distance from the fold within the caustic or completely new pattern for a source-trajectory going along the fold. The butterfly singularity shows flattening of cusp lobes and decrease of amplification of the cusp along its axis outside the caustic and increase of the amplification along the axis within the caustic.

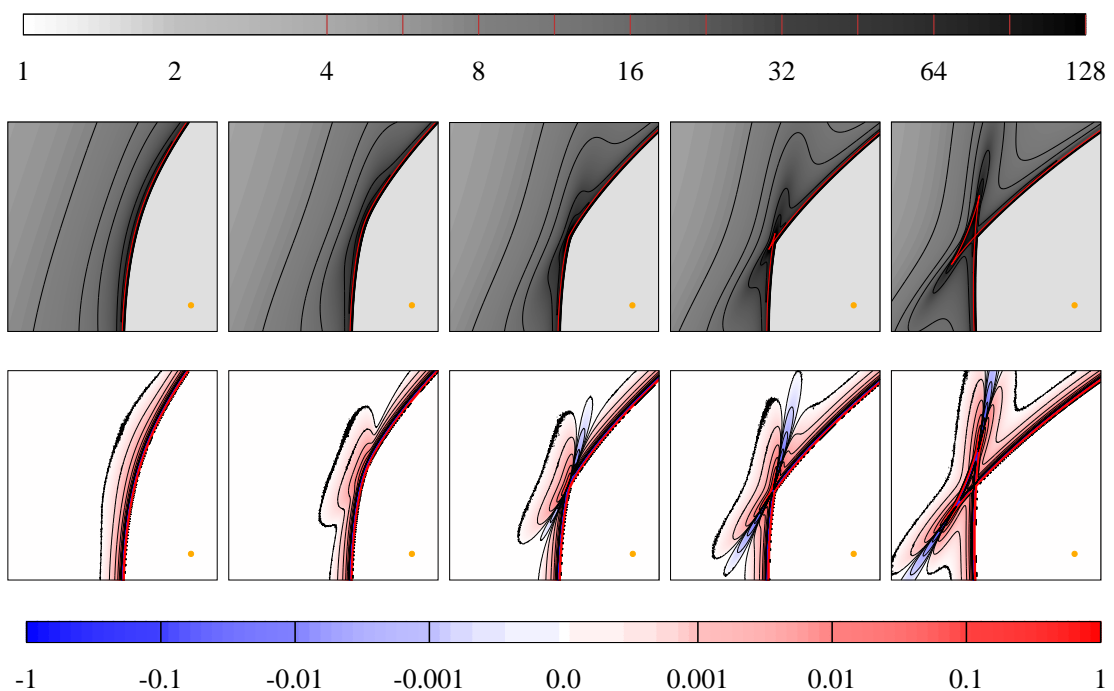


Figure 5.6 Effect of extended source for swallow tail metamorphosis. Top row: amplification-map sequence from Fig.5.4 for source size $\rho = 5 \times 10^{-4}$. Amplification in grayscale. Caustic in red. Contours in black. Source size indicated by orange circle. Bottom row: corresponding maps of extended-source effect. Blue for negative effect, red for positive effect.

To characterize the caustic metamorphoses further we discuss extended-source effect. Firstly we can show new types of shapes and regions that have higher

sensitivity to the extended nature of the source. Secondly, the expansion of extended-source effect in the small source limit is proportional to Laplacian of the amplification as derived by Pejcha & Heyrovský (57) so we can demonstrate properties of the amplification expansion.

Figure 5.6 illustrates the extended-source amplification and the extended-source effect maps for source size $\rho = 5 \times 10^{-4}$. In the amplification maps we can see the phenomenons we have already observed in the previous sections, e.g., blurring of the caustic. The blurring causes increased amplification both within and without the caustic. The extended-source effect maps have qualitatively new features emerging. Firstly, the fold in the second panel has a kidney-shaped blob of a increased positive effect around the point where the metamorphosis will occur. For the metamorphosis point itself lobes of negative effect appears separating the blob and the generic fold pattern, the contours of the blob become concave. In the fourth panel we can notice bent positive contours along the fold. In the last panel we can see all three lobes of sensitivity, two positive and one negative, for the two cusps. The contours of lobes adjacent to the folds are connected with the contours of the folds.

The extended-source amplification and the extended-source effect maps for the butterfly metamorphosis are shown in Figure 5.7. The extended-source effect maps offer a further insight into the butterfly metamorphosis. The most noteworthy is the step from the cusp to butterfly metamorphosis point, i.e., the leftmost two panels. Cusp phase itself shows no deviation from the map of ordinary cusp (one negative and two positive lobes). On the other hand, the butterfly-metamorphosis point has the negative-effect loop split in two which is quite distinctive feature not present in two-point-mass lens model. At the same time the amplification map shows little difference from the previous case. The fact that the negative lobe is split in this way also means that it has undergone a morphological change due to which it had become concave before it has reached the full split. At the first post-metamorphosis panel of Figure 5.7 two new lobes appear along the vertical axis, positive one outside and negative one inside the caustic. As the three cusps get more separated the positive lobe splits into two lobes one for each adjacent cusp and the negative lobe becomes lobe of inward pointing cusp that also grows two positive lobes on sides.

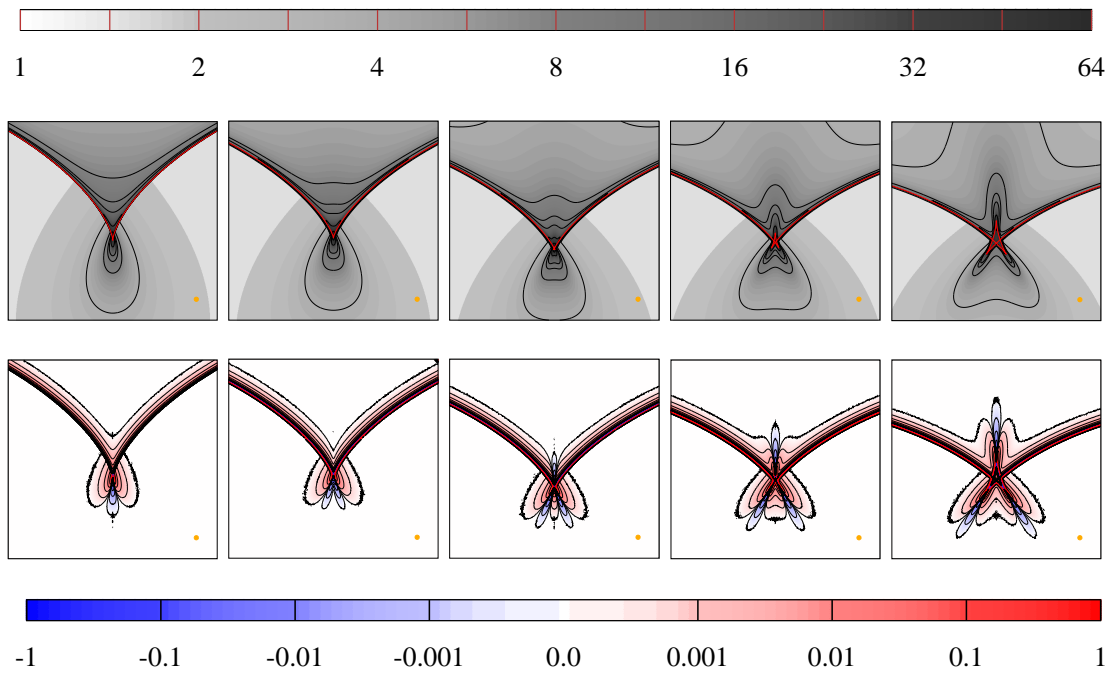


Figure 5.7 Effect of extended source for butterfly metamorphosis. Top row: amplification-map sequence from 5.5 for extended source of $\rho = 2 \times 10^{-3}$. Amplification in grayscale. Caustic in red. Contours in black. Source size indicated by orange circle. Bottom row: corresponding maps of extended-source effect. Blue for negative negative effect, red for positive effect.

6. Conclusions

In our investigation of the triple gravitational microlens we mainly focused on mapping of changes in topology of critical curves and caustic. We started with analysis of critical curves. We generalized approach of two-point-mass lens critical-curve analysis used by Erdl and Schneider (25) to a n -point mass lens. Firstly, we simplified the Sylvester matrix method by introduction of scale-less variables basically making the second resultant in the method redundant and thus both greatly reducing complexity of the calculation and avoiding spurious solutions to the problem. Secondly, we used Jacobian-contour correspondence, i.e., a correspondence between contours of a Jacobian determinant and critical curve of re-scaled lens configuration. Using the correspondence we reduced the problem of critical-curve topology changes to Jacobian saddle-point search.

Given critical curve topology, we know number of loops of the caustic. We were able to formulate conditions for catastrophes of higher order that do not lead to changes in critical-curve topology but can change number of caustic cusps. Firstly, we simplified the condition for a caustic cusp into form of one scale-invariant equation and equation of critical curve. Solving the equation for any scale we obtain cusp curves that under correct rescaling give main image of cusp position for whole family of caustics parametrized by the scale. Secondly, a condition for a swallow-tail metamorphosis was found as point where the cusp curve is tangent to a Jacobian contour. Using critical-curve equation and cusp-curve equation, the swallow-tail condition was transformed into scale-invariant form. The solutions of this equation has form of algebraic curve we call morph curve. A common solution of the equations of critical curve, cusp curve and morph curve can then give either beak-to-beak metamorphosis, swallowtail metamorphosis or butterfly metamorphosis. All of these catastrophes can change number of cusps, but only beak-to-beak changes also the number of caustic loops. Of course, it is unnecessary to solve full set of the equations to obtain parameters of a triple lens with a catastrophe mentioned above. Since any intersection of morph and cusp curve also lies on the same contour of the Jacobian, the corresponding scaled configuration involving the catastrophe can be obtained using the Jacobian-contour correspondence.

We demonstrated the methods of the critical curve and caustic analysis on case of several simple two- and three-parameter models. Firstly we investigated both critical curve topology and cusp number mapping for four two-parameter models. Those models are: Collinear symmetric model with variable central mass, collinear asymmetric model with equal masses, equilateral triangle with variable vertex mass and isosceles triangle with variable vertex angle. We have found nine different critical-curve topologies, as well as caustics with caustic number ranging from eight to twenty. For two-parameter models we supplied full galleries of critical curves and caustics and made note of every region separately and summarized their properties.

For the three-parameter models we have analyzed critical curves only. All three investigated models were triple lenses with the same set of free parameters, i.e. shape and scale parameters. Each model has fixed masses corresponding to different physical models. First model has equal masses and is used mainly

to illustrate the method. The second model has two equal masses and third body of one thousandth of total mass. It can be interpreted as planet in binary lens system. The third model include one massive lens and two lens points with masses 10^{-2} and 10^{-4} of the first lens point respectively and can be interpreted as star with two planets or star with planet and moon. In each case of three-parameter models we used sequences of ternary plots to depict the parameter space. Especially the latter two models include regions of parameter space that are too small or too narrow to be analyzed in full detail. We also computed weighted volumes of the regions and thus obtained occurrence probabilities.

We have analyzed amplification maps of triple lens. We developed a code for computing the amplification of an extended source with a general brightness profile. The code integrates images of the source using a flood-fill algorithm with inverse ray-shooting, and permits refinement of the image-plane grid when necessary. We investigated amplification maps of triple lenses. Discussed new triple-lens amplification-map features including caustic self-intersection, inward pointing cusps and cusp lobes of higher amplification stretching from within the caustic through a fold. We evaluated sensitivity to extended nature of the source. Finally, we investigated amplification and extended-source effect maps for swallow-tail and butterfly caustic metamorphoses. We demonstrated that the patterns specific to the caustic metamorphoses are extended and they occur long before actual metamorphosis takes place.

We have discovered eleven critical-curve topologies. The question whether this set of topologies of triple lens is complete remains unanswered. However, extent of our study leaves us with confidence that there are not many other topologies left and that the topologies that were not found have low probability of occurrence.

The tools introduced in this work can be a base for further studies of n -point-mass lenses. The method of evaluation of the extended-source amplification can be used in analysis of the observed data and, in combination with the our theoretical methods used in deeper study of the amplification-map features characteristic of triple and general n -point-mass lens.

Bibliography

- [1] Alcock, C., Allsman, R. A., Alves, D., et al., *Binary Microlensing Events from the MACHO Project*, The Astrophysical Journal **541** (2000), 270-297.
- [2] Alcock, C., et al., *The MACHO Project: Microlensing Results from 5.7 Years of Large Magellanic Cloud Observations*, The Astrophysical Journal **502** (2000), 281-307.
- [3] Alard, C., Mao, S., & Guibert, J., *Object DUO 2: a new binary lens candidates?*, Astronomy & Astrophysics **300** (1995), L17-L20.
- [4] Asada, H., *Perturbation theory of N point-mass gravitational lens systems without symmetry: small mass-ratio approximation*, Monthly Notices of Royal Astronomical Society **394** (2009), 818-830.
- [5] Asada, H., *Five Point Mass Gravitational Lenses in a Rhombus as a Soluble Model Giving the Maximum Number of Images*, Progress of Theoretical Physics **121** (2009), 121, 1381-1387.
- [6] Bennett, D. P., Rhie, S. H., Becker, A. C., et al., *Discovery of a planet orbiting a binary star system from gravitational microlensing*, Nature **402** (1999), 57-59.
- [7] Bennett, D. P., *Masses and Orbital Constraints for the OGLE-2006-BLG-109Lb,c Jupiter/Saturn Analog Planetary System*, The Astrophysical Journal **713** (2010), 837-855.
- [8] Bennett, D. P., Rhie, S. H., *Detecting Earth-Mass Planets With Gravitational Microlensing*, The Astrophysical Journal **472** (1996), 660-664.
- [9] Beaulieu, J.-P., Bennett, D. P., Fouqué, P., et al., *Discovery of a cool planet of 5.5 Earth masses through gravitational microlensing*, Nature **439** (2006), 437-440.
- [10] Bennett, D. P., *An Efficient Method for Modeling High-Magnification Planetary Microlensing Events*, The Astrophysical Journal **716** (2010), 1408-1422.
- [11] Bond, I. A., Udalski, A., Jaroszyński, M., et al., *OGLE 2003-BLG-235/MOA 2003-BLG-53: A Planetary Microlensing Event*, The Astrophysical Journal **606** (2004), L155-L158.
- [12] Bozza, V., *Perturbative analysis in planetary gravitational lensing*, Astronomy & Astrophysics **348** (1999), 311-326.
- [13] Bozza, V., *Caustics in special multiple lenses*, Astronomy & Astrophysics **355** (2000), 423-432.
- [14] Bozza, V., *Secondary caustics in close multiple lenses*, Astronomy & Astrophysics **359** (2000), 1-8.

- [15] Bozza, V., *Microlensing with an advanced contour integration algorithm: Green's theorem to third order, error control, optimal sampling and limb darkening*, Monthly Notices of Royal Astronomical Society **408** (2010), 2188–2200.
- [16] Chang, K., & Refsdal, S., *Star disturbances in gravitational lens galaxies*, Astronomy & Astrophysics **132** (1984), 168-178.
- [17] Chung, S.-J., Park, B.-G., *Properties of the Central Perturbations by Planets in Binary Stellar Systems under the Strong Finite-Source Effect*, The Astrophysical Journal **713** (2010), 865-870.
- [18] Daněk, K., 2010, Master's thesis, Charles University in Prague.
- [19] Daněk, K., Heyrovský, D., 2011, in WDS'11 Proceedings of Contributed Papers: Part III – Physics, ed. J. Šafránková & J. Pavlů (Prague: Matfyzpress), 37-42.
- [20] Daněk, K., Heyrovský, D., 2014, in Springer Proceedings in Physics 157, Relativity and Gravitation, ed. J. Bičák & T. Ledvinka (Cham: Springer International), 423-426.
- [21] Daněk, K., Heyrovský, D., 2015, *Image-plane Analysis of n -point-mass Lens Critical Curves and Caustics*, The Astrophysical Journal , in press (arXiv:1501.02722)
- [22] Daněk, K., Heyrovský, D., *Critical Curves and Caustics of Triple-lens Models*, The Astrophysical Journal , in press (arXiv:1501.06519)
- [23] Dominik, M., *The binary gravitational lens and its extreme cases*, Astronomy & Astrophysics **349** (1999), 108-125.
- [24] Einstein, A., *Lens-Like Action of a Star by the Deviation of Light in the Gravitational Field*, Science **84** (1936), 506-507.
- [25] Erdl, H., Schneider, P., *Classification of the multiple deflection two point-mass gravitational lens models and application of catastrophe theory in lensing*, Astronomy & Astrophysics **268** (1993), 453-471.
- [26] Escofier, J.-P., *Galois Theory*, NY: Springer, New York 2001.
- [27] Gaudi, B. S., Nabel, R. M., Sacket, P. D., *Microlensing by multiple planets in high-magnification events*, The Astrophysical Journal Letters **502** (1998), 33-37.
- [28] Gaudi, B. S., *Discovery of a Jupiter/Saturn Analog with Gravitational Microlensing*, Science **319** (2008), 927-930.
- [29] Gaudi, B. S., Chang, H.-Y., & Han, C., *Probing Structures of Distant Extrasolar Planets with Microlensing*, The Astrophysical Journal **586** (2003), 527-539.
- [30] Gould, A., *Hexadecapole Approximation in Planetary Microlensing*, The Astrophysical Journal **681** (2008), 1593–1598.

- [31] Gould, A., Udalski, A., Shin, I.-G., et al., *Hexadecapole Approximation in Planetary Microlensing*, *Science* **345** (2014), 46-49.
- [32] Grieger, B., Kayser R., Refsdal, S., & Stabell, *The Two Point Mass Gravitational Lens*, R. 1989, *Abhandlungen aus der Hamburger Sternwarte* **10** (1989), 177-223.
- [33] Han, C., Chang, H.-Y., An, J. H., & Chang, K., *Properties of Microlensing Light Curve Anomalies Induced by Multiple Planets*, *Monthly Notices of Royal Astronomical Society* **328** (2001), 986–992.
- [34] Han, C., & Han, W., *On the Feasibility of Detecting Satellites of Extrasolar Planets via Microlensing*, *The Astrophysical Journal* **580** (2002), 490-493.
- [35] Han, C., & Park, M.-G., *A New Channel to Search for Extra-Solar Systems with Multiple Planets via Gravitational Microlensing*, *Journal of Korean Astronomical Society* **35** (2002), 35-40.
- [36] Han, C., *Analysis of Microlensing Light Curves Induced by Multiple-Planet Systems*, *The Astrophysical Journal* **629** (2005), 1102-1109.
- [37] Han, C., *Microlensing Search for Planets with Two Simultaneously Rising Suns*, *The Astrophysical Journal Letters* **676** (2008), L53-L56.
- [38] Han, C., *Microlensing Detections of Moons of Exoplanets*, *The Astrophysical Journal* **684** (2008), 684-690.
- [39] Han, C., Udalski, A., Choi, J.-Y., et al., *The Second Multiple-Planet System Discovered By Microlensing: OGLE-2012-BLG-0026Lb, c—A Pair of Jovian Planets Beyond The Snow Line*, *The Astrophysical Journal Letters* **762** (2013), L28-L33.
- [40] Jaroszyński, M. *Binary Lenses in OGLE-II 1997–1999 Database. A Preliminary Study*, *Acta Astronomica* **52** (2002), 39-60.
- [41] Jaroszyński, M., Udalski, A., Kubiak, M., et al., *Binary Lenses in OGLE-III EWS Database. Seasons 2002-2003*, *Acta Astronomica* **54** (2004), 103-128.
- [42] Jaroszyński, M., Skowron, J., Udalski, A., et al., *Binary Lenses in OGLE-III EWS Database. Season 2004*, *Acta Astronomica* **56** (2006), 307-332.
- [43] Jaroszyński, M., Skowron, J., Udalski, A., et al., *Binary Lenses in OGLE-III EWS Database. Seasons 2006-2008*, *Acta Astronomica* **60** (2010), 197-231.
- [44] Kayser, R., Refsdal, S., Stabell, R., *Astrophysical applications of gravitational micro-lensing*, *The Astrophysical Journal* **166** (1986), 36-52.
- [45] Khavinson, D., & Neumann, G., *On the number of zeros of certain rational harmonic functions*, *Proceedings of the American Mathematical Society* **134** (2006), 1077-1085.
- [46] Kubas, D., Cassan, A., Dominik, M., et al., *Limits on additional planetary companions to OGLE 2005-BLG-390L*, *Astronomy & Astrophysics* **483** (2008), 317-324.

- [47] Lee, D.-W., Lee, Ch.-U., Park, B.-G., et al., *Microlensing Detections of Planets in Binary Stellar Systems*, The Astrophysical Journal **672** (2008), 623-628.
- [48] Liebig, Ch., Wambsganss, J., *Detectability of extrasolar moons as gravitational microlenses*, Astronomy & Astrophysics **520** (2010), 68-80.
- [49] Link, F., *Sur les Conséquences Photométriques de la Deviation d'Einstein*, Comptes Rendus de l'Académie des Sciences **52** (1936), 917-919.
- [50] Link, F., *Sur les Conséquences Photométriques de la Deviation d'Einstein*, Bulletin Astronomique **10** (1937), 73-90.
- [51] Luce, R., Sète, O., & Liesen, J., *Sharp parameter bounds for certain maximal point lenses*, General Relativity and Gravitation **46** (2014), 1736-1751.
- [54] Mao, S., Petters, A. O., & Witt, H. J. 1997, arXiv:astro-ph/9708111
- [53] Mao, S., Paczyński, B., *Gravitational microlensing by double stars and planetary systems*, The Astrophysical Journal **374** (1991), L37-L40.
- [54] Mao, S., Petters, A. O., & Witt, H. J., *Properties of Point Mass Lenses On A Regular Polygon and The Problem of Maximum Number of Images*, 1997 , arXiv:astro-ph/9708111
- [55] Paczyński, B., *Gravitational microlensing by the galactic halo*, The Astrophysical Journal **304** (1986), 1-5.
- [56] Paczyński, B., *Gravitational Microlensing in the Local Group*, Annual Review of Astronomy and Astrophysics **34** (1996), 419-460.
- [57] Pejcha, O., Heyrovský, D., *Extended-source effect and chromacity in two-point-mass microlensing*, The Astrophysical Journal **690** (2009), 1772-1796.
- [59] Petters, A. O., Levine, H., Wambsganss, J., *Singularity Theory and Gravitational Lensing*, Birkhäuser, Boston 2001.
- [59] Petters, A. O., Levine, H., & Wambsganss, J. 2001, *Singularity Theory and Gravitational Lensing* (Boston, MA: Birkhäuser)
- [60] Poleski, R., et al., *Triple Microlens OGLE-2008-BLG-092L: Binary Stellar System with a Circumprimary Uranus-type Planet*, The Astrophysical Journal **795** (2014), 42-50.
- [61] Poston, T. , Stewart, I., *Catastrophe theory and its applications*. Dover, Mineola 1996.
- [62] Rattenbury, N. J., Bond, I. A., Skuljan, J., & Yock, P. C. M., *Planetary Microlensing at High Magnification*, Monthly Notices of Royal Astronomical Society **335** (2002), 159-169.
- [63] Rhie, S. H., *Infimum Microlensing Amplification of the Maximum Number of Images of n -Point Lens Systems*, The Astrophysical Journal **484** (1997), 63-69.

- [64] Rhie, S. H., *Can A Gravitational Quadruple Lens Produce 17 images?*, 2001, arXiv:astro-ph/0103463
- [65] Rhie, S. H., *How Cumbersome is a Tenth Order Polynomial?: The Case of Gravitational Triple Lens Equation*, 2002, arXiv:astro-ph/0202294
- [66] Rhie, S. H., *n-point Gravitational Lenses with $5(n-1)$ Images*, 2003, arXiv:astro-ph/0305166.
- [67] Rhie, S. H., & Bennett, D. P., *Line Caustic Microlensing and Limb Darkening*, 1999, arXiv:astro-ph/9912050.
- [68] Refsdal, S., *Gravitational Lens Effect*, Monthly Notices of Royal Astronomical Society **128** (1964), 295-306.
- [69] Ryu, Y.-H., Chang, H.-Y., Park, M.-G., *Detection probability of a low-mass planet for triple lens events: implication of properties of binary-lens superposition*, Monthly Notices of Royal Astronomical Society **412** (2011), 503-510.
- [70] Schneider, P., Ehlers, J., Falco, E. E., *Gravitational lenses*, Springer, Berlin 1999.
- [71] Schneider, P., Weiss, A., *The two-point-mass lens: detailed investigation of special asymmetric gravitational lens*, Astronomy & Astrophysics **164** (1986), 237-259.
- [72] Sète, O., Luce, R., & Liesen, J., *Creating images by adding masses to gravitational point lenses*, General Relativity and Gravitation **47** (2015), 42-49
- [73] Skowron, J., Jaroszyński, M., Udalski, A., et al., *Binary Lenses in OGLE III EWS Database. Season 2005*, Acta Astronomica **57** (2007), 281-299.
- [74] Song, Y.-Y., Mao, S., & An, J. H., *Degeneracies in Triple Gravitational Microlensing*, Monthly Notices of Royal Astronomical Society **437** (2014), 4006-4018.
- [75] Sturmfels, B. *Solving Systems of Polynomial Equations*, American Mathematical Society, Providence, RI 2002
- [76] Udalski, A., Szymanski, M., Kaluzny, J., et al., *The Optical Gravitational Lensing Experiment*, Acta Astronomica **42** (1992), 253-284.
- [77] Udalski, A., Szymanski, M., Mao, S., et al., *The optical gravitational lensing experiment: OGLE no. 7: Binary microlens or a new unusual variable?*, The Astrophysical Journal Letters **436** (1994), 436, L103-L106.
- [78] Witt, H. J., *Investigation of high amplification events in light curves of gravitationally lensed quasars*, Astronomy & Astrophysics , **236** (1990), 311-322
- [79] Witt, H. J., Petters, A. O., *Singularities of the one- and two-point mass gravitational lens*, Journal of Mathematical Physics **34** (1993), 4093-4110.

- [80] Vermaak, P., *The effects of resolved sources and blending on the detection of planets via gravitational microlensing*, Monthly Notices of Royal Astronomical Society **319** (2000), 1011-1019.
- [81] Zhu, W., Gould, A., Penny, M., Mao, S., & Gendron, R., *Empirical Study of Simulated Two-planet Microlensing Events*, The Astrophysical Journal **794** (2014), 794, 53-62.

A. Computing the resultant of two polynomials

A polynomial $f(x)$ of degree $d \geq 1$ with roots ξ_1, \dots, ξ_d can be written as

$$f(x) = \sum_{j=0}^d a_j x^j = a_d \prod_{j=1}^d (x - \xi_j), \quad (\text{A.1})$$

where $a_d \neq 0$. Similarly, for another polynomial $g(x)$ of degree $e \geq 1$ with roots η_1, \dots, η_e we have

$$g(x) = \sum_{j=0}^e b_j x^j = b_e \prod_{j=1}^e (x - \eta_j) \quad (\text{A.2})$$

with $b_e \neq 0$. The resultant of the two polynomials is a function of their coefficients that is proportional to the product of the differences of all combinations of individual roots, specifically (e.g., 26),

$$\text{Res}_x(f, g) = a_d^e b_e^d \prod_{j=1}^d \prod_{k=1}^e (\xi_j - \eta_k). \quad (\text{A.3})$$

Using equations (A.1) and (A.2), we can write the resultant also in the form (e.g., 75)

$$\text{Res}_x(f, g) = a_d^e \prod_{j=1}^d g(\xi_j) = (-1)^{de} b_e^d \prod_{k=1}^e f(\eta_k). \quad (\text{A.4})$$

It follows from equation (A.3) that the condition for the two polynomials to have at least one common root is equivalent to the condition

$$\text{Res}_x(f, g) = 0, \quad (\text{A.5})$$

an equation in terms of the coefficients of the polynomials.

A common way to compute the resultant is based on the Sylvester matrix $S(f, g)$. This $(d + e) \times (d + e)$ matrix is formed by arranging the coefficients of $f(x)$ from highest to lowest order, filling the sequence repeatedly in the first e rows gradually staggered to the right, followed by d rows of coefficients of $g(x)$ staggered in a similar manner, filling the rest with zeros (e.g., 59). Explicitly,

$$S(f, g) = \begin{pmatrix} a_d & a_{d-1} & \cdots & a_0 & 0 & \cdots & 0 \\ 0 & a_d & \cdots & a_1 & a_0 & \cdots & 0 \\ \vdots & \vdots & & & & & \vdots \\ 0 & 0 & \cdots & \cdots & \cdots & & a_0 \\ b_e & b_{e-1} & \cdots & b_0 & 0 & \cdots & 0 \\ 0 & b_e & \cdots & b_1 & b_0 & \cdots & 0 \\ \vdots & \vdots & & & & & \vdots \\ 0 & 0 & \cdots & \cdots & \cdots & & b_0 \end{pmatrix}. \quad (\text{A.6})$$

The resultant is then obtained simply by computing the determinant of the Sylvester matrix,

$$\text{Res}_x(f, g) = \det S(f, g). \quad (\text{A.7})$$

In some texts (e.g., 26) the Sylvester matrix is defined as the transpose of the matrix in equation (A.6), i.e., with coefficients in staggered columns rather than rows. However, this doesn't change the determinant, so that equation (A.7) remains valid. In other texts the form of the matrix in equation (A.6) remains the same, but the coefficients are filled in reverse, from lowest to highest order (e.g., 25; 75). The determinant of such a matrix is not always equal to the resultant defined by equation (A.3), it differs by a factor $(-1)^{de}$. However, this difference plays no role when seeking the null-resultant condition given by equation (A.5), which is equivalent to $\det S(f, g) = 0$.

An alternative way to compute the resultant utilizes the smaller $n \times n$ Bézout matrix $B(f, g)$, where $n = \text{Max}(d, e)$. The matrix is obtained by anti-symmetrizing the direct product of the polynomials, dividing the result by the difference of their variables, and ordering the terms according to the powers of the variables. The elements of the matrix are thus defined by (e.g., 75)

$$\sum_{j,k=0}^{n-1} B_{jk}(f, g) x^j y^k = \frac{f(x)g(y) - f(y)g(x)}{x - y}. \quad (\text{A.8})$$

If we assume that the degree of the first polynomial $d \geq e$, substituting the expressions from equations (A.1) and (A.2) in equation (A.8) then yields $B_{jk}(f, g)$ in terms of the coefficients:

$$\sum_{j,k=0}^{d-1} B_{jk}(f, g) x^j y^k = \sum_{j,k=0}^{d-1} x^j y^k \sum_{l=\text{Max}(j+1,k+1)}^{\text{Min}(d,j+k+1)} a_l b_{j+k-l+1} - \sum_{j,k=0}^{e-1} x^j y^k \sum_{l=\text{Max}(j+1,k+1)}^{\text{Min}(e,j+k+1)} a_{j+k-l+1} b_l. \quad (\text{A.9})$$

For polynomials of the same degree ($d = e$) the result simplifies to directly yield

$$B_{jk}(f, g) = \sum_{l=\text{Max}(j+1,k+1)}^{\text{Min}(d,j+k+1)} (a_l b_{j+k-l+1} - a_{j+k-l+1} b_l). \quad (\text{A.10})$$

Assuming the more general $d \geq e$ case, the resultant is computed as the determinant of the Bézout matrix multiplied by a non-zero factor:

$$\text{Res}_x(f, g) = (-1)^{d(d-1)/2} a_d^{e-d} \det B(f, g). \quad (\text{A.11})$$

Hence, the condition for a common root from equation (A.5) is equivalent to setting $\det B(f, g) = 0$.

The Bézout matrix has the advantage of being smaller, while the Sylvester matrix is usually sparser. If any particular symbolic-manipulation software package fails to compute the determinant of one of them, one can try using the other, before resorting to numerical computations.

B. Spurious results of the resultant method

The polynomial $p_{res}(w)$ defined by equation (3.11) has a set of roots w_1, \dots, w_m . The polynomial $p_{conj}(w)$ defined by equation (3.12) then has roots $\bar{w}_1^{-1}, \dots, \bar{w}_m^{-1}$. The search for a common unit root using equation (3.13) assumes that for at least one of the roots $w_j = \bar{w}_j^{-1}$, and hence it lies on the unit circle. However, equation (3.13) is satisfied even by a non-unit root w_j if it is equal to the inverse conjugate of a different root, i.e., $w_j = \bar{w}_k^{-1}$ for some other $w_k \neq w_j$. This implies that w_k is another non-unit root satisfying equation (3.13). In case p_{res} has only real coefficients (e.g., in the case of the two-point-mass lens or the triple-lens models from § 3.5.2 – § 3.5.5) and w_j lies off the real axis, \bar{w}_j and \bar{w}_k are two more non-unit roots of p_{res} . The total number of such spurious solutions depends on the degree of the polynomial p_{res} , which is $\leq 3n - 3$, as discussed in § 3.3.2.

In the case of the two-point-mass lens, the polynomial given by equation (3.17) is of third degree and has real coefficients. Spurious solutions off the real axis would require p_{res} to have at least four different roots $\{w_1, w_2 = \bar{w}_1^{-1}, \bar{w}_1, \bar{w}_2 = w_1^{-1}\}$, hence they do not occur. A spurious solution w_1 along the real axis would require p_{res} to have a set of real roots $\{w_1, w_2 = w_1^{-1}, w_3\}$ and p_{conj} a corresponding set of roots $\{w_1^{-1}, w_1, w_3^{-1}\}$. We could then write

$$p_{res}(w) = (w - w_1)(w - w_1^{-1})(w - w_3). \quad (\text{B.1})$$

Expanding this expression and comparing it term-by-term with equation (3.17), we find that the only possible real solution is $w_1 = w_2 = 1$, which lies on the unit circle and thus is not spurious. Moreover, this double-root solution requires either $\mu = 0$ or $\mu = 1$, thus it corresponds to the single-lens limit rather than a genuine binary. The nonexistence of real spurious solutions can also be seen from the discriminant of p_{res} computed from equation (3.17). The result is always negative for $\mu \neq 0, 0.5, 1$. Therefore, except for these values p_{res} has one root on and two roots off the real axis. For the only other non-degenerate case, $\mu = 0.5$, the roots are $\{-2s^2, -2s^2, s^2/4\}$. We see that even in this case there is no reciprocal pair of roots and hence no spurious solution. For the two-point-mass lens all solutions of equation (3.13) thus correspond to topology changes of the critical curve.

In all the triple-lens cases analyzed in § 3.5.2 – § 3.5.5, spurious solutions do occur. In the LS model the 6th-degree saddle-point and critical-curve polynomials in fact can be studied as 3rd-degree polynomials in z^2 . The first resultant then leads to a 3rd-degree $p_{res}(w)$, which can be shown to have a pair of real spurious roots $w_1 = w_2^{-1}$ when the central mass $\mu < 0.2$. In the three other models $p_{res}(w)$ is of 6th degree. Regions in parameter space with spurious solutions can be found for each of them.

C. Cusp and morph curve polynomials of the LS model

We present here the explicit form of the cusp and morph curve polynomials for the simplest triple-lens model studied in this work, the linear symmetric model from § 3.5.2.

The cusp curve is generally defined by equation (3.27), with $n = 3$ for the triple lens. We first multiply the equation by $(z - z_1)^6(z - z_2)^6(z - z_3)^6$. Next we substitute the positions and masses of the LS-model components, $\{z_1, z_2, z_3\} = \{-s, 0, s\}$ and $\{\mu_1, \mu_2, \mu_3\} = \{(1 - \mu)/2, \mu, (1 - \mu)/2\}$. We obtain the parametric polynomial form of the cusp curve,

$$\begin{aligned}
 p_{cusp}(z) = & \\
 & (1 - \Lambda) z^{12} + 3[2 - 4\mu + \Lambda(3\mu - 1)] s^2 z^{10} + 3[3 - 10\mu + 12\mu^2 - \Lambda(1 - 5\mu + 9\mu^2)] s^4 z^8 \\
 & + [4\mu(4 - 9\mu) - \Lambda(1 - 3\mu + 9\mu^2 - 27\mu^3)] s^6 z^6 - 3[2 - 7\mu + \Lambda(1 - 5\mu + 9\mu^2)] \mu s^8 z^4 \\
 & - 3[2 + \Lambda(1 - 3\mu)] \mu^2 s^{10} z^2 + (1 - \Lambda\mu) \mu^2 s^{12} = 0, \tag{C.1}
 \end{aligned}$$

where $\Lambda > 0$ is a real non-negative parameter.

In a similar manner we convert the morph-curve equation (3.28) for $n = 3$, using exactly the same steps. After multiplication by $(z - z_1)^6(z - z_2)^6(z - z_3)^6$ and substitution of the LS model positions and masses, we obtain the parametric polynomial form of the morph curve,

$$\begin{aligned}
 p_{morph}(z) = & \\
 & -i\Gamma z^{12} + [1 - \mu - 6i\Gamma(1 - 2\mu)] s^2 z^{10} - [2 - 8\mu + 6\mu^2 + 3i\Gamma(3 - 10\mu + 12\mu^2)] s^4 z^8 \\
 & + [1 - 12\mu + 11\mu^2 - 4i\Gamma\mu(4 - 9\mu)] s^6 z^6 + [4 - 4\mu + 3i\Gamma(2 - 7\mu)] \mu s^8 z^4 \\
 & + [1 - \mu + 6i\Gamma\mu] \mu s^{10} z^2 - i\Gamma\mu^2 s^{12} = 0, \tag{C.2}
 \end{aligned}$$

where Γ is a real parameter.

We see that in the LS model both polynomials are of sixth degree in z^2 . Intersections of the cusp curve given by equation (C.1) and the critical curve given by equation (3.33) identify cusp images along the critical curve. Intersections of the morph curve given by equation (C.2) and the cusp curve identify the images of caustic-metamorphosis points in the image plane, as discussed in § 3.4.